Positron Annihilation Studies on Thin Film Solar Cells: CdSe and PbSe Quantum Dot Thin Films and Cu(In1-xGax)Se2 Layered Systems

Shi, Wenqin

DOI
10.4233/uuid:e90ee9dc-0b00-4908-be32-c6a3efb425e2

Publication date
2019

Document Version
Final published version

Citation (APA)
Shi, W. (2019). *Positron Annihilation Studies on Thin Film Solar Cells: CdSe and PbSe Quantum Dot Thin Films and Cu(In1-xGax)Se2 Layered Systems*. [Dissertation (TU Delft), Delft University of Technology]. https://doi.org/10.4233/uuid:e90ee9dc-0b00-4908-be32-c6a3efb425e2

Positron Annihilation Studies on Thin Film Solar Cells: CdSe and PbSe Quantum Dot Thin Films and $Cu(In_{1-x}Ga_x)Se_2$ Layered Systems

Proefschrift

ter verkrijging van de graad van doctor

aan de Technische Universiteit Delft,

op gezag van de Rector Magnificus prof. dr. ir. T.H.J.J. van der Hagen,

voorzitter van het College voor Promoties,

in het openbaar te verdedigen op

dinsdag 8 januari 2019 om 10.00 AM

door

Wenqin SHI

Master of Engineering in Optoelectronic and Information Function Materials,

Wuhan University of Technology, Wuhan, China

geboren te Wuhan, China

Dit proefschrift is goedgekeurd door de promotoren.

Samenstelling promotiecommissie bestaat uit:

Rector Magnificus,	voorzitter
Prof. dr. E.H. Brück,	Technische Universiteit Delft, promotor
Dr. S.W.H. Eijt,	Technische Universiteit Delft, copromotor

Onafhankelijke leden:

Prof. dr. B. Barbiellini	Lappeenranta University of Technology, Finland
Prof.dr.ir. A.H.M. Smets	Technische Universiteit Delft
Prof.dr.ir. J.R. van Ommen	Technische Universiteit Delft
Dr. A.J. Houtepen	Technische Universiteit Delft
Dr. W. Egger	Universität der Bundeswehr München, Germany

This research was financially supported by the China Scholarship Council (CSC). Part of the research was financially supported by ADEM, A green Deal in Energy Materials of the Ministry of Economic Affairs of The Netherlands, and by the European Commission under the 7th Framework Programme, Key Action: Strengthening the European Research Area, Research Infrastructures, Contract No. 226507, NMI3.

Keywords:

Solar cells, Quantum Dots, Positron Annihilation Spectroscopy, Ab-initio Calculations, Surface Composition, Surface States, CIGS, ZnO, Thin Films, Degradation, Vacancy, Grain Boundaries, Diffusion

ISBN: 978-94-028-1330-2

Printed in the Netherlands by Ipskamp ‖ https://proefschriften.net/

An electronic version of this dissertation is available at

http: //repository.tudelft.nl

Email: W.Shi-2@tudelft.nl; shiwenqin@hotmail.com

Contents

Chapter 1

Introduction

The French physicist Alexandre-Edmond Becquerel discovered the photovoltaic effect in an electrolytic cell in 1839. Since then, it took a comparatively long time before solar energy was effectively used to generate electricity. In 1905, Albert Einstein provided the basis for fundamental understanding of the photoelectric effect.[1] In 1918, the Polish chemist Jan Czochralski invented his groundbreaking growing method of high-quality crystalline silicon. Silicon-based solar cells first showed a significant development with cells with an efficiency of about 6% manufactured at Bell Laboratories in 1954[2]. Solar cells were first used to power satellites orbiting the earth, and then gained great interest for terrestrial applications in the 1970s because of the steep rise in oil prices. Since 2000, photovoltaic (PV) technology started to exhibit a fast development. The worldwide cumulative installed PV power has continuously increased exponentially between 2007 and 2018. Currently the largest share is installed in Europe, followed by the Asia Pacific Region, where most of the PV power is installed in Japan and China. Even though solar electricity still covers only a small fraction of the worldwide electricity supply (about 2% in 2016), solar electricity has a great potential to grow much faster than other technologies such as hydroelectricity, nuclear electricity, and wind electricity, both on the basis of its science and technology perspectives and since solar energy is by far the largest available form of renewable energy on earth. Besides, PV systems can be installed decentralized on individual roof, unlike hydro- and nuclear power plants that require large public or private investments.

This thesis focuses on two types of solar cell materials, namely semiconductor quantum dots (QDs) and ZnO:Al/CdS/Cu($In_{1-x}Ga_x$)Se_2 (CIGS) layered systems, that are of importance for the further development of QD and CIGS thin film solar cells. For the first system, we applied positron techniques to probe the surface composition and electronic structure of ligand-capped PbSe and CdSe semiconductor QDs embedded in thin films. For CIGS solar cells, we examined the stability and degradation mechanism of ZnO:Al window layer under 85%/85 ^{o}C damp heat conditions and investigated the layered structure of CIGS with an (In,Ga) compositional gradient using positron techniques.

1.1. Quantum dot solar cells

Colloidal quantum dots (QDs) are approximately spherically shaped semiconductor nanocrystals with a diameter in the range of typically 2 to 20 nm, corresponding to hundreds to hundred thousands of atoms. A QD consists of a semiconductor crystalline core which is capped by a layer of organic molecules with an anchoring endgroup that is attached to the nanocrystal (NC) surface and a hydrocarbon tail directed away from it (figure 1.1). When the size of the QD is comparable to the Bohr radius of the electron and the hole, the conduction band and valence band become discrete and the band gap increases with a decrease in size. This quantum confinement effect makes the properties of QDs highly distinguishable to bulk crystals, as the QDs possess strongly size-dependent optical and optoelectronic properties. The unique property of size-tunability in the electronic and optical properties has spurred much of the interest in view

of potential applications in optoelectronic technology including solar cells, light-emitting diodes (LEDs), photodetectors and field-effect transistors (FETs).

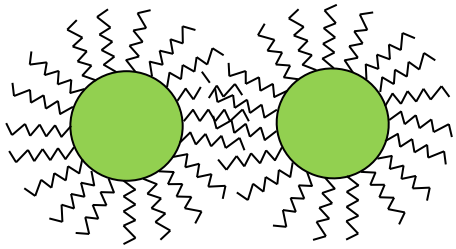

Figure 1.1. Schematic of NCs with hydrocarbon surface ligands

During the last decade, QD photovoltaic (PV) cells have attained a large increase in the power conversion efficiency (PCE), that increased from less than 1% in 2005 to 9.9% in 2016[3]. However, such an efficiency is still too low for large scale application like maturely commercialized Si-based solar cells (with a record efficiency of 25.6% for lab-based solar cells) and thin-film PV systems such as CdTe and $CuInGaSe_2$ (CIGS) (with record efficiencies of 21.5% and 22.6%, respectively).[4] Although QDs have two advantages over Si, namely a high absorption coefficient due to their direct band gap and the availability of inexpensive deposition techniques, the two key parameters of carrier mobility and carrier recombination rate limit the performance of QD solar cells. In order to improve the efficiency of QD solar cells significantly, it is required to develop effective transport of charge carriers between QDs, enhancing the charge carrier mobility and significantly reducing the concentrations of trap states at the surfaces of the QDs.

Atoms on a solid surface may exhibit dangling bonds, since they have less neighbouring atoms than interior atoms. In order to stay stable, a solid has a strong tendency to lower its surface energy by moving surface atoms away from lattice sites, by shifting inwardly or laterally in the process of surface reconstruction.[5,6] Relative to the bulk solid, QDs possess very high surface-to-volume ratios, which magnify significantly the contributions of the surface structure, composition and local electronic structure to the properties of the material. Under-coordinated surface atoms with dangling bonds often lead to electronic states with energies lying between the highest occupied and lowest unoccupied energy band of QDs, the so-called mid-gap states or surface states. These localized states behave as traps for electrons or holes, largely enhancing non-radiative surface recombination that limits the power conversion efficiency (PCE) of QD solar cells.[7] Shallow traps slow down charge transport through the solid, whereas deep traps capture both types of carriers, aiding their recombination. In order to improve the performance of QD solar cells, the concentration of mid-gap states should therefore be reduced substantially. Surface ligands attached to a QD are used to passivate the dangling bonds. Besides, they also play a vital role in the QD nucleation and growth, aiding to produce monodisperse size distributions and to induce chemical and colloidal stability of the QDs. The bonding between a QD surface atom and ligand molecules was described using Covalent Bond Classification scheme[8] in which the bonding types are classified according to the number of electrons provided

by ligands to form bonds with the surface atom. Figure 1.2 (a) illustrates the three ligand types. L-type ligands can donate two electrons and interact with surface sites, while X-type ligands can just donate one electron to form ligand-surface bond. Z-type ligands can accept two electrons and interact with electron-donating surface atoms.[8-11] In the case of CdSe QDs and PbSe QDs, phosphine oxides (R_3PO) and amines (RNH_2) (L-type ligands) are two-electron donors and can attach to the surface atoms (Cd and Pb) with dative covalent bonds, while carboxylate (RCOO-) and thiolate (RS-) (X-type ligand) are one-electron donors and can bind the cationic surface sites (Cd and Pb) with covalent bonds as presented in figure 1.2(b).

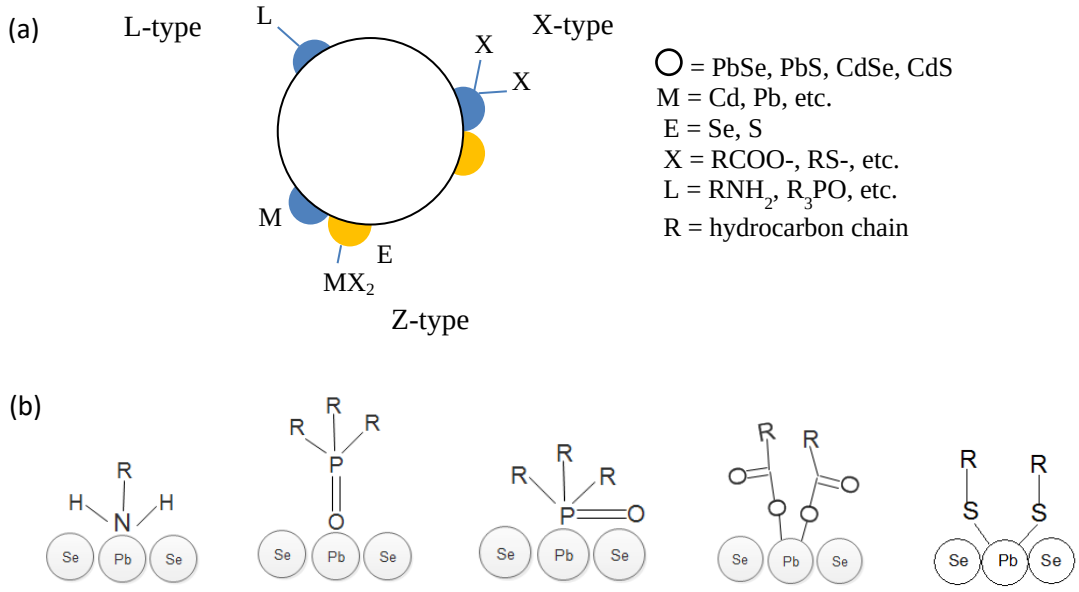

Figure 1.2. (a). Three Nanocrystal-ligand binding modes (L-type, X-type, and Z-type bonding); (b). The schematic of ligating atoms in various ligands (RNH_2, R_3PO, $RCOO^-$, and RS^-) attached to the Pb atoms at the surface of PbSe nanocrystals. Figure (a) is reproduced and adapted from ref. [9]

In order to gain a deeper understanding of the electronic structure of QDs and how it is affected by size, surface composition and type of capping ligand, a suite of experimental and computational techniques have been used previously. The effect of the size of QDs and ligands on opto-electronic properties is usually examined from the position of the band-edge absorption in the absorption spectra[12] and the photoluminescence peak in the photoluminescence spectra[12]. The quantum confinement of electrons in QDs as a function of particle size can also be observed experimentally using positron annihilation spectroscopy (PAS)[13] and X-ray absorption spectroscopy (XRAS)[14]. In XRAS, it can observe that the s states at the bottom of the conduction band shift to higher energies with a shift of $E_c \sim R^{-0.6}$ due to quantum confinement as the radius R of the CdSe QDs decreases. The mid-gap states created by the reconstructed surface structure, including the surface distortions, surface off-stoichiometry and the effect of surface ligands, were studied by both experimental and computational methods. The structural distortion of PbSe QDs was studied by X-ray diffraction (XRD) in comparison with computational analysis of the QD structure at the surface based on ab-initio total energy minimization methods.

Besides, the surface structure and electronic structure of CdSe and PbSe NCs with a bare surface[15,16], with weakly bound ligands, and with covalently bound ligands[17] were studied by ab-initio calculations. The bond length and bond angles are distorted when the size of NCs decreases, but the distorted surface structure does not create mid-gap states for stoichiometric NCs in the absence of passivated ligands.[16] A decrease in NC size was found to lead to an increase in the surface off-stoichiometry[18], which can also induce mid-gap states. Nevertheless, it was found from the ab initio calculations based on DFT that the mid-gap trap states can be removed through passivation of QD by an optimal number of attached ligands.[19] Passivating ligands can have various effects on the electronic structure. Some ligands such as hybrid ligands[20] can remove mid-gap states, while some other ligands like carboxylic acid ligands[17] can even introduce new mid-gap states.

Despite such insights, the relationship between passivation of NC surface sites and its electronic structure remains unclear due to several experimental reasons. First, there is no technique available that can directly reveal the reconstruction of the NC surface at an atomic-level. This means that only indirect methods can be used to study the surface structure. Secondly, the effect of passivated ligands on the electronic structure can be quite complicated. Surface passivation upon ligand binding is common, but not universally observed: some ligands introduce new mid-gap electronic states and increase the rate of non-radiative recombination.[10]

In this thesis, we use positron annihilation techniques to study the surface composition and electronic structure of ligand-capped semiconductor QDs embedded in thin films. Previous studies have indicated that positron-annihilation spectroscopy is a highly sensitive probe of the surface composition and electronic structure of semiconductor QDs.[21,22] Up to now, the cause of the high surface sensitivity, and a firm theoretical understanding of the underlying positron state was still lacking. In this thesis, it is demonstrated that the comparison of positron annihilation lifetime spectroscopy (PALS) studies of CdSe QDs with first-principles calculations within the WDA scheme developed and performed by Vincent Callewaert at the University of Antwerpen resolves the longstanding question regarding the nature of the positron state in semiconductor QDs, revealing the presence of a positron surface state for CdSe QDs, as described in Chapter 3. Eijt *et al.*[21,22] used the positron two-dimensional angular correlation of annihilation radiation (2D-ACAR) method to study CdSe QDs of various sizes and revealed the presence of selenium-rich surfaces due to the outward relaxation of Se atoms and inward relaxation of the Cd atoms. For PbSe QDs, Chai et al.[22] observed that positrons annihilate mostly with Se electrons in the surface layer and with electrons of O atoms from the oleate ligands bound to Pb ad-atoms at the NC surfaces. It was furthermore found that the positron can sensitively probe partial removal of oleate ligands together with the attached Pb ad-atoms from the surface. Here, we use 2D-ACAR to study the modifications of the surface composition and electronic structure of CdSe QDs (see Chapter 4) and PbSe QDs (see Chapter 5), caused by various ligands. For CdSe QDs, the observed change in the electron-positron momentum distributions caused by the ligands is much smaller than that for PbSe QDs. For PbSe QDs, the surface oxidation upon long-term exposure to air is also monitored by the positron method. (see Chapter 5)

1.2. CIGS solar cells

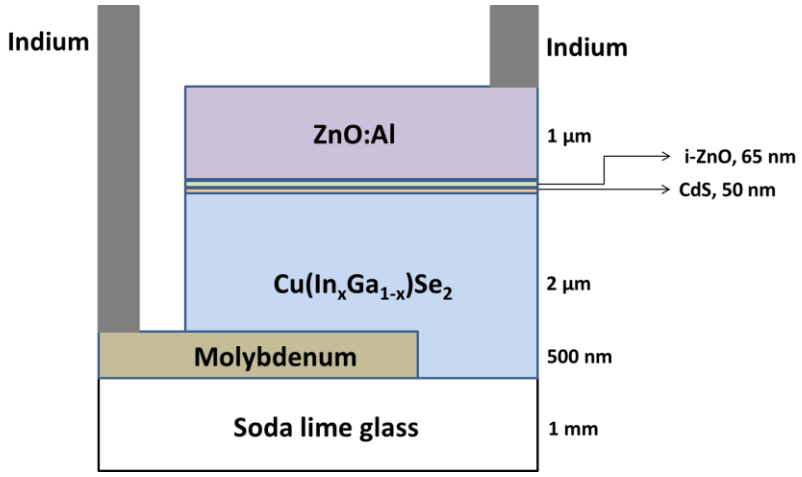

Figure 1.3. Schematic cross-section of a CIGS-based thin-film solar cell. The typical materials for the individual parts of the cell are given for each layer

$CuGaSe_2$ (CGS), $CuInSe_2$ (CIS), and their alloys $Cu(In_{1-x}Ga_x)Se_2$ (CIGS) have been intensively investigated for use as absorber layers in solar cells because of their high optical absorption coefficient, high chemical stability, and excellent radiation tolerance. CIGS has a chalcopyrite crystal structure and its band gap can be continuously tuned between 1.0 eV and 2.4 eV by varying the In/Ga and Se/S ratios. The low–band gap compositions so far systematically give the best performance. The CIGS-based solar cell is one of the most efficient technologies for thin film photovoltaics, with a record efficiency of 22.6%.[23] A typical CIGS-based solar cell consists of a ZnO:Al transparent conducting oxide (TCO) layer, an intrinsic ZnO buffer layer, a CdS buffer layer, the CIGS absorber layer, a Mo thin film metal electrode, and a soda lime glass substrate.(figure 1.3)

1.2.1. The ZnO doped with Al Transparent Conductive Oxide (TCO) layer

ZnO doped with Al (ZnO:Al) is one of the most promising transparent conducting oxides (TCOs) for electrode applications. It is highly transparent in the active wavelength range between 380 nm and 750 nm due to its wide band gap of 3.4 eV[24] and exhibits high conductivity of more than 10^3 $(\Omega \cdot cm)^{-1}$[25], which are important characteristics for application in optoelectronic devices. Besides, the cost of zinc is much lower than the rare indium in indium tin oxide (ITO), which is considered as the best TCO electric front contact for solar cells, making ZnO economically competitive. Besides ZnO:Al, other TCO materials such as ZnO:B and SnO_2:F are currently also widely investigated. In photovoltaic devices, the ZnO:Al layer serves three different purposes, namely passing the solar illumination from the cell surface to the absorber layer, enabling transport of charge carriers as front electrode, and inducing the formation of a heterojunction with the absorber layer.[26]

ZnO films for CIGS-based modules can be prepared by using chemical vapour deposition (CVD) and magnetron sputtering (radio frequency (RF)[27], either using a direct current (DC)[28], or mid-frequency (MF) deposition mode [29]). The three deposition methods can yield good film properties. The processing temperature is limited to 200℃ - 250℃ in order to be compatible with the remainder of the cell structure, since the ZnO film is the final layer to be deposited in CIGS-based module.

Despite the mentioned attractive features, there are two problems to consider for ZnO as TCO for solar applications. The first issue is the efficiency of doping of ZnO, related to the formation of point defects. Intrinsic point defects are deviations from the ideal structure caused by displacement or removal of lattice atoms. In ZnO, possible intrinsic defects are vacancies such as V_{Zn} and V_O, interstitials such as Zn_i and O_i, and antisite defects such as Zn_O and O_{Zn}. O_i, Zn_O, and O_{Zn} have a high formation energy, which means that they are difficult to form in large concentrations under normal conditions.[30] In order to obtain the desirable n type or p type doping, which is affected by the unwanted compensation of native defects, and to achieve a better control over the electrical conductivity, it is important to understand the nature of native defects in ZnO. Positron annihilation techniques are commonly used to investigate the properties of vacancy defects in ZnO that are either negatively charged or neutral, such as the Zn vacancy (V_{Zn}). Selim[31] and Weber[32] identified the relatively deep donor nature of oxygen vacancy (V_O) with an energy of 0.7 eV below conduction band under Zn-rich annealing by using positron annihilation spectroscopy (PAS)[31] associated with optical transmission measurements. Selim[31] also shows that for stoichiometric ZnO, the oxygen vacancy V_O is difficult to create, leading to difficulties in p-type doping with N, P, As.

Another issue is the stability of ZnO:Al thin films. Outdoor testing of chalcopyrite-based modules has generally demonstrated degradation rates of up to 4% per year.[33,34] In CIGS solar cells, chalcopyrites do not suffer from any form of light-induced degradation because of their extraordinary radiation hardness and their capability to passivate defects at comparably low temperatures.[35] However, the degradation of ZnO:Al properties can significantly affect the performance of CIGS solar cells, since ZnO plays an important role in these solar cells as a window layer, top electrode, and by forming part of the heterojunction.

Accelerated lifetime testing reveals that the increase of series resistance of CIGS solar cells during the degradation process constitutes an important factor in the decrease of the fill factor of the solar cells and, consequently, in the decrease of their efficiency. Exposing non-encapsulated films and devices to the conditions of 85 ℃/85% RH according to IEC/EN 61646[34] can mimic about 25-years of field exposure in Miami.[34] Many studies[36] revealed an important role played by the grain boundaries in the degradation process of ZnO:Al based CIGS solar cells. Theelen et al. [37] revealed that the change in optical and electrical properties during degradation could be explained by the following physical and chemical mechanisms. Atmospheric species like CO_2 and H_2O diffuse into the TCO top layer via the grain boundaries (in figure 1.4) and react with the ZnO to form $Zn(OH)_2$ complexes and Zn-based carbonates. This leads to significant increase

in the potential barriers at the grain boundaries and increased scattering of charge carriers at ionized impurities in the grain[37].

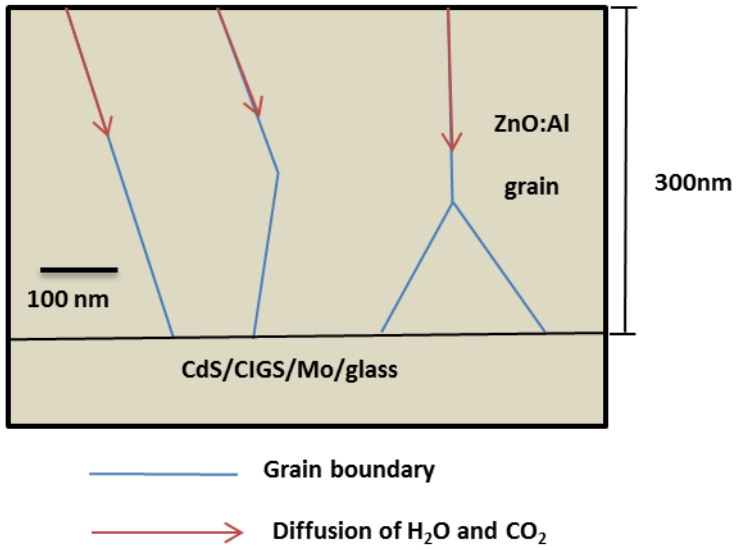

Figure 1.4. Schematic of the in-diffusion process of H_2O and CO_2 molecules into the ZnO:Al TCO layer via the grain boundaries.

In this thesis, a pronounced growth of vacancy clusters at the grain boundaries and mono-vacancies in the grains during the accelerated degradation of ZnO:Al based CIGS solar cells was revealed by Positron Annihilation Lifetime Spectroscopy (PALS) and Doppler Broadening Positron Annihilation Spectroscopy (DB-PAS) depth profiling. Such open-volume defects are created by reaction of in-diffusion molecules such as H_2O and CO_2 at the grain boundaries of ZnO:Al layer that locally removes Zn and O atoms. The increased open space at the grain boundaries imposes additional transport barriers, reducing the charge carrier mobility and increasing the series resistance of the ZnO:Al capped CIGS solar cells, leading to a further deterioration of their efficiency. (see Chapter 6)

1.2.2. The $Cu(In_{1-x}Ga_x)Se_2$ (CIGS) absorber layer

Many electrical characteristics of $Cu(In,Ga)Se_2$-based solar cells, including their current–voltage characteristics, are affected by specific properties of defects in the absorber layer. The doping in chalcopyrites is believed to be caused by native shallow defects, such as vacancies and antisites. These defects can have both donor and acceptor characters, and they can compensate each other, although the net result is usually a p-type CIGS absorber. The doping affects the band bending, determines the built-in voltage, and finally, limits the open circuit voltage and the efficiency of photovoltaic conversion. There are 12 intrinsic defects in $CuInSe_2$. The doping level can be controlled through the composition ratios applied during the synthesis process[38]. However, native defects can also act as recombination centres, which are detrimental to the efficiency.[39] In order to obtain highly efficient CIGS-based solar cells, it is important to

investigate the properties of the point defects, their correlation with the process conditions and how they affect the efficiency of CIGS-based solar cells. The Se flux was found to be a key parameter to control the crystal orientation for the three-stage evaporation methods.[40] By varying the Se flux used for CIGS thin film growth, the cell efficiency is suppressed at low Se flux values, correlating with an increase in vacancy-related defects.[41] By using a solution-based deposition approach, under insufficient Se supply level, a defective chalcopyrite layer with a high density of $(In, Ga)_{Cu}$ defects forms near the CIGS surface, leading to partial saturation of the device forward current and crossing of the J – V curves measured under dark and illuminated conditions.[42] Ga atoms are used to substitute In atoms in CIGS to adjust the bandgap. The efficiency reaches the highest values of more than 20% when the Ga/(Ga + In) ratio lies between 0.30 and 0.33.[43] Further gains in efficiency are hampered by the increased importance of defect mediated recombination of charge carriers (electrons and holes) with increasing Ga content.[44] It was found that the density of the mid-gap defects at 0.8 eV above the top of the valence band, which could either be the V_{Se}–V_{Cu} divacancy or the $(In,Ga)_{Cu}$ antisite defect, increases with increasing Ga/In ratio, reducing the open circuit voltage V_{oc} and the efficiency of the solar cell.[45,46] Further, the Cu contents is a key factor to form a strong p-type character of the as-grown CIGS absorber.[47,48]

In this thesis, we use Doppler Broadening Positron Annihilation Spectroscopy (DB-PAS) to study the depth dependence of the composition and vacancy-type defects in CIGS thin films grown when adjusting the synthesis parameters, i.e., the ramp temperature, selenization temperature, and substrate temperature during the selenization process. The positron can distinguish the layered structure in the CIGS film resulting from a gradient in Ga concentration applied during growth, but hardly sees any variation in vacancies for CIGS thin films produced when varying the parameters during the selenization process. (see Chapter 7)

1.3. Outline of thesis

This thesis contains 7 chapters, including the introduction and the theoretical aspects related to the theory of positrons and characterization techniques. The major topics of this thesis consist of two parts: (1) the investigation of surface structure, composition and ligand attachment of CdSe and PbSe quantum dot (QD) thin films probed using positron techniques in chapter 3, chapter 4 and chapter 5, and (2) the investigation of the degradation of and the presence of compositional gradients in ZnO:Al/CIGS solar cells by positron annihilation methods in chapter 6 and chapter 7.

In Chapter 3, the nature of the positron state in quantum dots is determined by using the positron annihilation lifetime technique combined with first-principles calculations. Our positron-annihilation lifetime spectroscopy (PALS) studies of CdSe QDs reveal the presence of a strong lifetime component with a lifetime in the narrow range of 358-371 ps, indicating abundant trapping and annihilation of positrons at the surfaces of the QDs. The ab-initio calculations of the positron wave function and lifetime employing a recent formulation of the Weighted Density

Approximation (WDA) developed and performed by Vincent Callewaert at the University of Antwerpen provide theoretical support for the existence of a positron surface state. Our study thus resolves the longstanding debate regarding the nature of the positron state in semiconductor QDs. This opens a new pathway to extract quantitative information on surface composition and ligand-surface interactions of colloidal QDs via positron techniques.

In Chapter 4, the modifications in electronic structure and composition at the surfaces of PbSe quantum dots (QDs) with various ligands are investigated by using the positron 2D-ACAR method. The positron can probe effectively the variation of the surface composition caused by various ligands. Also, for PbSe QDs, it is observed that the electron-positron momentum distributions are strongly affected by electronic coupling of valence electrons of neighbouring QDs when small ethyl diamine (EDA) molecules are applied as the ligands. Besides, the local oxidation process at the surfaces of colloidal nanocrystals resulting from long term exposure to air is monitored by the highly surface sensitive positron method.

In Chapter 5, the variation in the surface and electronic structure at the surfaces of CdSe quantum dots (QDs) caused by various ligands, i.e., stearic acid (SA), oleic acid (OA), oleylamine (OLA), and trioctylphosphine oxide (TOPO), is revealed by using positron two-Dimensional Angular Correlation of Annihilation Radiation (2D-ACAR) and Positron Annihilation Lifetime Spectroscopy (PALS). The positron can distinguish the variation in surface composition caused by various ligands that attach either via oxygen or nitrogen to the QD surface. However, for the case of CdSe QDs, the observed variation in the momentum distributions is much smaller than for the case of PbSe QDs presented in Chapter 5.

In Chapter 6, the mechanism of the degradation of ZnO:Al window layer for $Cu(In,Ga)Se_2$ (CIGS) solar cells was examined by using Positron Annihilation Lifetime Spectroscopy (PALS) and Doppler Broadening Positron Annihilation Spectroscopy (DB-PAS). The growth of vacancy clusters at the grain boundaries and mono-vacancies inside the grains is revealed by PALS and DB-PAS. Such open-volume defects are generated by reaction of in-diffusion molecules such as H_2O and CO_2 with ZnO:Al at the grain boundaries. The open volume imposes additional transport barriers at the grain boundaries, reducing the charge carrier mobility and further deteriorating the efficiency of the ZnO:Al capped CIGS solar cells as the resistance of the ZnO:Al layer increases. Notably, the evolution of the positron Doppler depth-profiles with the degradation time can be accurately described by a planar in-diffusion model, from which a diffusion coefficient of $35nm^2$/hour for the in-diffusion of molecules such as CO_2 and H_2O is extracted, in line with earlier studies based on determination of hydrogen (deuterium) depth profiles.

In Chapter 7, the vacancies and composition of $Cu(In,Ga)Se_2$ (CIGS) thin films is studied by using depth-resolved Doppler Broadening Positron Annihilation Spectroscopy (DB-PAS) and X-Ray Diffraction (XRD). the DB-PAS depth profiles using VEPFIT and S-W analysis reveal the presence of two layers, which is due to different concentrations of vacancy defects. The gradient in vacancy concentration is most probably caused by the inhomogeneous composition

with depth in the CIGS absorber layer. XRD spectra show that each sample has a non-uniform distribution of Ga and In, and consists of at least three phases with different $In_{1-x}Ga_x$ composition.

References

[1] A. Einstein, Annalen der Physik 17, 132-148 (1905).
[2] D. M. Chapin, C. S. Fuller, and G. L. Pearson, Journal of Applied Physics **25**, 676 (1954).
[3] C. M. Chuang, P. Brown, V. Bulovic, and M. G. Bawendi, Nature Materals **13**, 796 (2014).
[4] M. V. Kovalenko, Nature Nanotechnology 10, 994-997 (2015).
[5] F. J. Giessibl, Science **267**, 68 (1995).
[6] Cao, G., Wang, Y., Nanostructures and Nanomaterials (Imperial College Press, London, 2004)
[7] P. Nagpal and V. I. Klimov, Nature Communications 2, 486 (2011).
[8] M. L. H. Green, Journal of Organometallic Chemistry **500**, 127 (1995).
[9] N. C. Anderson, M. P. Hendricks, J. J. Choi, and J. S. Owen, Journal of the American Chemical Society **135**, 18536 (2013).
[10] M. A. Boles, D. Ling, T. Hyeon, and D. V. Talapin, Nature materials **15**, 141 (2016).
[11] A. J. Houtepen, Z. Hens, J. S. Owen, and I. Infante, Chemistry of Materials **29**, 752 (2017).
[12] T. M. Frederick and A. W. Emily, ACS Nano **4**, 3195 (2010).
[13] M. Weber, K. Lynn, B. Barbiellini, P. Sterne, and A. Denison, Physical Review B **66**, 041305 (2002).
[14] J. Lee, R. Meulenberg, K. Hanif, H. Mattoussi, J. Klepeis, L. Terminello, and T. van Buuren, Physical Review Letters **98**, 146803 (2007).
[15] A. Puzder, A. Williamson, F. Gygi, and G. Galli, Physical Review Letters **92**, 217401 (2004).
[16] A. Franceschetti, Physical Review B **78**, 075418 (2008).
[17] O. Voznyy, The Journal of Physical Chemistry C **115**, 15927 (2011).
[18] V. Petkov, I. Moreels, Z. Hens, and Y. Ren, Physical Review B **81**, 241304 (2010).
[19] D. Kim, D.-H. Kim, J.-H. Lee, and J. C. Grossman, Physical Review Letters **110**, 196802 (2013).
[20] A. H. Ip, S. M. Thon, S. Hoogland, O. Voznyy, D. Zhitomirsky, R. Debnath, L. Levina, L. R. Rollny, G. H. Carey, and A. Fischer, Nature nanotechnology **7**, 577 (2012).
[21] S. W. H. Eijt, A. (Tom) van Veen, H. Schut, P. E. Mijnarends, A. B. Denison, B. Barbiellini, and A. Bansil, Nature materials **5**, 23 (2006).
[22] L. Chai, W. Al-Sawai, Y. Gao, A. J. Houtepen, P. E. Mijnarends, B. Barbiellini, H. Schut, L. C. van Schaarenburg, M. A. van Huis, L. Ravelli, W. Egger, S. Kaprzyk, A. Bansil, and S. W. H. Eijt, APL Materials **1**, 022111 (2013).
[23] P. Jackson, R. Wuerz, D. Hariskos, E. Lotter, W. Witte, and M. Powalla, Physica Status Solidi (RRL) **10**, 583 (2016).
[24] Y. Chen, D. M. Bagnall, H.-j. Koh, K.-t. Park, K. Hiraga, Z. Zhu, and T. Yao, Journal of Applied Physics **84**, 3912 (1998).
[25] Kodigala, S., Cu(InGa)Se2 based thin film solar cells (Academic Press, Burlington MA, 2010)
[26] Ellmer, K., Klein, A., Rech, B., Transparent Conductive Zinc Oxide (Springer Verlag, Berlin, 2007)
[27] T. Minami, H. Sato, H. Nanto, and S. Takata, Japanese Journal of Applied Physics **24**, L781 (1985).
[28] Z. L. Pei, C. Sun, M. H. Tan, J. Q. Xiao, D. H. Guan, R. F. Huang, and L. S. Wen, Journal of Applied Physics **90**, 3432 (2001).
[29] R. J. Hong, X. Jiang, B. Szyszka, V. Sittinger, and A. Pflug, Applied Surface Science **207**, 341 (2003).
[30] M. D. McCluskey and S. J. Jokela, Journal of Applied Physics **106**, 071101 (2009).
[31] F. Selim, M. Weber, D. Solodovnikov, and K. Lynn, Physical Review Letters **99**, 085502 (2007).
[32] M. H. Weber, F. A. Selim, D. Solodovnikov, and K. G. Lynn, Applied Surface Science **255**, 68 (2008).
[33] R. Feist, S. Rozeveld, M. Mushrush, R. Haley, B. Lemon, G. Jennifer, N. Beth, N. Robert, R. Timm, S. Scott, T. Randy, T. Shari, and W. Charlie, Proc. 33rd IEEE PVSC San Diego, CA, May 11-16, 2008.

[34] M. Theelen and F. Daume, Solar Energy **133**, 586 (2016).
[35] J. F. Guillemoles, U. Rau, L. Kronik, H. W. Schock, and D. Cahen, Advanced Materials 11, 957 (1999).
[36] J. I. Kim, W. Lee, T. Hwang, J. Kim, S.-Y. Lee, S. Kang, H. Choi, S. Hong, H. H. Park, T. Moon, and B. Park, Solar Energy Materials and Solar Cells **122**, 282 (2014).
[37] M. Theelen, T. Boumans, F. Stegeman, F. Colberts, A. Illiberi, J. van Berkum, N. Barreau, Z. Vroon, and M. Zeman, Thin Solid Films **550**, 530 (2014).
[38] A. Polity, R. Krause-Rehberg, T. E. M. Staab, M. J. Puska, J. Klais, H. J. Möller, and B. K. Meyer, Journal of Applied Physics **83**, 71 (1998).
[39] E. Korhonen, K. Kuitunen, F. Tuomisto, A. Urbaniak, M. Igalson, J. Larsen, L. Gütay, S. Siebentritt, and Y. Tomm, Physical Review B **86**, 064102 (2012).
[40] S. Chaisitsak, A. Yamada, and M. Konagai, Japanese Journal of Applied Physics **41**, 507 (2002).
[41] M. M. Islam, A. Uedono, T. Sakurai, A. Yamada, S. Ishizuka, K. Matsubara, S. Niki, and K. Akimoto, Journal of Applied Physics **113**, 064907 (2013).
[42] Q. Cao, O. Gunawan, M. Copel, K. B. Reuter, S. J. Chey, V. R. Deline, and D. B. Mitzi, Advanced Energy Materials **1**, 845 (2011).
[43] M. Powalla, P. Jackson, W. Witte, D. Hariskos, S. Paetel, C. Tschamber, and W. Wischmann, Solar Energy Materials and Solar Cells **119**, 51 (2013).
[44] Y. Hirai, Y. Kurokawa, and A. Yamada, Japanese Journal of Applied Physics **53**, 012301 (2014).
[45] X. Hu, T. Sakurai, A. Yamada, S. Ishizuka, S. Niki, and K. Akimoto, Japanese Journal of Applied Physics **53**, 068008 (2014).
[46] J. T. Heath, J. D. Cohen, W. N. Shafarman, D. X. Liao, and A. A. Rockett, Applied Physics Letters **80**, 4540 (2002).
[47] S. Siebentritt., Thin Solid Films **403-404**, 1 (2002).
[48] S. Ishizuka, A. Yamada, P. Fons, and S. Niki, Progress in Photovoltaics: Research and Applications **21**, 544 (2011).

Chapter 2

Theory and Experimental techniques

2.1. Positron-solid interactions

2.1.1. Positron implantation and positron diffusion

The interaction process of a positron beam with a material can be described as schematically presented in figure 2.1. When energetic positrons enter the material, they will lose their kinetical energy mainly through fast inelastic collisions with core and valence electrons. Through such interactions the kinetical energy of the positrons is reduced to a few tens of eV in about 1 ps. The stopping profile of the monoenergetic positrons in the material can be expressed by the Makhovian distribution[1]:

$$P(z,E) = \frac{mz^{m-1}}{z_0^m} exp[-(z/z_0)^m] \quad (2.1)$$

where $z_0=1.13z_{ave}$ with the average positron implantation depth $z_{ave}=\alpha_p/\rho E^n$, ρ is the density of the medium, and E is the positron implantation energy. In the analysis, the parameters m=2, n=1.62, and α =3.6 $\mu g cm^{-2} keV^{-1.62}$ were used[2,3].

After thermalization, positrons diffuse randomly in the material, and the motion of positrons in the lattice can be described by using the Boltzmann equation[4]. This equation describes the motion of the positrons in the same way as the diffusion of other free carriers, but one needs to include the possible effect caused by positron trapping and annihilation in the bulk solid or defects. The positron diffusion coefficient D_+ and positron diffusion length L_+ can be calculated through the equations 2.2 and 2.3,

$$D_+ = \tau_r \frac{k_B T}{m^*} \quad (2.2)$$

$$L_+ = (\frac{D_+}{\lambda_{eff}})^{1/2} \quad (2.3)$$

in which

$$\lambda_{eff} = \frac{1}{\tau_b} + k(r) \quad (2.4)$$

is the effective positron annihilation rate, taking the positron trapping rate in defects $k(r)$ into account. τ_b is positron lifetime in the delocalised bulk state, and τ_r is the relaxation time for the dominant scattering mechanism (longitude acoustic phonon or optical phonon)[5]. m^* is the effective mass of the positron. D_+ can be determined in a defect-free reference sample. L_+ is usually measured with slow positrons diffusing back to the surface after their implantation[6] and can be directly obtained in the VEPFIT program, the principle of which can be found in reference[3]. In defect-free semiconductors at the room temperature the positron diffusion coefficient is typically 1-2 cm^2/Vs, and the diffusion length is typically 100-200 nm.[7]

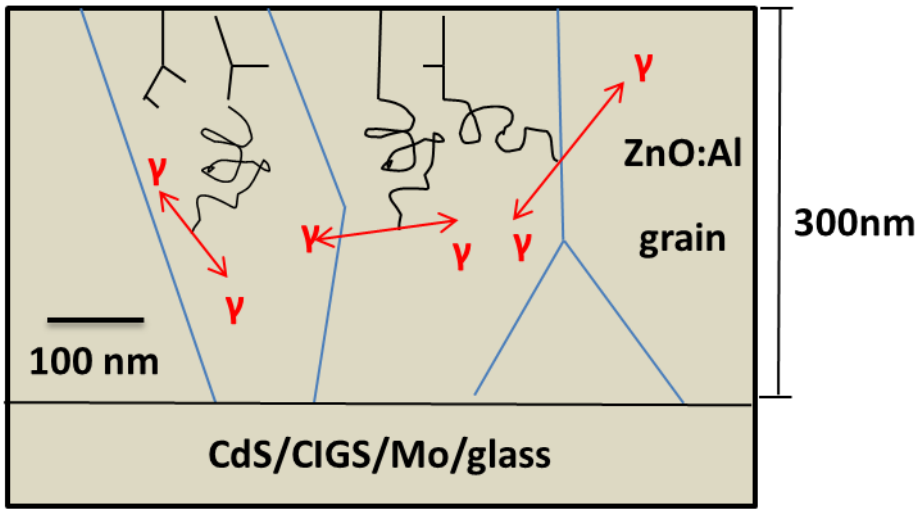

Figure 2.1. Interaction processes of positrons in a ZnO:Al thin film

2.1.2. Depth profiling of layers and defects

The profile as a function of depth of the annihilation parameters, such as S and W parameters in Doppler Broadening measurements or lifetime τ_i and corresponding intensity I_i in positron annihilation lifetime measurements can be modelled as the layered structure or defect profile convoluted by the implantation profile P(z, E) and is influenced by the positron diffusion.[6] Among the annihilation parameters, the S and W parameters measured by using the Doppler Broadening techniques can be fitted by VEPFIT program[3], which is based on the solution of the time-independent one-dimensional diffusion equation and takes into account the energy dependent positron implantation profiles P(z). One example of a Doppler depth profile, expressed as the S parameter as a function of positron energy and its fitted curve by VEPFIT program, is shown in figure 2.2(a). In applying the VEPFIT program, the fraction of positrons diffusing back to the surface (f_s) and annihilating in each layer (f_i ($i = 1, 2, 3$)) can be also calculated as shown in figure 2.2(b).

(a)

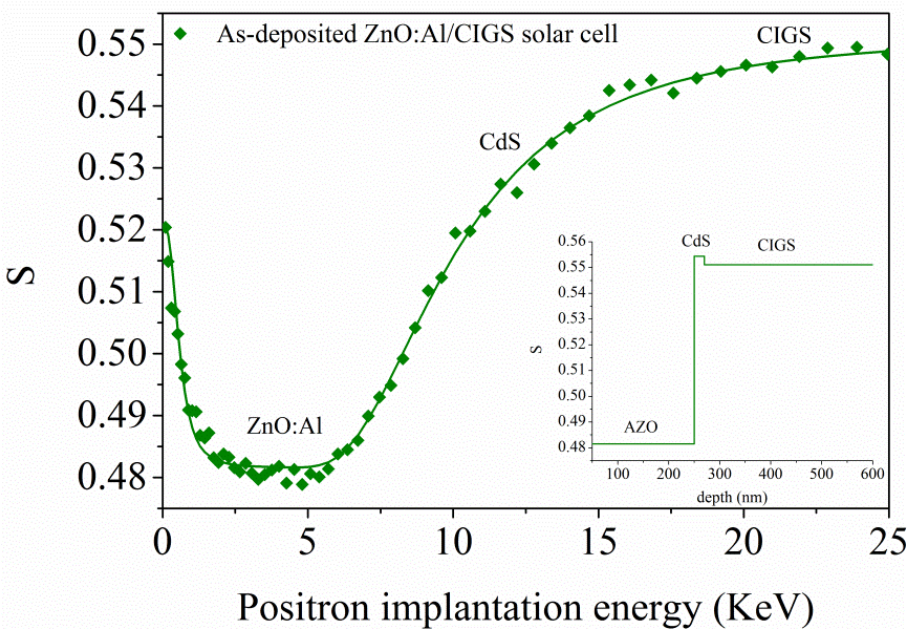

(b)

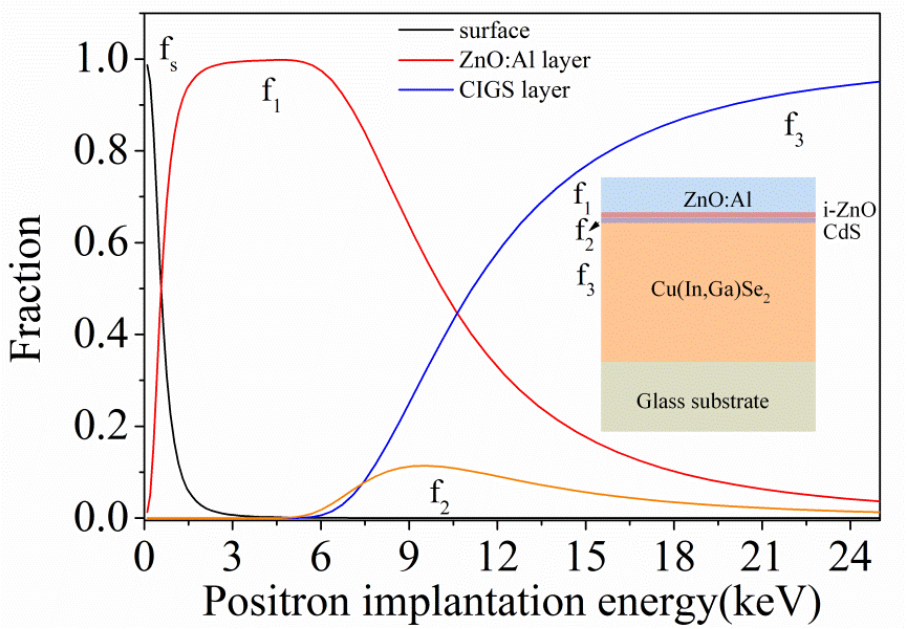

Figure 2.2.(a) S parameter as a function of positron implantation energy for the as-deposited ZnO:Al/CIGS solar cell. The layer structure used as model in the VEPFIT program is inserted in the figure. The curve through the data points was obtained by VEPFIT program. (b) Fraction of positrons that annihilate in each layer of an as-deposited ZnO:Al/CIGS solar cell as a function of positron implantation energy, extracted from the VEPFIT program; f_s – surface, f_1 – ZnO:Al/i-ZnO, f_2 – CdS, f_3 – CIGS.

2.2. Positron states

2.2.1. Positron states at vacancy-type defects

After implantation and thermalization, the positron is initially in a Bloch-like state in a perfect lattice. The positron wave function is focused in the interstitial region between the atoms of the crystal lattice, caused by the combined effects of the Coulomb repulsion from the ion cores and the electron-positron correlation. When the positron is trapped, at neutral or negatively charged open-volume defects such as atomic vacancies in the lattice, the positron wave function is localised at the defect, since the Coulomb repulsion is decreased caused by the missing ion core, and this contributes to lowering the potential sensed by the positron creating a local potential well. (figure 2.3) The positron annihilation rate and the positron-electron momentum distribution for the positron in the trapped state can be used to characterize the vacancies. In a vacancy defect, the positron lifetime is generally longer than the defect-free lattice, since the electron density is locally reduced. (see 2.3.2 equation 2.9) Besides, when the positron is trapped at the vacancy, the overlap of the wavefunction of positrons and core electrons is strongly reduced while wavefunction of valence electrons extends farther into the open space, which leads to increased annihilation probability with valence electrons and a corresponding sharper momentum distribution.

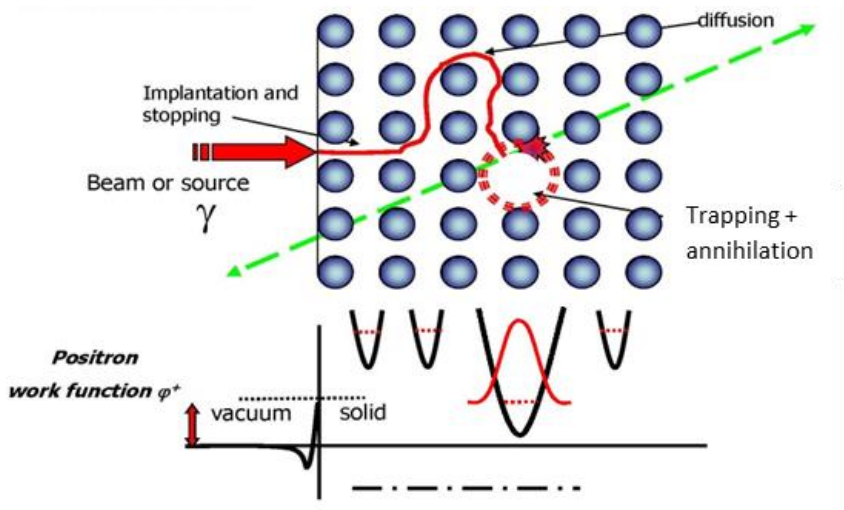

Figure 2.3. Potential well for a positron in a perfect lattice and vacancy defect in a lattice[1]

2.2.2. Positron states on nanocrystal surface

When positrons enter in the nanocrystal thin film, the majority of positrons is stopped by nanocrystal cores while a small fraction of positrons is stopped by capping ligands attached at the surface of nanocrystals, owing to the higher mass fraction of the QD cores.[8] After thermalization, the majority of positrons tends to be trapped in the image potential well[1] (figure 2.4) at the surface of the nanocrystals. The positron potential outside the surface is lower than

inside the QD, leading to a high possibility of trapping positrons in the surface potential well. Besides, nanocrystals' dimensions are typically of similar size or smaller than the thermal wavelength $\lambda_{th}^{+} = \frac{h}{\sqrt{3m^{*}k_{B}T}} \approx 50\left(\frac{300K}{T}\right)^{\frac{1}{2}}$ Å $\approx 5\,nm$ (at room temperature) and the scattering length of the positron[9], thus the positron cannot effectively diffuse in a QD after thermalization. This kind of surface trapping has already been suggested based on experiments in the positron studies of CdSe QDs[9,10] and PbSe QDs[8], for which positron annihilation spectroscopy was used to study properties and surface structure of nanocrystals. The positron lifetime for both PbSe QDs[8] and CdSe QDs show the values between 350 ps and 370 ps, characteristic of open space with a size comparable to trivacancies, with high intensity of 80% - 98%, suggesting that the majority of positrons is trapped at open space available at the surface.

The positron state can be calculated by using first-principle two-component density-functional theory (DFT), which is developed from the density-functional theory for calculating electronic structure in solids from first principles. The ground-state electron and positron densities can be calculated by solving of the one-particle Schrödinger equations for the electrons and the positron.[5] The potential sensed by the positron is the sum of the Coulomb potential $\Phi(n)$ caused by the electrons in the solid which is obtained from electronic structure calculation and the electron-positron correlation potential V_{corr} as follows:

$$V_{+} = \Phi(n) + V_{corr} \tag{2.5}$$

The electron-positron correlation potential can be calculated by using the local-density approximation (LDA).[11] When the positron is inside the solid, LDA can describe the positron correlation potential reasonably, since the screening cloud of electrons at the positron is quite isotropic. However, in the region close to the surface, the screening cloud is anisotropic with respect to the in-plane and out-of-plane directions, since the electron density decreases rapidly from the surface into the vacuum region. Since the LDA does not lead to the correct behaviour for the positron potential far away from the surface, an image potential well with the correct asymptotic behaviour of $V_{image} \sim 1/(z - z_0)$ is often used in the vacuum region. The positron potential in a solid is thus connected to the image potential at a certain position in the vacuum, introducing an empirical element into the calculations. Another theory based on weighted density approximation (WDA)[12] does not suffer from this flaw, since WDA leads to the correct behaviour far away from the surface.[12] More details on the calculations of the positron state can be found in references[5,7,12].

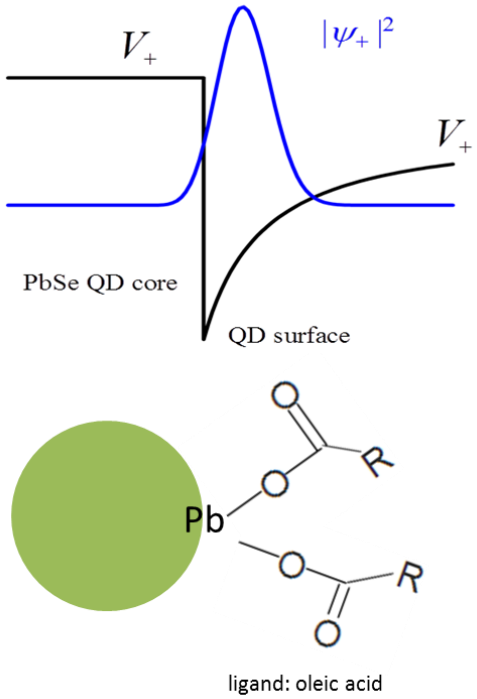

Figure 2.4. Schematic of positron state for a positron are trapped at the surface of the PbSe QDs capped with oleic acid ligands. Note that the schematic below denotes oleic acid ligands attatched Pb according to an X–type bonding.

2.2.3. Positronium

Positronium (Ps) is a bound state of a positron and an electron. Ps can not only be formed at the surface of metals or semiconductors, it can also be formed in polymers or long chain organic molecules in a solid where sufficiently large open space is present. The Ps work function at the surface can be written as follows:

$$\varepsilon_{Ps} = \varphi_- + \varphi_+ - \frac{1}{2}R_\infty \tag{2.6}$$

The binding energy of Ps in vacuum $\frac{1}{2}R_\infty \approx 6.8\ eV$, φ_- and φ_+ are electron and positron work function, respectively.

In vacuum, Ps can exist in two states, which are para-positronium (p-Ps) and ortho-positronium (o-Ps) with their lifetimes of 125 ps and 142 ns, respectively. p-Ps annihilates by emitting two γ-rays with an energy of 511 keV each, while o-Ps annihilates with emission of three γ-rays with a total energy of 1022 keV. When o-Ps is formed at the surface of the solid or inside an open volume of a material, the three-γ annihilation probability is reduced by pick-off annihilation, that is, the positron of the o-Ps may annihilate with an electron from the surrounding materials in a singlet state, with emission of two γ-rays instead of three. This causes a reduction of the

positronium lifetime, that can be used to estimate the size of the open space by using Tao-Eldrup model[13].

The presence of Ps can be identified by an analysis of the two-dimensional ACAR spectra and PALS spectra. The 2D-ACAR spectra is sensitive to the 2γ rays from p-Ps trapped in the open volumes (e.g. nanocavities or open spaces in polymers) or at the surface of the solid, but is not sensitive to the 3y o-Ps annihilations.[1] p-Ps annihilation leads to a relatively narrow peak in the 2D-ACAR spectra due to the low momentum of the thermalized e^--e^+ pair. The peak is asymmetric for Ps at the outside surface of materials, due to the fact that the p-Ps can be emitted from the surface. Besides, PALS can also be used to probe the Ps at the surface of materials and in open space in polymers or long chain organic materials. Lifetimes and intensities of p-Ps (with a lifetime of 125 ps in vacuum) and pick-off annihilation of o-Ps (with an effective lifetime of typically 1 ns or larger) can be resolved from the PALS spectra. The size and concentration of the open space can be estimated according to the lifetime and intensity of o-Ps that annihilates via pick-off by using Tao-Eldrup model[13].

2.3. Positron annihilation parameters

When a positron annihilates with an electron, the annihilation characteristics which include the momentum distribution of the annihilating electron-positron pairs and their annihilation rate can be calculated from first principles, characterizing the local electronic structure in a solid as seen by the positron. These calculated annihilation parameters can be compared directly with 2D-ACAR or CDBAR experiments and PALS experiments.

2.3.1. Momentum distribution of annihilating electron-positron pairs

In a non-interacting system, the momentum distribution of annihilating electron-positron pairs $\rho(\boldsymbol{P})$ can be written as follows:

$$\rho(\boldsymbol{P}) = \pi r_e^2 c \sum_j \left| \int d\boldsymbol{r} e^{-i\boldsymbol{P}\cdot\boldsymbol{r}} \psi_j^{ep}(\boldsymbol{r}) \right|^2 \tag{2.7}$$

Where **P** is the total momentum of the annihilating pair, the summation is over all occupied electron states j, $\psi_j^{ep}(\boldsymbol{r})$ is two-particle wave function when the electron and positron are at the same position r, and can be approximated as

$$\psi_j^{ep}(\boldsymbol{r}) = \psi_+(\boldsymbol{r})\psi_j(\boldsymbol{r})\sqrt{\gamma_j(\boldsymbol{r})} \tag{2.8}$$

$\psi_+(\boldsymbol{r})$ and $\psi_j(\boldsymbol{r})$ are the positron and electron wave functions obtained when positron-electron correlation effects are not included. The state-dependent enhancement factor $\gamma_j(\boldsymbol{r})$ is introduced to take into account the electron-positron correlation effects, which describes the distortion of the positron wave function from $\psi_+(\boldsymbol{r})$ and the enhancement of the electron density at the positron for the electron state j.

In practice, the calculation of momentum distribution can be simplified through various approximations. The simplest approximation is the independent-particle model (IPM) in which the positron and electron are independent particles and the short-range e^--e^+ correlation effect is neglected with $\gamma_j(\boldsymbol{r}) = 1$. That is justified because the momentum dependence of these correlation effects is weak. However, this approximation largely underestimates the annihilation rates due to the neglect of correlation effects. Also, approximation methods, e.g. Local Density Approach (LDA) and the Generalised Gradient Approximation (GGA) for the density functional are used in calculations of the electron-positron the momentum distribution.

2.3.2. Positron annihilation rate and lifetime

When the electron and positron densities as a function of position in the unit cell are known, the positron annihilation rate λ and mean lifetime τ can be calculated by

$$\lambda = \frac{1}{\tau} = \pi r_e^2 c \int d\boldsymbol{r} n_+(\boldsymbol{r}) n_-(\boldsymbol{r}) \gamma(\boldsymbol{r}, \boldsymbol{r}; [n_+, n_-]) \quad (2.9)$$

r_e is the classical radius of the electron, $\boldsymbol{r}$ the position vector, and c the speed of light. $\gamma(r, r; [n_+, n_-]$ is the enhancement factor, describing the increase in electron density due to the Coulomb attraction between a positron and an electron. $n_-(\boldsymbol{r}) = \sum_j \left|\psi_j(\boldsymbol{r})\right|^2$ and $n_+(\boldsymbol{r}) = |\psi_+(\boldsymbol{r})|^2$ are electron and positron densities, respectively.

2.4. Positron annihilation spectroscopy

Three positron annihilation techniques are used in this thesis, as shown in figure 2.5, namely 2-dimensional Angular Correlation of Annihilation Radiation (2D-ACAR), Doppler Broadening of Annihilation Radiation (DBAR), and Positron Annihilation Lifetime Spectroscopy (PALS). 2D-ACAR experiments measure the deviation of the annihilating photons from 180 °by a small angle $\Theta_{x,y} = p_{x,y}/m_0 c$, where $p_{x,y}$ is the transverse momentum component. Doppler broadening experiments detect the Doppler energy shift $\Delta E = cp_z/2$ of the annihilation photons, related to the momentum component of the annihilating photon-electron pair in the propagation direction of photons. Positron lifetime experiments measure the time difference between the moment a positron enters the material and its annihilation with an electron. All of the three positron techniques can be used to probe defects in materials. 2D-ACAR is very sensitive to the chemical environment of the annihilation site and the local electronic structure. DBAR can investigate the type and sometimes also the concentration of defects in materials while coincidence Doppler Broadening of Annihilation Radiation (CDBAR) is also very sensitive to the chemical information close to the annihilation site and can be used to identify the chemical environment of the defects. In CDBAR, coincidence measurements of the two annihilation photons are performed to reduce the background due to Compton scattering by adding a second detector in DBAR setup. The advantage of PALS is that it can distinguish different vacancy defect states simultaneously and estimate the size of the vacancy clusters in a quantitative

manner. Also, vacancy concentrations can be extracted in certain cases. On the other hand, PALS is rather insensitive to the chemical environment of the vacancy defects.

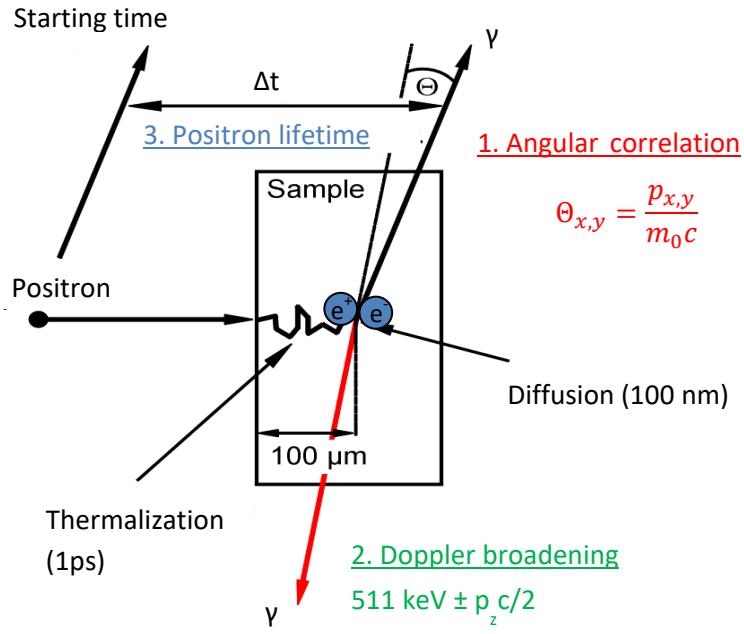

Figure 2.5. Schematic overview of positron annihilation and the three positron techniques used in this thesis

2.4.1. Two-dimensional Angular Correlation of Annihilation Radiation (2D-ACAR)

The 2D-ACAR technique is used to study the momentum distribution of annihilating electron-positron pairs in solids. This technique measures the angular deviation between the two coincident annihilation photons from 180˚. The momentum of positron-electron pair is conserved during the annihilation process. In the center-of-mass frame the total momentum of the electron-positron pair is zero and the annihilation photons are emitted in the opposite direction with an energy of $m_0c^2 \approx 511.0\, keV$ for each photon. In the lab frame, the momentum of the positron-electron pair in general will be non-zero, resulting in a small angle between the emitted coincident annihilating photons. The small deviation from collinearity generated in the p_x and p_y directions, as is shown in figure 2.6(a), can be written (for $p \ll m_0c$) as:

$$\theta \sim \sin\theta = \frac{p_x}{m_0 c} \tag{2.10}$$

$$\varphi \sim \sin\varphi = \frac{p_y}{m_0 c} \tag{2.11}$$

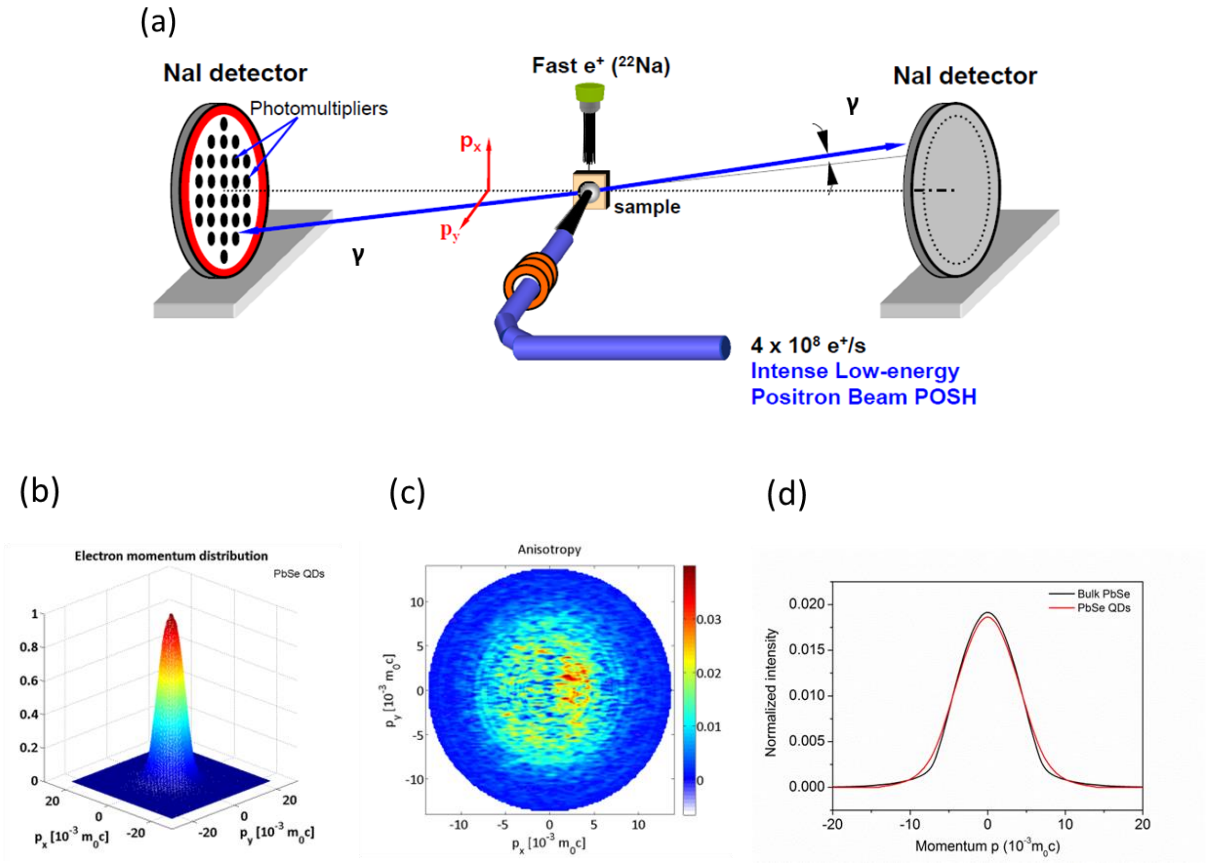

Figure 2.6. (a) A schematic of the setup (POSH-ACAR); (b) the 2-dimensional momentum distribution of electron-positron annihilation pairs; (c) Examples of the anisotropic part of the momentum distribution (d) 1D momentum distribution obtained by projection of the 2-dimensional momentum distribution after extracting the anisotropic part.

The annihilation photons are detected in the two position-sensitive detectors, and the position information (θ, φ) of γ rays in each annihilation event is stored in an incrementally updated 2D discrete array. The data $N(\theta, \varphi)$ collected here represents a two-dimensional projection of the three-dimensional momentum distribution $\rho(\boldsymbol{p})$ convoluted with the resolution function of the instrument $R(p_x, p_y)$.

$$N(\theta, \varphi) = N(p_x, p_y) = (\int \rho^{2\gamma}(\boldsymbol{p}) dp_z) * R(p_x, p_y) \tag{2.12}$$

2.4.2. Doppler Broadening of Annihilation Radiation (DBAR)

The momentum component p_z in the propagation direction z of the γ-rays results in a Doppler shift ΔE of the annihilation energy of $m_0c^2 \approx 511.0\, keV$, which amounts approximately to $\Delta E = cp_z/2$.

$$N(p_z) = \iint \rho^{2\gamma}(\boldsymbol{p}) dp_x dp_y \tag{2.13}$$

The peak-to-background ratio of the Doppler broadening measurement can be significantly improved by using two collinear detectors for coincident detection of the two annihilation photons, since the Doppler spectrum $N(E_{tot})$ with $E_{tot} = E_1 + E_2 \approx 1022\,keV$ does not contain a Compton contribution to the background. Furthermore, the energy resolution is better by a factor $\sqrt{2}$.

Two parameters S and W are used to characterize the momentum distribution obtained from a single detector DBAR measurement (figure 2.7), defined as the ratio of the counts in the central region of N(p) to the total number of the counts in the line, and the ratio of the counts in the wing regions of N(p) to the total number of the counts in the line, respectively. The S parameter mainly represents valence electrons characterized by their low electron momenta, while W also contains information on core electrons with higher momentum values. Therefore, they can be used to characterize the information of vacancies (size and concentration) and local chemical identity of atoms close to the annihilation site of positron, respectively. The coincidence Doppler data can also be used to identify the type of vacancy defects and information of local chemical compositions from the shape of N(p) directly, by a comparison to the momentum distribution of either a reference sample or deduced from ab-initio calculations.

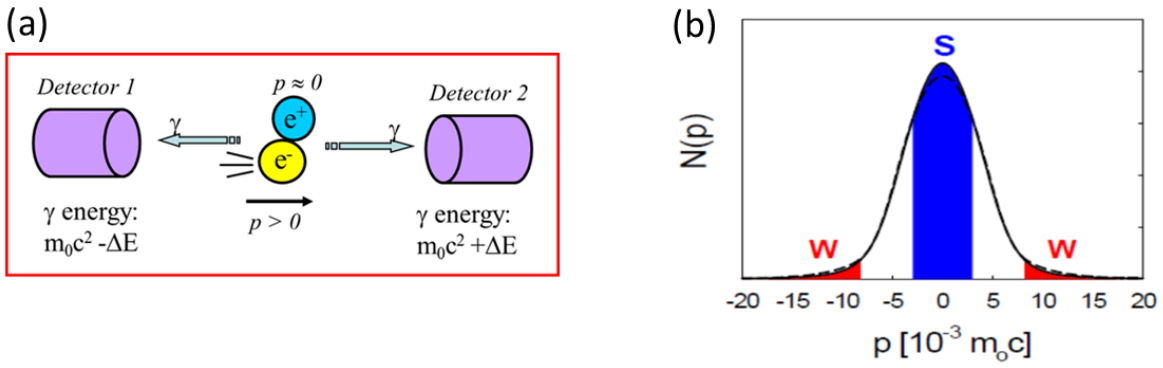

Figure 2.7. (a) A schematic overview of a DBAR experimental setup; (b) S, W parameter area of an electron-positron momentum distribution N(p).

2.4.3. Positron Annihilation Lifetime Spectroscopy (PALS)

The PALS technique is used to measure time difference between the moment the positron enters a material and its annihilation with an electron of the material. In a conventional positron lifetime setup, the positron source based on a positron-emitting isotope (e.g. ^{22}Na, ^{64}Cu, ^{58}Co) simultaneously provides a high-energy γ ray as a start signal when producing the positron. The lifetime can be determined by detecting the time difference between the start signal generated by the high-energy gamma photon from β^+ decay and the annihilation gamma of 511 keV. Such radioactive isotopes emit positrons with a broad range of energies up to the MeV range, leading to implantation of positrons up to the sub-millimeter range, excluding thin film studies. This problem can be overcome by using an intense variable mono-energetic low energy positron beam such as the NEPOMUC (Garching) or POSH beam (Delft). The PLEPS spectrometer

employs a pulsed low energy positron beam such that positrons arrive at samples at regular intervals of typically 40 ns, providing the start signal for determination of the positron lifetime.[14] The lifetime spectrum could be affected by the background noise, the width of the pulsed beam and the time resolution. The relative contribution by background noise can be decreased by increasing the intensity of the beam and the measurement time. The width of pulsed beam (< 200 ps) is controlled by a chopper and buncher and will affect the lifetime spectra. The time resolution arising from the size of the scintillators and the setting on the photomultiplier tubes cannot be neglected either. Thus, the experimental lifetime spectrum needs to be deconvoluted by the time instrument resolution function when decomposing the lifetime spectrum.

The experimental lifetime spectrum can be decomposed into a sum of decaying exponentials:

$$N(t) = N(0)\sum_t^n I_i \exp(-t/\tau_i) \tag{2.14}$$

where

$$\sum_i^n I_i = 1$$

so that

$$\frac{dN}{dt} = -N(0)\sum_i^n I_i/\tau_i \exp(-t/\tau_i) \tag{2.15}$$

In which n is the number of different annihilation states, τ_i is the lifetime of positron in state i, and I_i in the intensity of that state.

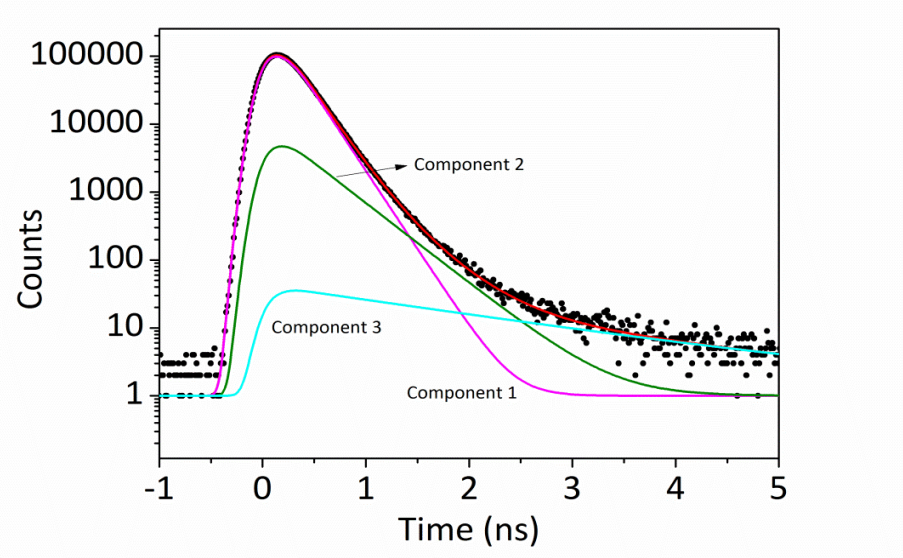

Figure 2.8. Experimental lifetime spectrum of a ZnO single crystal collected at a positron implantation energy of 16 keV, decomposed into three components by using the LT program[15]

References

[1] P. Schultz and K. G. Lynn, Reviews of Modern Physics **60**, 701 (1988).

[2] A. Vehanen, K. Saarinen, P. Hautojärvi, and H. Huomo, Phys. Rev. B **35**, 4606 (1987).

[3] A. van Veen, H. Schut, J. de Vries, R. A. Hakvoort, and M. R. Ijpma, AIP Conference Proceedings 218, 171 (1990).

[4] W. Brandt and N. R. Arista, Physical Review A **19**, 2317 (1979).

[5] M. J. Puska and R. M. Nieminen, Reviews of Modern Physics **66**, 841 (1994).

[6] R. Krause-Rehberg and H. S. Leipner, Positron Annihilation in Semiconductors - Defect Studies (Springer-Verlag, Berlin Heidelberg, Germany, 1999).

[7] F. Tuomisto and I. Makkonen, Reviews of Modern Physics **85**, 1583 (2013).

[8] L. Chai, W. Al-Sawai, Y. Gao, A. J. Houtepen, P. E. Mijnarends, B. Barbiellini, H. Schut, L. C. van Schaarenburg, M. A. van Huis, L. Ravelli, W. Egger, S. Kaprzyk, A. Bansil, S. W. H. Eijt, APL Materials **1** (2013).

[9] S. W. H. Eijt, A. (Tom) van Veen, H. Schut, P. E. Mijnarends, A. B. Denison, B. Barbiellini, and A. Bansil, Nature materials **5**, 23 (2006).

[10] M. Weber, K. Lynn, B. Barbiellini, P. Sterne, and A. Denison, Physical Review B **66**, 041305 (2002).

[11] E. Boroński and R. M. Nieminen, Physical Review B **34**, 3820 (1986).

[12] V. Callewaert, R. Saniz, B. Barbiellini, A. Bansil, and B. Partoens, Physical Review B **96**, 085135 (2017).

[13] D. W. Gidley, H.-G. Peng, and R. S. Vallery, Annual Review of Materials Research **36**, 49 (2006).

[14] W. Egger, P. Sperr, G. Kögel, and G. Dollinger, Physica status solidi (c) **4**, 3969 (2007).

[15] J.Kansy, Nuclear Instruments and Methods in Physics Research A **374**, 235 (1996).

Chapter 3

Nature of the Positron State in CdSe Quantum Dots

Abstract

Previous studies have shown that positron-annihilation spectroscopy is a highly sensitive probe of the electronic structure and surface composition of ligand-capped semiconductor Quantum Dots (QDs) embedded in thin films. Nature of the associated positron state, however, whether the positron is confined inside the QDs or localized at their surfaces, has so far remained unresolved. Our positron-annihilation lifetime spectroscopy (PALS) studies of CdSe QDs reveal the presence of a strong lifetime component in the narrow range of 358-371 ps, indicating abundant trapping and annihilation of positrons at the surfaces of the QDs. Furthermore, our ab-initio calculations of the positron wave function and lifetime employing a recent formulation of the Weighted Density Approximation (WDA) demonstrate the presence of a positron surface state and predict positron lifetimes close to experimental values. Our study thus resolves the longstanding question regarding the nature of the positron state in semiconductor QDs, and opens the way to extract quantitative information on surface composition and ligand-surface interactions of colloidal semiconductor QDs through highly sensitive positron-annihilation techniques.

This chapter is based on the published paper:

W. Shi*, V. Callewaert*, B. Barbiellini, R. Saniz, M. Butterling, W. Egger, M. Dickmann, C. Hugenschmidt, B. Shakeri, R. W. Meulenberg, E. Brück, B. Partoens, A. Bansil, and S. Eijt, Nature of the positron state in CdSe quantum dots, Physical Review Letters **121**, 057401 (2018)

(*These authors contribute equally to this work.)

3.1. Introduction

Colloidal semiconductor Quantum Dots (QDs) are drawing intense interest as potential functional building blocks for next-generation photovoltaic (PV) devices due to their special size-tunable opto-electronic properties. Solar cells based on PbS QDs recently reached promising efficiencies above 10%[1]. Relative to the bulk solid, QDs possess a very high surface-to-volume ratio, which greatly magnifies contributions of the surface structure, composition and electronic structure to their properties[2-4]. In order to prevent defect states in the band gap from dangling bonds of under-coordinated surface atoms, it is important to passivate such surface states via suitable ligand molecules, since imperfect passivation can severely limit the efficiency of QD solar cells[5]. For boosting the performance of QD-based PV devices, a deeper understanding of the electronic and surface structure of QDs capped with surface ligands is necessary. In this connection, recent years have witnessed innovative applications of X-ray absorption and positron-annihilation techniques [6-11] and the development of a wide range of computational modeling methods [12-15].

Studies have shown that positron techniques are effective probes of surface composition and electronic structure of semiconductor QDs[9,10,16,17]. However, the cause of the high surface sensitivity, and a firm theoretical understanding of the underlying positron state is still lacking. The first experimental positron studies of colloidal CdSe QDs by Weber *et al*. [9] demonstrated that positron Coincidence Doppler Broadening can sensitively probe the electronic structure of semiconductor QDs via their positron-electron momentum distributions (PEMDs), attributed to positron annihilation from a positron state confined inside of the QD, that has characteristics of a confined 'bulk'-like state. Later, Eijt *et al*.[10] revealed that the positron is mainly located at the surfaces of CdSe QDs, facilitated by the comparison of the PEMDs of CdSe QDs and bulk CdSe observed by positron 2D-ACAR (two-dimensional Angular-Correlation-of-Annihilation-Radiation) with the PEMD of bulk CdSe obtained from *ab-initio* calculations. The positron wave function was only schematically described as a 'shell'-like state at the surface of the QD. Notably, recent Positron Annihilation Lifetime Spectroscopy (PALS) measurements indicated the presence of a positron surface state for PbSe QDs as well[16].

In order to provide evidence of the positron surface state in CdSe QDs indicated by positron experiments, *ab-initio* calculations of the positron-surface interaction potential and the resulting positron wave function are essential. The positron wave function is subsequently used to calculate the annihilation probabilities, enabling direct comparison with PALS experiments. Positron states at solid surfaces were extensively studied in the past years[18-20]. However, unlike the case of a positron in a bulk solid, the screening cloud of electrons at the surface is strongly anisotropic and the positron correlation potential cannot be accurately described by the local-density approximation (LDA), which has proven to be reliable for the description of the bulk positron wave function in solids[21]. This has prevented a satisfactory theoretical treatment of the positron wave function at the surfaces of QDs, even in studies employing a combined LDA plus

corrugated mirror model (CMM) approach, where the erroneous behavior of the LDA in the vacuum region is empirically corrected.

In this Chapter, we demonstrate the existence of a positron surface state in CdSe QDs through quantitative and systematic comparison of PALS spectra with corresponding first-principles calculations. Two methods, namely, the LDA+CMM[22,23] and the recently developed implementation of the WDA[24, 25], are used to model the electron-positron correlation potential. In contrast to the standard implementation of the LDA+CMM, our calculations within the WDA show that the positron wave function is characterized consistently by the presence of a clear peak located at the surface of CdSe QDs, with calculated lifetimes close to the experimental values.

3.2. Experimental

CdSe QDs with a mean diameter of 6.5 nm were produced using the synthesis methods described in Ref. [26], which produces QDs nominally capped with both stearic acid (SA) and trioctylphosphine oxide (TOPO) ligands. In Ref. [26], we showed that the type of ligand present on the surface of the QD can be controlled during post-processing, so that only SA is left on the surface. Ligand exchange was then performed with three ligand types: oleylamine (OLA), oleic acid (OA), and TOPO. In this way, five unique samples were obtained: CdSe coated with SA/TOPO, SA, TOPO, OLA, and OA. CdSe QD layers with thicknesses in the range of several μm were produced by drop-casting of the solutions on 1×1 cm^2 ITO-coated glass substrates.

These thin-film samples were examined by PALS[27,28,19] using the pulsed low-energy positron lifetime spectrometer (PLEPS) instrument[29] of the neutron induced positron source (NEPOMUC) facility[30] at the Heinz Maier–Leibnitz Zentrum (MLZ) research reactor in Garching. Measurements were performed at selected positron energies between 1 and 18 keV. Around $4 \cdot 10^6$ counts were collected for each lifetime spectrum. The lifetime spectra were fitted by using the LT program[31].

3.3. Results and Discussion

3.3.1. Surface state and positronium lifetimes

Representative PALS spectra are shown in Figure 3.1(a) for 6.5-nm CdSe QDs. The spectra are remarkably similar in the short time region, showing only differences upon variation of the binding ligand in mainly the intensity of the long-lifetime component characteristic for ortho-positronium (o-Ps) formation. Satisfactory lifetime fits could be obtained using a three component decomposition, as is exemplified in Figure 3.1(b). The three components correspond to (1) para-positronium (p-Ps), (2) a positron lifetime of 370 ps, which is in the range of values indicating positron surface annihilation[16,32], and (3) ortho-positronium. In the fit, the instrumental resolution function is described by a sum of two Gaussian functions, obtained by measurement of the PALS spectra of p-doped SiC sample for each investigated positron

implantation energy, assuming a bulk p-SiC lifetime of 145 ps and surface lifetime of 385 ps[33]. In the analysis of the PALS spectra, a constraint of $I_{o\text{-}Ps} = 3I_{p\text{-}Ps}$ due to the spin multiplicity of the positronium states[34] was applied. Table 3.1 lists the obtained fitted parameters, that did not show any significant dependence on the positron implantation energy beyond 2 keV, indicating the homogeneity of the QD layers.

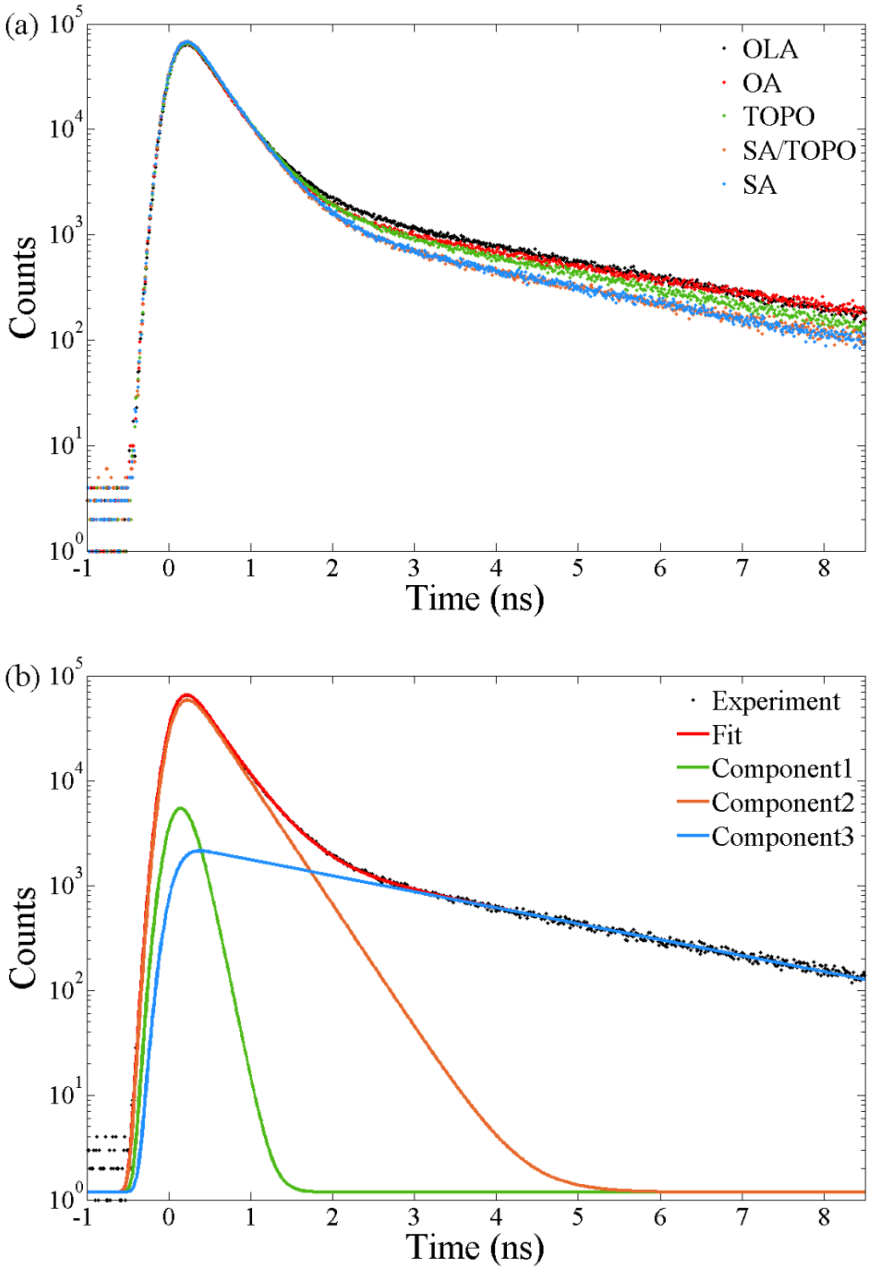

Figure 3.1. (a) Positron lifetime spectra of CdSe QDs capped with OLA, OA, TOPO, SA/TOPO, and SA ligands, collected at the positron implantation energy of 6 keV. (b) Data with TOPO ligands in (a) (solid circles) along with the corresponding fit (red full curve) and decomposition of the spectrum into three lifetime components (green, magenta, and blue lines) using the LT software.

Table 3.1. Positron lifetimes and intensities for CdSe QDs capped with five different ligands averaged over values obtained for five positron implantation energies in the range of 2-16 keV. Errors are standard deviations in the average values. Last column gives the range of fit variances.

CdSe QD capping ligand	I_1 (%)	I_2 (%)	I_3 (%)	τ_1 (ps)	τ_2 (ps)	τ_3 (ns)	Fit variance range
OLA	5.7 ±0.2	77 ±1	17.0 ±0.5	101 ±2	371 ±1	2.93 ±0.05	1.16 – 1.27
OA	5.4 ±0.8	78 ±3	16.2 ±2.5	101 ±13	363 ±1	3.29 ±0.15	1.33 – 1.55
TOPO	4.4 ±0.6	82 ±2	13.3 ±1.7	110 ±5	369 ±3	2.83 ±0.04	1.19 – 1.30
SA/TOPO	3.6 ±0.8	86 ±3	10.7 ±2.4	92 ±6	358 ±2	2.85 ±0.04	1.49 – 1.86
SA	3.9 ±0.9	84 ±4	11.7 ±2.7	100 ±22	364 ±2	2.84 ±0.04	1.38 – 1.69

The PALS study reveals the presence of a dominant (77%-86%) second lifetime component with lifetimes in the narrow range of 358-370 ps, *i.e*. significantly higher than the experimental positron lifetime of defect-free CdSe (275 ps [9]) and at most weakly depending on the type of ligand present. The longest lifetime component is in the range of 2.8-3.3 ns with an intensity of 10-17%, corresponding to o-Ps that forms in the open spaces between the carbon chains of surface ligands or at the surface of the QDs and annihilates via pick-off annihilation[16]. The o-Ps lifetimes indicate an open space size of about 0.7-0.8 nm[35,36]. The relative intensities of the second lifetime component and Ps are comparable to the estimated fractions of positrons stopped in the CdSe core and ligand shells, 88% and 12%, respectively, extracted from the mass-density-weighted volume fractions for the CdSe cores and ligand shells[16]. This provides further indication that Ps is formed in the ligands, while it strongly suggests that the intense second lifetime component arises mainly from the majority of positrons that are stopped and thermalize in the QD cores. In view of the small size of the QDs, the wave function of these positrons will have considerable overlap with the surfaces of the QDs and these positrons may thus easily trap in a surface state. The transition from a 'bulk'-like state confined in the QD to a surface state in the last processes of thermalization may occur for example via an Auger process[20].

Clearly, a satisfactory and robust decomposition of the PALS spectra into three components was obtained for all samples, with the shortest and longest lifetime component corresponding to p-Ps and o-Ps (pick-off) annihilation, respectively, and a dominant intermediate lifetime associated with positron surface state annihilation. In the analysis, the constraint of $I_{o\text{-}Ps} = 3I_{p\text{-}Ps}$ leads to p-Ps lifetimes of about 90-110 ps, *i.e*. close to the intrinsic (vacuum) lifetime of 125 ps. It should be noted that the time resolution (ranging from 260 ps to 280 ps) was not optimal and could be a factor of uncertainty in the quantitative determination of the (short) p-Ps lifetime. We checked

the reliability and robustness of the PALS analysis by comparison to another fitting scheme in which the lifetime of p-Ps is fixed at its vacuum value of 125 ps. In that case, satisfactory fits can also be obtained, but this leads to unphysically large deviations from the expected 1:3 ratio in p-Ps to o-Ps intensities in absence of strong magnetic fields. Importantly, however, the lifetimes and intensities of the second lifetime component remain nearly the same as in Table 3.1, demonstrating the robustness of the lifetime parameters characterizing the positron surface state.

3.3.2. First-principles calculations

In order to provide firm support for the positron surface state at the surfaces of QDs inferred from the PALS experiments, we have performed first-principles calculations of the positron ground state wave function and the corresponding positron annihilation lifetimes, employing the zero-positron-density limit of the two-component density functional theory[19, 37]. The first-principles electronic structure calculations of CdSe were performed using the PAW method[38] as implemented in VASP[39-41]. The plane wave cutoff energy was set to 357 eV in all calculations. Brillouin zone integration was performed using an $11\times11\times7$ Γ-centered k-grid for the hexagonal bulk cell, and two-dimensional grids of a comparable density were used for the slab calculations. Electron-electron exchange and correlation was described with the Perdew-Burke-Ernzerhof functional[42]. Surfaces were modeled in a slab geometry with a vacuum region of at least 1.5 nm. The lattice parameters and atomic positions were optimized for the bulk unit cell prior to the construction of the slab models in which ionic positions were optimized but lattice parameters were kept fixed. We only considered non-polar surfaces of CdSe.

For the positron ground state calculations, we considered two models to describe the electron-positron correlation potential, namely, LDA+CMM, and WDA. In CMM[22], the erroneous LDA potential[43] in the vacuum regions of the simulation cell is empirically corrected to give the correct asymptotic $\sim 1/(z\text{-}z_0)$ behavior. For positron lifetime calculations, we set the enhancement factor γ[44] to unity wherever the image potential was imposed, instead of using the LDA enhancement. Indeed, since the LDA enhancement factor implicitly assumes that the screening electron cloud is attached to the positron, its use is inconsistent with the use of the image potential since the screening cloud resides at the surface of the material[23]. In contrast, the WDA has the correct asymptotic behavior far away from the surface, and hence it does not require an empirical correction of the potential and the enhancement factor [21], but corrections are necessary in order to reproduce the experimental bulk lifetimes[24,45,46]. Here we apply the shell partitioning method, treating the Cd(5s), Cd(4d), S(4s) and Se(4p) electrons as valence electrons, and a modified screening charge Q[24], assumed to be equal to the charge of a single electron in earlier work[45,46]. In this way, an adequate description of the screening can be obtained, which in turn can be expected to yield a good description of the electron-positron interaction potential at the surface. The details of our implementation of both models can be found in Refs. [24,47].

Turning first to LDA+CMM results, the procedure of Ref. [47], we obtained an image potential reference plane at $z_0 = 1.8 \pm 0.1$ a.u. (1 a.u. = 0.0529nm) from the topmost atom at the surface for both the $(10\bar{1}0)$ and $(11\bar{2}0)$ surfaces. Neither of the calculated positron lifetimes of respectively 251 ps and 257 ps are, however, near the range of the experimental values $\tau = 358 - 371$ ps. In fact, these values are close to the LDA bulk value 246 ps, which is to be expected since the resulting positron state is seen to reside mostly inside the quantum dot (Figure 3.2(a)).

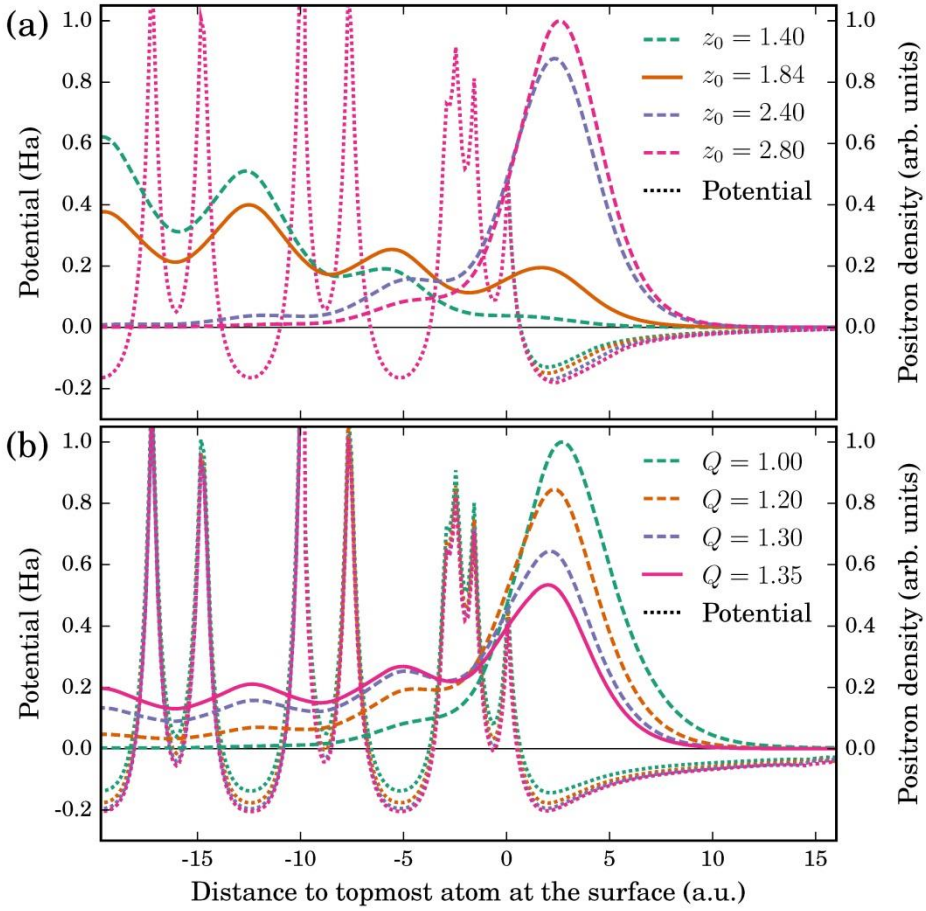

Figure 3.2. Results of the positron calculations at the CdSe $(10\bar{1}0)$ surface with (a) the LDA+CMM model, and (b) the WDA approach. Full curves show the positron densities (normalized to the highest density in the plotted region) with z_0=1.837 a.u. and Q=1.35 determined from the background edge and the bulk lifetime, respectively. Dashed lines show the effect of variation of the parameters. Total potentials (Coulomb and correlation) are given by dotted lines. All curves give averages over the planes parallel to the surface.

In the WDA calculations, we find that a modified screening charge of Q=1.35 reproduces the experimental *bulk* lifetime of 275 ps in CdSe [9]. Using this Q value, we find a positron surface state at both considered surfaces, in a sharp contrast to the LDA+CMM results, even though the tails of the states penetrate several layers into the material as seen in Figure 3.2(b). The

computed energy difference of 0.18 eV between the shown state and the first bulk state for the CdSe $(10\bar{1}0)$ slab confirms that these results indeed correspond to true surface states rather than surface resonances. The energy difference further shows that thermal excitation from the surface to the bulk state is negligible. The WDA-based lifetimes are much closer to the experimental values than the LDA+CMM, with values of 328 ps and 333 ps for the $(10\bar{1}0)$ and $(11\bar{2}0)$ surfaces, respectively, demonstrating that these computations provide a good description of the positron state at the surfaces of CdSe. It is highly satisfying that the Q value fitted for the bulk provides a good description of the surface state and its positron lifetime value as well.

Moreover, the WDA provides a fundamental conceptual advance over the LDA+CMM scheme for the following reasons. (1) Unlike LDA+CMM, the asymptotic behavior of the potential in WDA away from the surface is not imposed by hand in an ad hoc manner, but it arises naturally through a proper description of the underlying electron-positron correlation cloud. (2) The WDA enhancement factor varies continuously from the bulk into the vacuum as it is obtained by the computed screening cloud, while in LDA+CMM it is abruptly replaced by unity when crossing the z_0 boundary into the vacuum region. And, (3) the Q parameter in WDA involves a relatively simple bulk computation, while the z_0 parameter in LDA+CMM not only depends on the surface exposed but it is also difficult to generalize for surface geometries beyond a flat surface.

We finally investigate the sensitivity of the lifetimes and positron states to variation of z_0 and Q. Our purpose is to determine which parameter values reproduce exactly the measured lifetimes and examine the corresponding surface state. Figure 3.3(a) shows that in the LDA+CMM, in order to achieve consistency between the calculated and measured lifetimes, we need to shift the calculated z_0 to $z_0 \approx 2.4$ a.u.. Figure 3.2(a) shows that this leads to strong localization of the positron state at the surface, overlapping significantly only with the topmost few Cd-Se layers. This demonstrates that also within the LDA+CMM the measured lifetimes indicate the presence of a surface state. Within the WDA, we can obtain exact agreement with the measured lifetime by a slight change of Q=1.35, which fits the bulk lifetime, to Q=1.28-1.30 (Fig. 3.3(b)). The slightly reduced Q value at the surface likely reflects a decreased overlap of the positron with Cd(4d)-electrons, consistent with the experimental results of Ref. [10]. Note that the WDA predicts a significant penetration of the positron surface state into the bulk of the dots both for Q=1.35 and Q=1.28-1.30, as shown in Figure 3.2, indicating a qualitative difference with the LDA+CMM predictions at $z_0 \approx 2.4$ a.u.

Our analysis shows that LDA and LDA+CMM as well as the WDA are able to reproduce both bulk and surface lifetimes with a single adjustable parameter. However, LDA+CMM is unable to predict a surface state without having as input the corresponding experimental lifetime, while this is not the case for WDA, demonstrating its more advanced predictive capabilities. Finally, we note that the WDA has the potential to be quantitatively superior in applications that probe finer details of the positron-electron correlation and positron wavefunction.

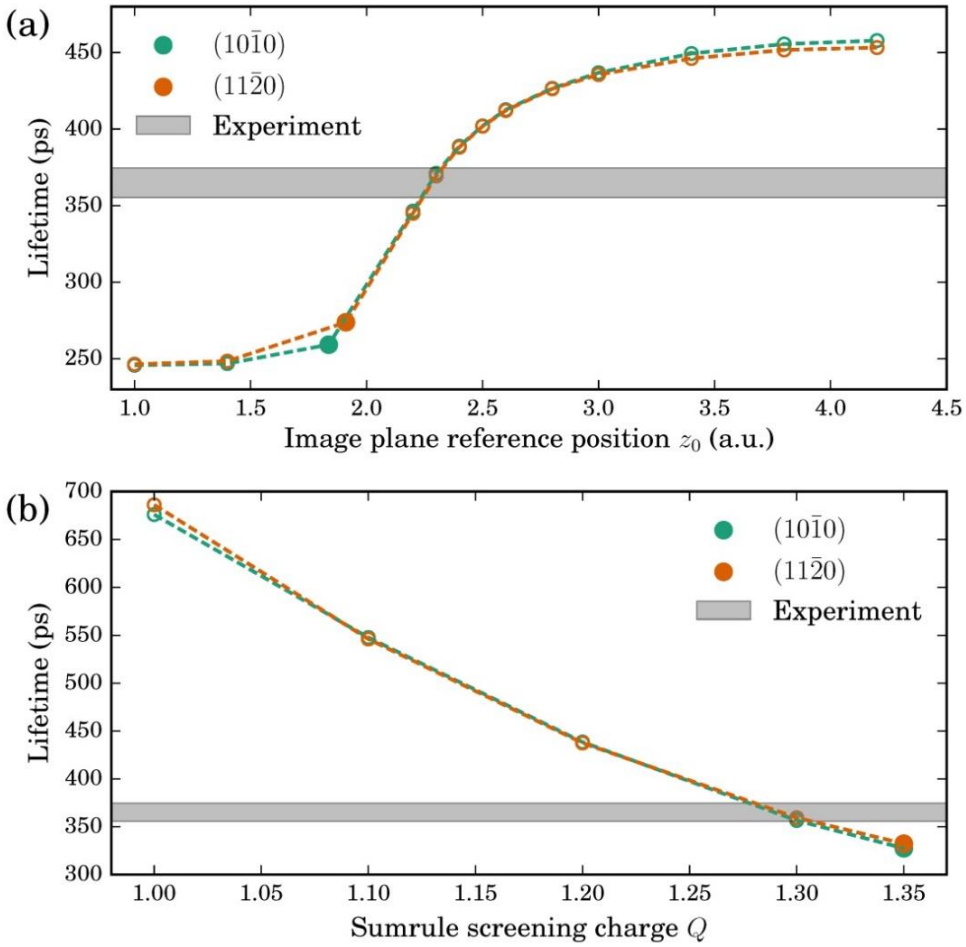

Figure 3.3. Computed positron lifetimes using (a) the LDA+CMM and (b) WDA for different values of the image potential reference plane z_0 and screening charge Q. Filled symbols indicate lifetimes calculated with z_0=1.837 a.u. determined from the background edge and Q=1.35 that fits the bulk lifetime, respectively. The gray area indicates the range of experimentally measured positron lifetimes at the surface.

3.4. Conclusions

Our in-depth PALS measurements of CdSe QDs demonstrate abundant trapping and annihilation of positrons at the surfaces of the QDs. Our parallel first-principles calculations within our WDA scheme confirm the existence of a positron surface state with calculated lifetimes that are close to the experimental values. Our work thus resolves the longstanding controversy concerning the nature of the positron state in QDs. We also demonstrate predictive capabilities of the WDA, and its conceptual superiority over conventional schemes such as the LDA+CMM, opening a new pathway for unraveling the complex behavior of positrons at the surface of QDs, which would allow us to obtain quantitative information on PEMDs of colloidal

QDs. Our study thus provides a robust basis for the application of positron annihilation spectroscopy as a highly surface-sensitive tool for probing surface compositions and ligand-surface interactions of colloidal semiconductor QDs.

References

[1] A. Stavrinadis, S. Pradhan, P. Papagiorgis, G. Itskos, and G. Konstantatos, ACS Energy Lett. **2**, 739 (2017).

[2] M. A. Boles, D. Ling, T. Hyeon, and D. V. Talapin, Nature Mater. **15**, 141 (2016).

[3] O. Voznyy and E.H. Sargent, Phys. Rev. Lett. **112**, 157401 (2014).

[4] F.D. Ott, L.L. Spiegel, D.J. Norris, and S.C. Erwin, Phys. Rev. Lett. **113**, 156803 (2014).

[5] A.H. Ip *et al*., Nature Nanotech. **7**, 577 (2012).

[6] J.R.I. Lee, R.W. Meulenberg, K.M. Hanif, H. Mattoussi, J.E. Klepeis, L.J. Terminello, and T. van Buuren, Phys. Rev. Lett. **98**, 146803 (2007).

[7] J. R.I. Lee *et al*., Nano Lett. **12**, 2763 (2012).

[8] J. T. Wright and R. W. Meulenberg, Appl. Phys. Lett. **101**, 193104 (2012).

[9] M.H. Weber, K.G. Lynn, B. Barbiellini, P.A. Sterne, and A.B. Denison, Phys. Rev. B **66** 041305 (2002).

[10] S. W. H. Eijt, A. van Veen, H. Schut, P. E. Mijnarends, A. B. Denison, B. Barbiellini, and A. Bansil, Nature Mater. **5**, 23 (2006).

[11] S.K. Sharma, K. Sudarshan, P. Maheshwari, D. Dutta, P.K. Pujari, C.P. Shah, M. Kumar, and P. Bajaj, Eur. Phys. J. B **82**, 335 (2011).

[12] D. Kim, D.-H. Kim, J.-H. Lee, and J. C. Grossman, Phys. Rev. Lett. **110**, 196802 (2013).

[13] A. Puzder, A.J. Williamson, F. Gygi, and G. Galli, Phys. Rev. Lett. **92**, 217401 (2004).

[14] V. Petkov, I. Moreels, Z. Hens, and Y. Ren, Phys. Rev. B **81**, 241304 (2010).

[15] A. Franceschetti, Phys. Rev. B **78**, 075418 (2008).

[16] L. Chai *et al.*, APL Materials **1**, 022111 (2013).

[17] W. Shi, S. W. H. Eijt, C. S. Suchand Sandeep, L. D. A. Siebbeles, A. J. Houtepen, S. Kinge, E. Brück, B. Barbiellini, and A. Bansil, Appl. Phys. Lett. **108**, 081602 (2016).

[18] M. J. Puska and R. M. Nieminen. Rev. Mod. Phys. **66**, 841 (1994).

[19] F. Tuomisto and I. Makkonen, Rev. Mod. Phys. **85**, 1583 (2013).

[20] S. Mukherjee, M.P. Nadesalingam, P. Guagliardo, A.D. Sergeant, B. Barbiellini, J.F. Williams, N.G. Fazleev, and A.H. Weiss, Phys. Rev. Lett. **104**, 247403 (2010).

[21] A. Rubaszek, Phys. Rev. B **44**, 10857 (1991).

[22] R. M. Nieminen and M. J. Puska, Phys. Rev. Lett. **50**, 281 (1983).

[23] R. M. Nieminen, M. J. Puska, and M. Manninen, Phys. Rev. Lett. **53**, 1298 (1984).

[24] V. Callewaert, R. Saniz, B. Barbiellini, A. Bansil, and B. Partoens, Phys. Rev. B **96**, 085135 (2017).

[25] V.A. Chirayath, V. Callewaert, A.J. Fairchild, M.D. Chrysler, R.W. Gladen, A.D. Mcdonald, S.K. Imam, K. Shastry, A.R. Koymen, R. Saniz, B. Barbiellini, K. Rajeshwar, B. Partoens, and A.H. Weiss, Nature Comm. **8**, 16116 (2017).

[26] B. Shakeri and R. W. Meulenberg, Langmuir **31**, 13433 (2015).

[27] R. Krause-Rehberg, and H. Leipner, *Positron Annihilation in Semiconductors - Defect Studies*, (Springer Verlag, Berlin, 1999).

[28] P.J. Schultz, and K.G. Lynn, Rev. Mod. Phys. **60**, 701 (1988).

[29] P. Sperr, W. Egger, G. Kögel, G. Dollinger, C. Hugenschmidt, R. Repper, and C. Piochacz, Appl. Surf. Sci. **255**, 35 (2008).

[30] C. Hugenschmidt, B. Löwe, J. Mayer, C. Piochacz, P. Pikart, R. Repper, M. Stadlbauer, and K. Schreckenbach, Nucl. Instr. Meth. A **593**, 616 (2008).

[31] D. Giebel, and J. Kansy, Phys. Proc. **35**, 122 (2012).
[32] F. Plazaola, A.P. Seitsonen, M.J. Puska, J. Phys.: Condens. Matter **6**, 8809 (1994).
[33] W. Egger, P. Sperr, G. Kögel, M. Wetzel, and H. J. Gudladt, Appl. Surf. Sci. **255**, 209 (2008).
[34] K. G. Lynn, W. E. Frieze, and P. J. Schultz, Phys. Rev. Lett. **52**, 1137 (1984).
[35] D. W. Gidley, H.-G. Peng, and R.S. Vallery, Ann. Rev. Mater. Res. **36**, 49 (2006).
[36] P. Crivelli, U. Gendotti, A. Rubbia, L. Liszkay, P. Perez, and C. Corbel, Phys. Rev. A **81**, 052703 (2010).
[37] E. Boroński and R. M. Nieminen, Phys. Rev. B **34**, 3820 (1986).
[38] P. Blöchl, Phys. Rev. B **50**, 17953 (1994).
[39] G. Kresse and J. Furthmüller, Comp. Mater. Sci. **6**, 15 (1996).
[40] G. Kresse and J. Furthmüller, Phys. Rev. B **54**, 11169 (1996).
[41] G. Kresse and D. Joubert, Phys. Rev. B **59**, 1758 (1999).
[42] J. P. Perdew, K. Burke, and M. Ernzerhof, Phys. Rev. Lett. **77**, 3865 (1996).
[43] N. D. Drummond, P. López Ríos, R. J. Needs and C. J. Pickard, Phys. Rev. Lett. **107**, 207402 (2011).
[44] J. Laverock, T. D. Haynes, M. A. Alam, S. B. Dugdale, Phys. Rev. B **82**, 125127 (2010).
[45] A. Rubaszek, Z. Szotek, and W. M. Temmerman, Phys. Rev. B **58**, 11285 (1998).
[46] A. Rubaszek, Z. Szotek, and W. M. Temmerman, Acta Phys. Pol. A **95**, 652 (1999).
[47] V. Callewaert, K. Shastry, R. Saniz, I. Makkonen, B. Barbiellini, B. A. Assaf, D. Heiman, J. S. Moodera, B. Partoens, A. Bansil, A. H. Weiss, Phys. Rev. B **94**, 115411 (2016).

Chapter 4

Ligand-Surface Interactions and Surface Oxidation of Colloidal PbSe Quantum Dots Revealed by Thin-film Positron Annihilation Methods

Abstract

Positron Two Dimensional Angular Correlation of Annihilation Radiation (2D-ACAR) measurements reveal modifications of the electronic structure and composition at the surfaces of PbSe quantum dots (QDs), deposited as thin films, produced by various ligands containing either oxygen or nitrogen atoms. In particular, the 2D-ACAR measurements on thin films of colloidal PbSe QDs capped with oleic acid ligands yield an increased intensity in the electron momentum density (EMD) at high momenta compared to PbSe quantum dots capped with oleylamine. Moreover, the EMD of PbSe QDs is strongly affected by the small ethylediamine ligands, since these molecules lead to small distances between QDs and favor neck formation between near neighbor QDs, inducing electronic coupling between neighboring QDs. The high sensitivity to the presence of oxygen atoms at the surface can be also exploited to monitor the surface oxidation of PbSe QDs upon exposure to air. Our study clearly demonstrates positron annihilation spectroscopy applied to thin films can exquisitely probe surface transformations of colloidal semiconductor QDs embedded in functional layers.

This chapter is based on the published paper:

W. Shi, S. W. H. Eijt, C. S. S. Sandeep, L. D. A. Siebbeles, A. J. Houtepen, S. Kinge, E. Brück, B. Barbiellini, and A. Bansil, Ligand-surface interactions and surface oxidation of colloidal PbSe quantum dots revealed by thin-film positron annihilation methods, Applied Physics Letters **108**, 081602 (2016)

4.1. Introduction

Semiconductor quantum dots (QDs) present remarkable advantages as photovoltaic materials due to their tunable electronic structure. Physical properties of QDs such as photoluminescence (PL), charge carrier mobility, and multiple-exciton generation are greatly influenced by ligands used in the passivation of surfaces. The local environment of atoms on QD surfaces is intrinsically different from that of the core of QDs and varies with the type of ligand. The structural and electronic modifications due to surface ligands have been investigated via ab-initio modelling studies.[1-4] Experimental techniques such as X-ray absorption spectroscopy (XAS)[5] have been used to explore changes in electronic properties due to the nature of ligands. This is important since key properties such as photoconductivity and charge carrier mobility depend strongly on the type of ligand attached to the surface of the PbSe QDs.[6] Treating PbSe QD films with short ligand molecules such as ethylenediamine (EDA) leads to strong electronic coupling between the PbSe cores and results in high carrier mobility and photoconductivity.[6] A key issue in the development of solar cells based on PbSe QD absorber layers[7,8] is that these cells often show a strong, time-dependent degradation under ambient conditions.[9-11] Optical Absorption Spectroscopy (OAS) and X-ray Photoemission Spectroscopy (XPS) studies of PbSe QD films indicate that the dominant degradation process involves oxidation of the QDs through exposure to atmospheric oxygen. Strategies based on surface engineering, e.g involving the reaction of molecular chlorine with Se to form a protective thin $PbCl_x$ shell, are being developed to arrive at air-stable PbSe QD solids for applications as solar cells and field effect transistors.[12,13] Clearly, the development of methods to investigate and monitor surfaces of PbSe QDs embedded in a sub-surface layer in such devices is of crucial importance. In this regard, positron annihilation spectroscopy (PAS) offers unique advantages over XAS, OAS and XPS, since it combines a high sensitivity to selectively probe surfaces of nanoparticles[14-16] with an established capacity for depth-profiling of films in the range of ~10 nm to a few μm.[17-19] These unique merits are highly important in studies of photovoltaic devices, where charge carrier separation requires the formation of a p-n junction,[8] and PAS can probe the involved light absorbing and charge separation layers independently.

4.2. Experimental

PbSe QDs with average sizes ranging between 5 nm and 6 nm were synthesized by using oleylamine-based synthesis.[26] PbSe QDs with OA ligands and PbSe QDs treated with EDA were made by exchanging oleylamine with the other ligands. Hexane was used as a solvent for drop casting PbSe QDs with OA ligands and OLA ligands onto indium-tinoxide coated glass substrates. The deposition of the PbSe QDs treated with EDA was performed by dip coating. The PbSe QD films were examined by 2D-ACAR using the thin-film POSH-ACAR setup at the Reactor Institute Delft.[14-16] For comparison, a PbSe single crystal was studied by 2D-ACAR using a ^{22}Na positron source. The 2D-ACAR distributions were obtained with positron implantation energies of 1 keV for PbSe QDs with EDA and 3.4 keV for PbSe QDs with OLA and OA ligands. These energies correspond to average implantation depths of ~7 nm and ~50

nm, respectively, coinciding to the middle of the deposited films as determined by positron Doppler broadening depth profiling.[22] The 2D-ACAR spectra consisting of 10^7 counts were analysed using the ACAR2D program.[27] The distributions were isotropic due to the polycrystalline random orientation of the nanocrystals. Therefore, 1D-ACAR spectra were obtained by integrating the isotropic part of the 2D-ACAR spectra over one momentum direction.

4.3. Results and Discussion

Here, we use the positron 2D-ACAR technique[14] to probe the electronic and compositional changes at the surfaces of PbSe QDs deposited as thin films. Previous positron lifetime experiments have shown that more than 90% of positrons implanted in a layer of PbSe QDs capped with Oleic Acid (OA) ligands trap at the surface of PbSe QDs,[16] where the positron is bound in a potential well behaving like an image potential at large distances (Figure 4.1). [20,21] Positrons implanted in the PbSe QD layer primarily lose their high initial kinetic energy in the PbSe cores of the QDs where they thermalize. Subsequently, they have a high probability of trapping in a surface state (Figure 4.1).[20,21] Therefore, the gamma rays produced by the annihilation of positrons trapped in surface states yields a way to probe the surface of PbSe QDs using 2D-ACAR, as the angular correlation of this annihilation radiation carries detailed information on the electron momentum density (EMD) sampled by the positron trapped in the surface state.[14]

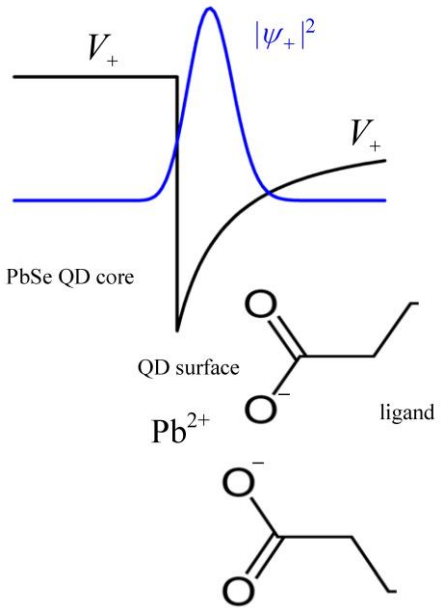

Figure 4.1. Schematic density $|\psi_+|^2$ of the positron surface state of the quantum dot, and schematic illustration of a $Pb^{2+}(OA^-)_2$ complex at the surface.

Films with PbSe QDs using three different ligands, namely, Oleylamine (OLA), OA and EDA,[22] were studied in order to investigate the variation in electron-positron momentum density with the type of ligand end group (amine or carboxyl) and chain length (long or short). The two ligands OA and OLA are equally long, but differ in their attachment to the PbSe QDs. OA ligands attach to the surfaces of PbSe QDs by the formation of $Pb^{2+}(OA^{-})_2$ complexes involving electrostatic interactions between lead and oxygen ions,[23,4,9] while the amine group of OLA only binds weakly to the surface of PbSe QDs, involving weak covalent interactions. Further, part of the QD surfaces might be passivated by chloride ions present in the synthesis.[24,25] EDA ligands are much shorter, and also interact only weakly to the surface of PbSe QDs. EDA treatment of PbSe QD films with OLA ligands mostly induces removal of the original ligands,[6] as was observed for films of PbSe QDs with OA ligands, while very little EDA was found on the surface after the treatment.[23] Our ACAR measurements on PbSe QD films with OA ligands reveal a stronger electron momentum density at high momenta compared to PbSe QDs with OLA ligands or treated with EDA. This effect is caused by oxygen atoms at the surface of QDs with OA ligands. This high sensitivity to oxygen atoms was further exploited to monitor the oxidation process of a layer of PbSe QDs with EDA ligands upon exposure to air.

Figure 4.2 presents the measured 1D-ACAR momentum distributions of PbSe QDs with OLA and OA ligands, and after EDA treatment of PbSe QDs with OLA ligands, in the form of ratio curves relative to bulk crystalline PbSe. The ratio curves show a peak at ~1 a.u. caused mostly by quantum confinement of the Se(4p) valence electron orbitals,[16] positron confinement[28,29] and other small contributions of atoms at the surface connected with the ligands.[16] The confinement of valence electrons and positrons for PbSe QDs capped with OA and OLA ligands leads to a small difference in the 1 a.u. peak area,[16,30] since the QDs have comparable sizes and the ligands have the same large chain length. In the case of EDA treated films, however, the confinement peak is significantly smaller. This pronounced difference can be attributed to the small QD-QD distances, which leads to electronic coupling of neighbouring QDs[6], resulting in a corresponding reduction of the Se(4p) valence electron confinement.[15] Furthermore, in ligand-exchange studies, it was demonstrated that short-chain diamines effectively strip lead oleate from (100) surfaces of the PbSe QDs.[23,31] The ligand replacement remains incomplete, particularly for the PbSe {100}-facets, which remain partially bare.[23] This leads to neck formation and epitaxially connection between PbSe QDs,[23] inducing electronic coupling between QDs. Partial depletion of QD surfaces and neck formation between QDs also occurs for EDA treatment of PbSe QDs capped with OLA ligands.[6] The electronic coupling induced by short QD-QD distances and neck formation results in more delocalized electron states with lower kinetic energy and momentum. This effect explains the narrowing of the EMD in momentum space, and a lower intensity of the confinement peak (Figure 4.2).

Independently, the high momentum region between 2 and 2.5 a.u. can be considered since the intensity here is primarily determined by the contributions of Pb atoms [Pb(5d) semi-core electrons][16] and contributions of ligand ad-atoms present at the surface. This region may also be influenced by positron annihilation with Se(3d) semi-core electrons.[16] The differences in the

ratio curves in this momentum range reflect the various surface compositions probed by the trapped positrons. Previous calculations showed that the contribution of O(1s) electrons gradually becomes the most important factor in the observed electron-positron momentum density in the region p>2 a.u. for PbSe QDs with OA ligands.[16] Figure 4.2 shows that PbSe QDs with OA ligands exhibit a higher intensity in this momentum range than PbSe QDs with OLA ligands or PbSe QDs treated with EDA. OA and OLA share the same large $C_{17}H_{33}$ tail, and differ only in the –(C=O)O– and –(CH_2)HN– end groups attached strongly and weakly, respectively, to the surface of the PbSe QDs. The EMD of PbSe QDs observed by positron annihilation is thus clearly affected by the surface composition (involving the presence of oxygen versus nitrogen, and possibly chlorine), as is visible in the high momentum range. Indeed, calculations indicate that oxygen and chloride ions form attractive sites for positrons, as O^- and Cl^- form bound states with a positron, in contrast to the case of nitrogen.[32-34] One should note that, for a positron localized at the surface of the QD, the dominant Coulomb attraction comes mostly from an individual ion and the contribution from all other ions can be neglected as a first approximation as in the Boev-Arefiev model considered in Ref. [35].

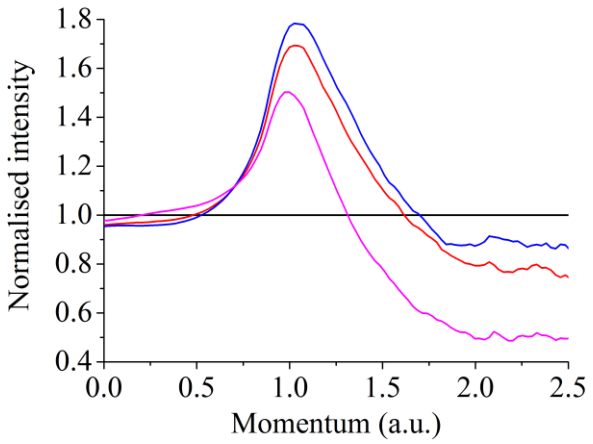

Figure 4.2. The ratio curve of 1D-ACAR momentum distributions for PbSe QDs with various surface compositions: oleic acid (blue); oleylamine (red); and, EDA (magenta). All curves are normalized to the directionally averaged 1D-ACAR distribution of bulk PbSe. (a.u. = atomic units).

Compared to the case of OLA ligands, PbSe QDs treated with EDA show a further reduced intensity in the high-momentum range, which could be attributed to annihilation at partially bare PbSe facets created during treatment with EDA.[23] Indeed, our previous study on PbSe QDs capped with OA ligands revealed a similar reduction in intensity for PbSe QDs with incompletely covered surfaces.[16] Confinement of valence electron orbitals with/without coupling between neighbouring QDs mainly influences the EMD at low momenta (Figure 4.2). This sensitivity demonstrates that thin film positron methods is a suitable characterization method to examine the surface composition and electronic structure of PbSe QD layers, which are key to understanding the resulting (opto-)electronic properties. Moreover, access to the depth range of up to ~1.5 μm below the outer surface of a PbSe QD layer in positron beam

experiments enables one to perform full depth-profiling studies of innovative photovoltaic devices based on PbSe QD layers[13] as the involved layer thicknesses typically range from several hundred nanometers to micrometers.

In the second set of experiments, the sensitivity to detect oxygen present at the surface of PbSe QDs is further exploited. The local oxidation of the surfaces of PbSe QDs treated with EDA ligands can therefore be investigated. A rather thin PbSe QD film of about 2-3 monolayers deposited on a ~100 nm ITO layer on a glass substrate was used,[22] in order to prevent any depth dependence of the oxidation process as all PbSe QDs are uniformly exposed to oxygen of ambient air. Figure 4.3a shows that the first absorbance peak in the OAS spectra shifts towards shorter wavelength over a period of 3 months of oxidation under ambient conditions. The observed large blue shift of the absorption features points to a reduction in the effective PbSe core diameter from an initial value of 6.1 nm to 5.0 nm[11] caused by the formation of a thin oxidized shell. Figure 4.3b explicitly shows the gradual reduction of the effective PbSe core radius of the QDs as a function of exposure time in air, extracted from the wavelength of the first absorption peak.[36] The decrease of the effective radius of PbSe QD cores by 0.3 to 0.5 nm over a period of 1 to 2 months as revealed by the OAS spectra is close to what was observed in previous studies on ~6 nm diameter PbSe QDs stored in solution under ambient conditions and application of vigorous stirring.[11]

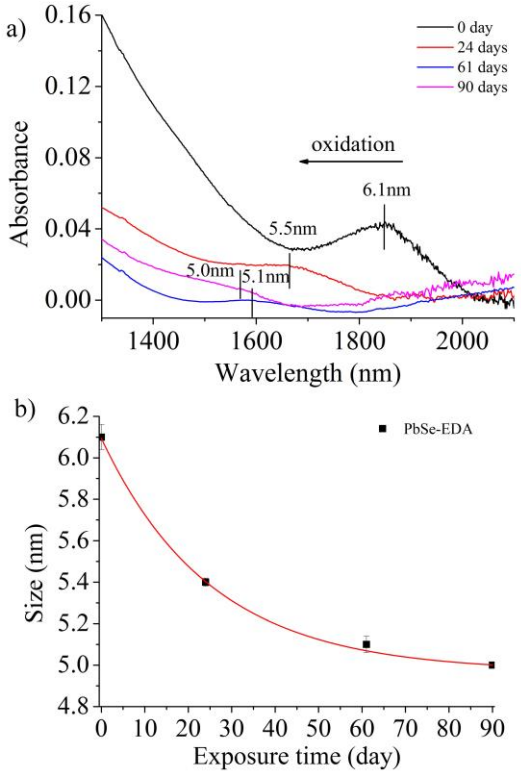

Figure 4.3. a) Evolution of absorption spectra of a PbSe QD film treated with EDA upon exposure to air at room temperature; b) Evolution of the effective PbSe core size of the QDs. Solid line serves as a guide-to-the-eye.

Figure 4.4a shows the corresponding evolution of 1D-ACAR ratio curves of PbSe QDs treated with EDA, for different periods of air exposure. The oxidation of PbSe QDs after 24 days leads to an increase of the confinement peak near 1 a.u. due to the decrease in effective size of the core PbSe QDs by the oxidation, which enhances the confinement of the Se(4p) valence electrons and also reduces the electronic coupling between QDs. Interestingly, the increased fraction of oxygen atoms present at the surfaces of PbSe QDs by surface oxidation yields a pronounced increase in intensity for $p > 2$ a.u. due to the contribution of O(1s) electrons to the momentum density. Notably, the strongest increase in the momentum density in the range of 2-2.5 a.u. is seen already after the first period of exposure in air of 24 days (Figure 4.4), while the oxide shell continues to grow afterwards, as revealed by the continued shift towards shorter wavelengths of the OAS spectra (Figure 4.3). The normalised intensity in the momentum range of 2-2.5 a.u. (Figure 4.4b), in contrast, indicates a saturation in the high momentum intensity for the longer air exposure times of 61 and 90 days. This can be understood since the positron mostly probes the outermost atomic layers of the QD, *i.e*. the outer surface region of the oxidized shell, likely consisting of PbO, SeO_2 and $PbSeO_3$ formed at the surface of the QD.[10] Small differences in intensity at high momenta over 24-90 days can be caused by a variation in binding energy and distance of the positron from the surface, since the image potential will reduce in strength due to the more insulating character of the surface with the growth of an oxide layer.[37] The transformation of the surface by the oxidation process thus seems to saturate sooner than the continued growth of the oxidized shell below the surface, as monitored by the first absorption peak in the OAS which provides a sensitive measure of the size of the non-oxidized PbSe cores of the QDs. Decrease in the effective PbSe core size revealed by the OAS is consistent with the observed (small) increase in the confinement peak in the 1D-ACAR ratio curves, while the intensity of the ratio curves for $p > 2$ a.u. provides complementary information on the local oxygen fraction formed at the outer surface of the PbSe QDs during the oxidation process. These results demonstrate that positron methods can be sensitively applied to probe the oxidation at the surfaces of colloidal QDs, and indicate more generally that surface chemical transformations can be monitored. A more quantitative determination of the surface chemical composition requires details of shape of the positron wave function at the surface of the QD and its overlap with the (local) electronic orbitals, and the development of appropriate ab-initio methods for this purpose is needed.

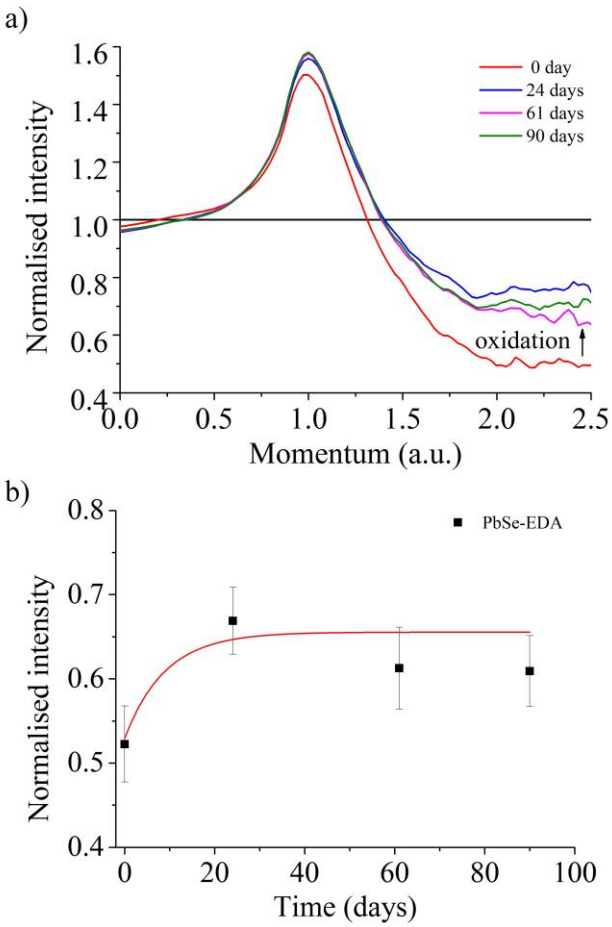

Figure 4.4. a) Evolution of 1D-ACAR momentum distribution for PbSe QDs treated with EDA with exposure time in air, presented as ratio curves relative to the directionally averaged 1D-ACAR distribution of bulk PbSe; b) Normalized intensity ratio to bulk PbSe at the momentum region between 2 a.u. and 2.5 a.u. Solid line is a guide-to-the-eye.

4.4. Conclusions

In summary, our study demonstrates that positrons are effective in probing the composition of the surfaces of reduced dimensional systems such as the PbSe QDs. By enabling this advanced characterization of the attachment of ligand molecules, our method can now facilitate the optimization of efficient charge carrier transport in novel optoelectronic devices by introducing descriptors based on positron annihilation characteristics. Our study further demonstrates that positron methods[38] can be used to sensitively monitor oxidation processes at the surfaces of colloidal nanocrystals. Thin film positron methods thus hold promise as a surface characterization technique for colloidal semiconductor QDs in functional layers used to develop (opto-)electronic devices including thin film solar cells, light-emitting diodes and field effect transistors. Positron techniques will provide key insights into chemical transformations at the surfaces of QDs and aid their development by surface chemical engineering strategies of innovative core-shell structures required for stabilization against oxidation under ambient

conditions. Finally, our study shows that the electron momentum density of PbSe QDs is strongly affected by electronic coupling between the neighbouring QDs induced by the use of small EDA molecules, related to short interparticle distances and induced neck formation between neighboring QDs. Such a coupling is very important to achieve favorable charge carrier mobility and enhanced photoconductivity of PbSe QD layers for prospective application in next generation photovoltaic devices. The depth-profiling capability of the applied positron method can provide a means to probe (potentially *in-situ*) the light absorbing and charge separation layers as well as the p-n junction interface region independently, which play a key role for radical improvement in solar cell efficiencies.

References

[1] A. Franceschetti, Phys. Rev. B **78**, 075418 (2008).

[2] V. Petkov, I. Moreels, Z. Hens, and Y. Ren, Phys. Rev. B **81**, 241304 (2010).

[3] D. Kim, D.-H. Kim, J.-H. Lee, J.C. Grossman, Phys. Rev. Lett. **110**, 196802 (2013).

[4] C.R. Bealing, W.J. Baumgardner, J.J. Choi, T. Hanrath, R.G. Hennig, ACS Nano **6**, 2118 (2012).

[5] J.R. Lee, D. Witley, R.W. Meulenberg, A. Wolcott, J.Z. Zhang, D. Prendergast, D.D. Lovingood, G.F. Strouse, T. Ogitsu, E. Schwegler, L.J. Terminello, T. van Buuren, Nano Lett. **12**, 2763 (2012).

[6] Y. Gao, M. Aerts, C.S.S. Sandeep, E. Talgorn, T.J. Savenije, S. Kinge, L.D.A. Siebbeles, A.J. Houtepen, ACS Nano **6**, 9606 (2012).

[7] X. Lan, S. Masala, E.H. Sargent, Nature Mater. **13**, 233 (2014).

[8] V. Renugopalakrishnan, B. Barbiellini, C. King, M. Molinari, K. Mochalov, A. Sukhanova, I. Nabiev, P. Fojan, H.L. Tuller, M. Chin, P. Somasundaran, E. Padrós, S. Ramakrishna, J. Phys. Chem. C **118**, 16710 (2014).

[9] I. Moreels, B. Fritzinger, J.C. Martins, Z. Hens, J. Am. Chem. Soc. **130**, 15081 (2008).

[10] M. Sykora, A.Y. Koposov, J.A McGuire, R.K. Schulze, O. Tretiak, J.M. Pietryga, V.I. Klimov, ACS Nano **4**, 2021 (2010).

[11] W.K. Bae, J. Joo, L.A. Padilha, J. Won, D.C. Lee, Q. Lin, W.K. Koh, H. Luo, V.I. Klimov, J.M. Pietryga, J. Am. Chem. Soc. **134**, 20160 (2012).

[12] M.H. Zarghami, Y. Liu, M. Gibbs, E. Gebremichael, C. Webster, M. Law, ACS Nano **4**, 2475 (2010).

[13] Z. Ning, O. Voznyy, J. Pan, S. Hoogland, V. Adinolfi, J. Xu, M. Li, A.R. Kirmani, J.-P. Sun, J. Minor, K.W. Kemp, H. Dong, L. Rollny, A. Labelle, G. Carey, B. Sutherland, I. Hill, A. Amassian, H. Liu, J. Tang, O.M. Bakr, E.H. Sargent, Nature Mater. **13**, 822 (2014).

[14] S.W.H. Eijt, A. van Veen, H. Schut, P.E. Mijnarends, A.B. Denison, B. Barbiellini, A. Bansil, Nature Mater. **5**, 23 (2006).

[15] S.W.H. Eijt, P. E. Mijnarends, L. C. van Schaarenburg, A. J. Houtepen, D. Vanmaekelbergh, B. Barbiellini, A. Bansil, Appl. Phys. Lett. **94**, 091908 (2009).

[16] L. Chai, W. Al-Sawai, Y. Gao, A. J. Houtepen, P. E. Mijnarends, B. Barbiellini, H. Schut, L. C. van Schaarenburg, M. A. van Huis, L. Ravelli, W. Egger, S. Kaprzyk, A. Bansil, S. W. H. Eijt, APL Mater. **1**, 022111 (2013).

[17] P.J. Schultz, and K.G. Lynn, Rev. Mod. Phys. **60**, 701 (1988).

[18] A. van Veen, H. Schut, and P. E. Mijnarends, *Depth-Profiling of Subsurface Regions, Interfaces and Thin Films*. in *Positron Beams and Their Applications*, edited by P. G. Coleman, (World Scientific, Singapore, 2000), pp 191 – 225.

[19] R. Krause-Rehberg and H. S. Leipner, *Positron Annihilation in Semiconductors: Defect studies* (Springer Verlag, Berlin, 1999).

[20] S. Mukherjee, M.P. Nadesalingam, P. Guagliardo, A.D. Sergeant, B. Barbiellini, J.F. Williams, N.G. Fazleev, and A.H. Weiss, Phys. Rev. Lett. **104**, 247403 (2010).

[21] J. Mayer, C. Hugenschmidt, and K. Schreckenbach, Phys. Rev. Lett. **105**, 207401 (2010).

[22] See supplemental material at section 4.5 for XRD and OAS spectra (Figure S4.5.1), particle sizes (Table S4.5.1), Doppler depth profiles and VEPFIT analysis (Figure S4.5.2, Tables S4.5.2 and S4.5.3), details of the positron 2D-ACAR experiments and further information on the ligand molecules.

[23] C.S.S. Sandeep, J.M. Azpiroz, W.H. Evers, S.C. Boehme, I. Moreels, S. Kinge, L.D.A. Siebbeles, I. Infante, A.J. Houtepen, ACS Nano **8**, 11499 (2014).
[24] I. Moreels, Y. Justo, B. de Geyter, K. Haustraete, J.C. Martins, Z. Hens, ACS Nano **5**, 2004 (2011).
[25] M.C. Weidman, M.E. Beck, R.S. Hoffman, F. Prins, W.A. Tisdale, ACS Nano **8**, 6363 (2014).
[26] M.V. Kovalenko, D.V. Talapin, M.A. Loi, F. Cordella, G. Hesser, M.I. Bodnarchuk, W. Heiss, Angew. Chem. Int. Ed. **47**, 3029 (2008).
[27] L. Chai, M.Sc. thesis, Delft University of Technology, Delft, 2010.
[28] A. Calloni, A. Dupasquier, R. Ferragut, P. Folegati, M.M. Iglesias, I. Makkonen, M.J. Puska, Phys. Rev. B **72**, 054112 (2005).
[29] Z. Tang, T. Toyama, Y. Nagai, K Inoue, Z.Q. Zhu, M. Hasegawa, J. Phys. Cond. Matt. **20**, 445203 (2008).
[30] M.H. Weber, K.G. Lynn, B. Barbiellini, P.A. Sterne, A.B. Denison, Phys. Rev. B **66**, 041305 (2002).
[31] N.C. Anderson, M.P. Hendricks, J.J. Choi, J.S. Owen, J. Am. Chem. Soc. **135**, 18536 (2013).
[32] X. Cheng, D. Babikov, D.M. Schrader, Phys. Rev. A **85**, 012503 (2012).
[33] J.A. Ludlow, G.F. Gribakin, Int. Rev. Atom. Mol. Phys. **1**, 73 (2010).
[34] D.M. Schrader, T. Yoshida, K. Iguchi, Phys. Rev. Lett. **68**, 3281 (1992)..
[35] A. Harju, B. Barbiellini, R.M. Nieminen, Phys. Rev. A **54**, 4849 (1996).
[36] Q. Dai, Y. Wang, X. Li, Y. Zhang, D.J. Pellegrino, M. Zhao, B. Zou, J.-T. Seo, Y. Wang, W.W. Yu, ACS Nano **3**, 1518 (2009).
[37] A.P. Mills, Jr., L. Pfeiffer, Phys. Rev. B **32**, 53 (1985).
[38] It should be noted that, owing to the isotropic nature of the momentum density of the QD samples, the positron Coincidence Doppler Broadening (CBD) method is expected to give similar results as the 2D-ACAR method, albeit at a lower momentum resolution. In fact, CDB data on CdSe QDs by Weber *et al.*[30] are consistent with our ACAR study on CdSe QDs.[14]

4.5 Supplemental Material

XRD and OAS spectra of PbSe QD films

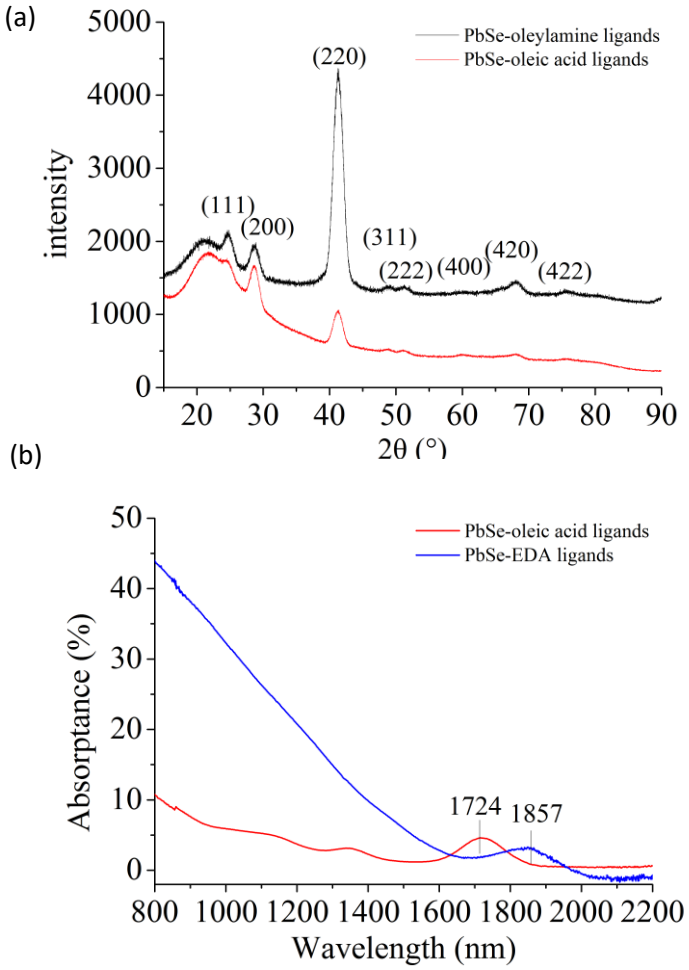

Figure S4.5.1. (a) XRD spectra of PbSe QDs with oleylamine ligands and oleic acid ligands, (b) OAS spectra of PbSe QDs with oleic acid ligands and EDA ligands.

Table S4.5.1. sizes of PbSe QDs extracted from XRD and OAS

sample	Average size(nm)	
	XRD	OAS
PbSe-oleic acid ligands	6.4	5.6
PbSe-oleylamine ligands	6.1	-
PbSe-EDA ligands	-	6.1

In Figure S4.5.1, XRD spectra and OAS spectra are presented, which were used to estimate the average sizes of PbSe QDs, as listed in Table S4.5.1. The average as-deposited crystal size of

the oleic acid-capped and oleylamine-capped PbSe QDs estimated from the peak broadening of XRD spectra is 6.4 nm and 6.1 nm, respectively. From the first exciton absorption peak, the extracted sizes of the PbSe QDs with oleic acid ligands and EDA ligands are 5.6 nm and 6.1 nm. The XRD patterns show that the PbSe QDs are in the rock salt phase.

Doppler depth profiles of PbSe QD film with EDA ligands used in the oxidation study

A thickness of the PbSe QD film with EDA ligands of about 15 nm (2-3 monolayers of PbSe QDs) was extracted from VEPFIT analysis of the positron Doppler broadening depth profiles shown in Figure S4.5.2. The fitted parameters are listed in Table S4.5.2 and S4.5.3.

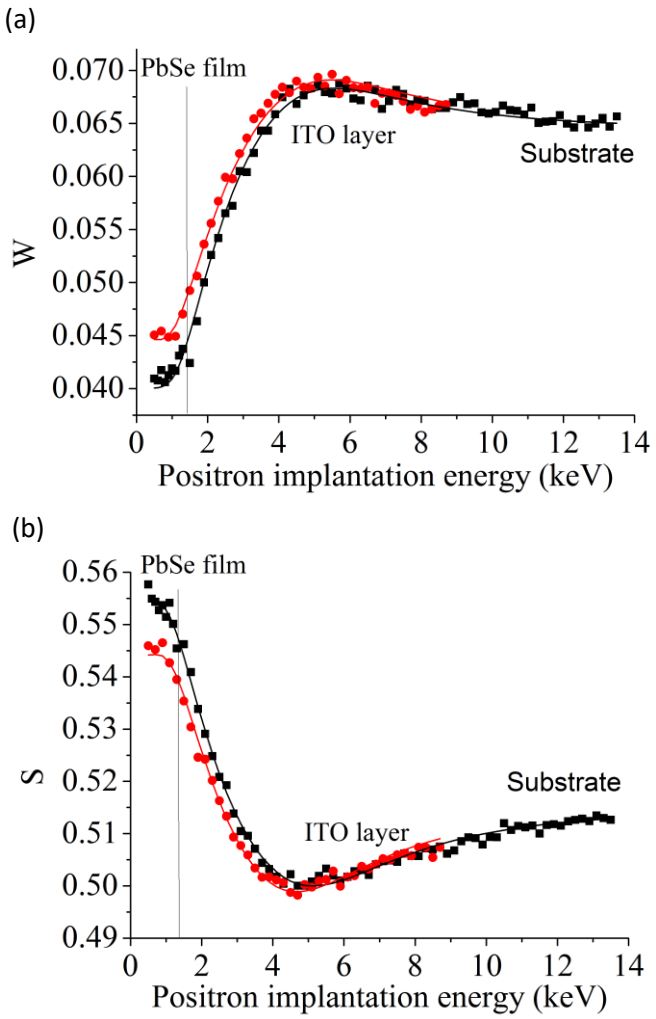

Figure S4.5.2. Positron Doppler broadening S-parameter (W-parameter) depth profiles of PbSe QD layer on an ITO-coated glass substrate before (black squares) and after oxidation (red circles).

Table S4.5.1. VEPFIT analysis results for EDA-capped PbSe QD film

layer	Density (g/cm^3)	Diffusion length (nm)	Layer width (nm)	S parameter	W parameter
PbSe layer	5.67*	5	15	0.5558 (0.0005)	0.039 (0.001)
ITO	7.1*	16*	109	0.4902 (0.0003)	0.073 (0.001)
glass	2.53*	29*	-	0.5149 (0.0003)	0.064 (0.001)

Table S4.5.2. VEPFIT analysis results for oxidized EDA-capped PbSe QD film

layer	Density (g/cm^3)	Diffusion length (nm)	Layer width (nm)	S parameter	W parameter
PbSe layer	5.67*	1	12	0.5443 (0.0004)	0.045 (0.001)
ITO	7.1*	16*	93	0.4871 (0.0004)	0.074 (0.001)
glass	2.53*	29*	-	0.5149 (0.0003)	0.064 (0.001)

* fixed

Ligand capping molecules

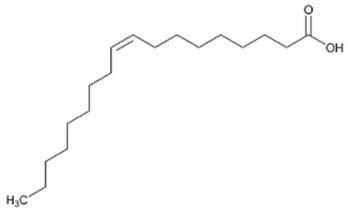

(a) Oleic acid (OA)

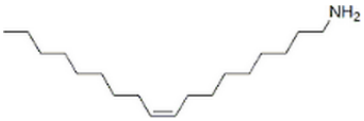

(b) Oleylamine (OLA)

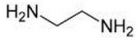

(c) Ethylenediamine (EDA)

Ligand type	Ligand name	Molecular structure	Interparticle space	Bond between ligand and QD
Long-chain molecules	Oleylamine, Oleic acid	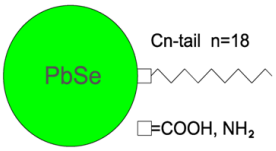	>1.5nm	O-Pb N-Pb
Short-chain molecules	EDA	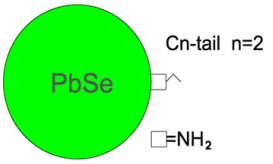	0.6nm	N-Pb

Oxidation process

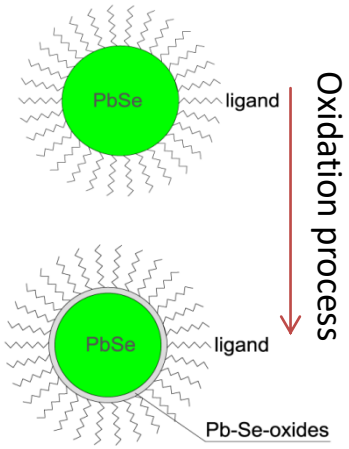

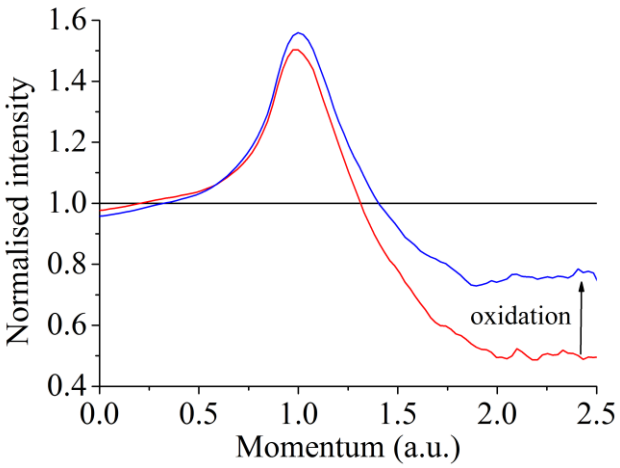

* All the figures are made by origin 8.5.1 program.

Chapter 5

Study of ligand-surface interactions of CdSe Quantum Dots using thin-film positron annihilation methods

Abstract

Positron studies have shown that positron annihilation techniques are surface-sensitive probes of the electronic structure of CdSe QDs and PbSe QDs and their surface composition. The variation of the electronic structure and surface composition induced by various ligands attached to the QDs is in general still unclear. In this study, Doppler Broadening of Positron Annihilation Radiation (DBAR) and two-dimensional Angular Correlation of Annihilation radiation (2D-ACAR) were used to probe thin films of CdSe QDs with stearic acid (SA) ligands and trioctylphosphine oxide (TOPO), oleylamine (OLA), and oleic acid (OA) ligands obtained from the ligand exchange with SA ligands. The majority of positrons are strongly trapped at the surface of CdSe QDs and can distinguish O and N atoms of ligands bound to Cd atoms at the surface. However, the positron shows a smaller discriminative power in probing the surface composition of CdSe QDs than for the case of PbSe QDs. This could be attributed to the different surface structure of CdSe QDs and PbSe QDs. CdSe QDs are terminated by a shell of Se atoms due to surface relaxation of puckering-out Se and pulled-in Cd atoms, while PbSe QDs tend to be enclosed by a layer of excess Pb atoms. Besides, a difference in the positron surface state for CdSe and PbSe QDs could also contribute to the observed difference.

5.1. Introduction

Semiconductor colloidal quantum dots (QDs) present remarkable advantages as photovoltaic materials due to their tunable optoelectronic and optical properties. QD-based thin film solar cells have gained a large progress in the past few years by developing more efficient synthesis techniques, optimizing device structures,[1] and improving charge transport. Currently, the efficiency record has exceeded 10% for PbS QD-based solar cells.[2,3] With the smaller size, the surface plays an increasingly dominant role in controlling physical properties such as charge carrier mobility and multiple-exciton generation which are important for development of QD solar cells. On the other hand, the effect of the defect states in the band gap introduced by dangling bonds of under-coordinated surface atoms is also magnified due to the larger surface-to-volume ratio, and can deteriorate greatly the efficiency of solar cells. Surface ligand molecules play an important role in passivating such surface states. In some cases, these ligands require to be exchanged by other surface-binding species in order to improve their end functionality, e.g., in order to promote the electrical conductivity of QD layers. The passivation of the surface sites of QDs, which is normally determined by the ligand density, can effectively remove the mid-gap states in the electronic structure.[4]

Experimental studies have shown that the positron is a highly surface-sensitive probe of the electronic structure of colloidal CdSe QDs and PbSe QDs, and of the chemical composition at their surfaces.[5-7] Besides, our recent positron lifetime experiments parallel to first-principles calculations within the WDA scheme[8] provided evidence for the existence of a positron surface state in CdSe QDs.[9] Positron studies on CdSe QDs[5] and PbSe QDs[6] with various sizes were performed previously. For the case of CdSe QDs, these studies revealed the presence of a selenium-rich surface due to the outward surface relaxation of Se atoms [5], while for PbSe QDs a total different surface structure occurs with excess Pb atoms that are positioned on top of the PbSe surface, and the positrons sensitively probe the local O atoms of oleate ligands attached to Pb ad-atoms at the surface[6]. Further positron studies[7] on the PbSe QDs tethered with various ligands were performed, showing that the positron can effectively distinguish the N atoms of oleylamine (OLA) ligands and O atoms of oleic acid (OA) ligands attached at the surface. Furthermore, positron annihilation can effectively monitor the oxidation process when exposing PbSe QDs to air.[7] However, the modification of the surface composition and the electronic structure of CdSe QDs caused by the surface interaction with different ligands has not yet been studied. Besides, differences in the sensitivity of positron annihilation to the presence of atoms involved in the ligand binding at the surface for CdSe QDs and PbSe QDs needs to be examined.

In this Chapter, we show the sensitivity of the two-dimensional Angular Correlation of Annihilation radiation (2D-ACAR) method in probing the variation of the surface composition induced by various ligands (TOPO, OA, OLA, and SA) obtained through the ligand exchange. The majority of positrons are strongly trapped at the surface of CdSe QDs and can distinguish O atoms and N atoms of ligands binding at the surface of CdSe QDs. When comparing with PbSe

QDs, the positron shows a smaller discriminative power in probing the surface composition of CdSe QDs.

5.2. Experimental

CdSe QDs with a mean diameter of 4 nm and 6.5 nm were produced at the Laboratory for Surface Science and Technology of the University of Maine using the synthesis methods described in Ref. [10], which produces QDs nominally capped with both stearic acid (SA) and trioctylphosphine oxide (TOPO) ligands. In Ref. [10], it was shown that the type of ligand present on the surface of the QD can be controlled during post-processing, so that only SA is left on the surface. Using such washed CdSe QDs capped with SA, ligand exchange was then performed with three ligand types: oleylamine (OLA), oleic acid (OA), and TOPO. In this way, eight unique samples were obtained: CdSe QDs of sizes 4 and 6.5 nm, respectively, and coated with SA, TOPO, OLA, and OA. CdSe QD layers with thicknesses in the range of several μm were produced by drop-casting of the five different solutions on 1.5×1.5 cm^2 FTO-coated glass substrates.

Doppler Broadening of Positron Annihilation Radiation (DBAR) measurements were performed at room temperature using the variable mono-energetic positron beam VEP setup at the Reactor Institute Delft. Samples were mounted onto the sample holder by two thin metal strings. Measurements were performed using positron energies varying from 0 keV to 25 keV. The intensity of the low-energy positron beam at sample position is around 10^4 e^+/s, and the FWHM size of the beam is 8 mm in diameter. A high purity Ge solid-state detector with an energy resolution of 1.8 keV was used to determine the energy of the emitted annihilation γ-rays. S and W parameters were extracted from the measured Doppler broadened annihilation γ-ray photo-peak, defined as the fraction of counts in the central region and in the wing regions of the 511 keV annihilation photo-peak, respectively.

The drop-cast nanocrystal films were further examined using two-dimensional Angular Correlation of Annihilation Radiation (2D-ACAR) on the thin-film POSH-ACAR setup at the Reactor Institute Delft. For comparison, a CdSe single crystal was studied by 2D-ACAR using a ^{22}Na positron source. The thickness of the QD-film and positron implantation energy applied in 2D-ACAR measurement were examined by depth profile measurement at the POSH setup using a Ge detector before each 2D-ACAR measurement. The 2D-ACAR distributions were obtained at a positron implantation energy of 6.2 keV for the CdSe QD films. The momentum resolution was 1.4×1.4 $(10^{-3} m_0 c)^2$, where m_0 is the electron rest mass and c the velocity of light. The 2D-ACAR spectra consisting of about 10^7 annihilation events were analyzed using the ACAR-2D program.[6] 1D-ACAR spectra were obtained by integrating the 2D-ACAR spectra over one momentum direction.

5.3. Results and discussion

Figure 5.1 shows the S parameter as a function of the positron implantation energy for 4-nm CdSe QDs capped with OA, OLA, TOPO, and SA ligands examined by DBAR experiments. In the whole range of the S-E curves, the S parameter for all the films is well above the S value from the FTO coated substrate (S_{FTO} = 0.4761 for the FTO film and S_{glass} = 0.5409 for the glass, as determined using a bare FTO-coated glass substrate), which means that the positron can hardly reach the substrate for all the applied positron implantation energies up to 25 keV, indicating a layer thickness of the CdSe QD films beyond 2 μm. The small variation of the S parameter for the whole range of the positron implantation energies reveals that all the films are quite uniform, except that two distinctive layers for the case of OLA ligands are shown to be present. The solid lines through the data points was fitted by the VEPFIT program[11] with three layers: 2 layers for CdSe QDs, and further the FTO coated glass substrate. As shown in figure 5.1, CdSe QDs with OA, TOPO, and SA ligands show the similar S parameters, while CdSe QDs with OLA show a slightly higher S parameter below 12 keV. The difference in S parameters for CdSe QDs capped with OLA ligands and the rest is within ~1%, which is small when compared to the reduction (4.2%) in S parameter of CdSe QDs with size decreasing from 4.4 nm to 2.5 nm[5]. This small difference is probably attributable to the slightly larger fraction of pick-off ortho-positronium (o-Ps) and p-Ps formed in the open space available at the QD surface and between the carbon chains of the OLA ligands capped at the surface of CdSe QDs, as is revealed in PALS studies[9].

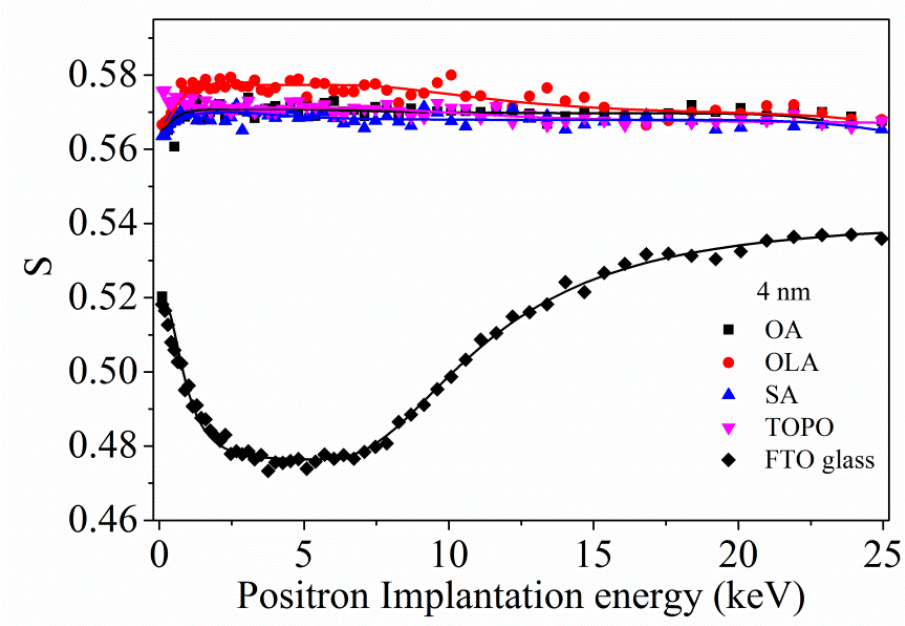

Figure 5.1. S parameter as a function of the positron implantation energy for 4 nm CdSe QDs with OLA, OA, TOPO, and SA ligands

Figure 5.2 presents the measured 1D-ACAR positron-electron momentum distributions (PEMD) of 4 nm and 6.5 nm CdSe QDs with OA, OLA, TOPO, and SA ligands collected at a positron implantation energy of 6.2 keV, in the form of ratio curves relative to bulk crystalline CdSe. The ratio curves for both 4 nm and 6.5 nm CdSe QDs show a peak at about 1 atomic momentum units (a.u.), which agrees well with results in reference[12] and is often observed for positron probing in nanocrystals, characteristic for the quantum confinement of Se(4p) and Cd(5s) valence electrons.[5,6,13] 4-nm CdSe QDs show a higher peak than 6.5 nm CdSe mainly due to stronger quantum confinement of the Se(4p) valence electrons. This can qualitatively be explained by the uncertainty principle, in which the smaller size of the QDs leads to more spatial confinement of the valence electrons, and thus, more broadening of the momentum distribution. CdSe QDs with all of the ligands show the similar intensity at 0 a.u., except for CdSe QDs with OLA ligands, which shows much higher intensity at momentum region of around 0 a.u.. The intensity decreases in the momentum region between 0 a.u. and 0.5 a.u.. CdSe QDs with both sizes (4 nm and 6.5 nm) shows similar features. The high intensity of the ratio curve in the low momentum region for CdSe QDs capped with OLA ligands is in agreement with the higher S parameter in figure 5.1. This is consistent with a larger fraction of pick-off o-Ps and p-Ps, which is probably due to the relatively low density of OLA ligands bound at the surface of CdSe QDs.

In the higher momentum region between 2.0 a.u. and 2.5 a.u., the intensity varies with the type of ligand capping the CdSe QDs. The high momentum region for CdSe mainly comes from annihilation with inner atomic shell electrons (Cd(4d)[5]), which allows one to understand the chemical composition which is at surface of CdSe QDs. CdSe QDs with OA ligands and SA ligands show the similar intensity, which can be explained since OA and SA ligands possess the same anchor group –(C=O)O– and a large $C_{17}H_{33}$ or $C_{17}H_{35}$ tail, with the same O atoms attached at surface. This leads to a similar binding strength between the attached atoms of ligands and Cd atoms at surface and also a very similar local surface structure of CdSe QDs. In comparison, CdSe QDs capped with TOPO show the highest intensity, while CdSe QDs with OLA shows the lowest intensity in the high momentum range. TOPO and OLA have different anchor groups consisting of $–(CH_2)_3P=O$ and $–(CH_2)H_2N$, respectively, with quite different attachment of the O and N atoms to Cd atoms at the surface of CdSe QDs. The observed order of the intensities for different ligands is similar to the case for PbSe QDs[7], in which the local atomic environment involving N atoms of the OLA ligands give a lower intensity than for the case of O atoms of the OA ligands. This could be due to the fact that oxygen and chloride ions (O^- and Cl^-) are more attractive sites for positrons than nitrogen when they form bound states with positrons.[7] This variation of the intensities in the high momentum region reveals the positron's sensitivity of probing the surface composition of CdSe QDs.

(a)

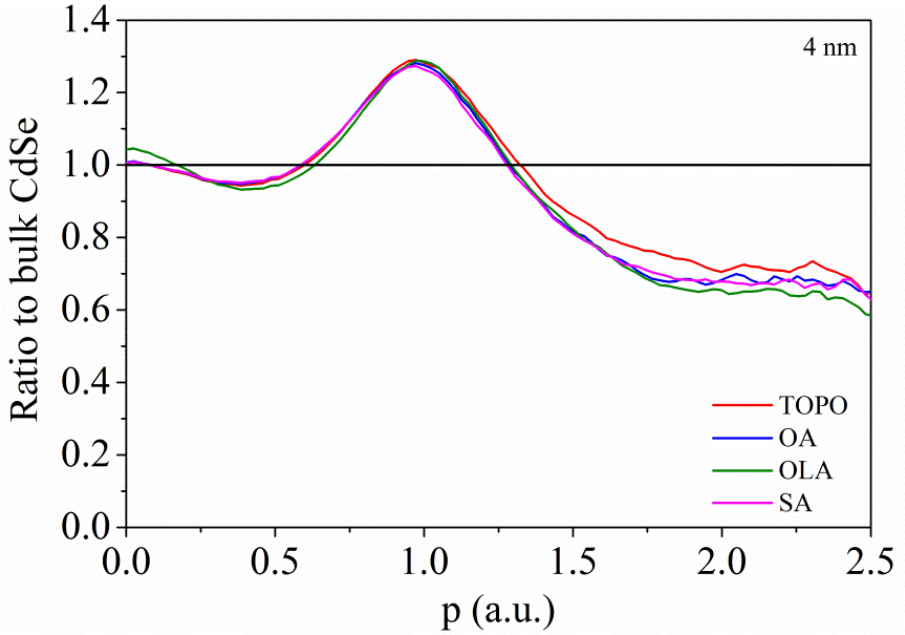

(b)

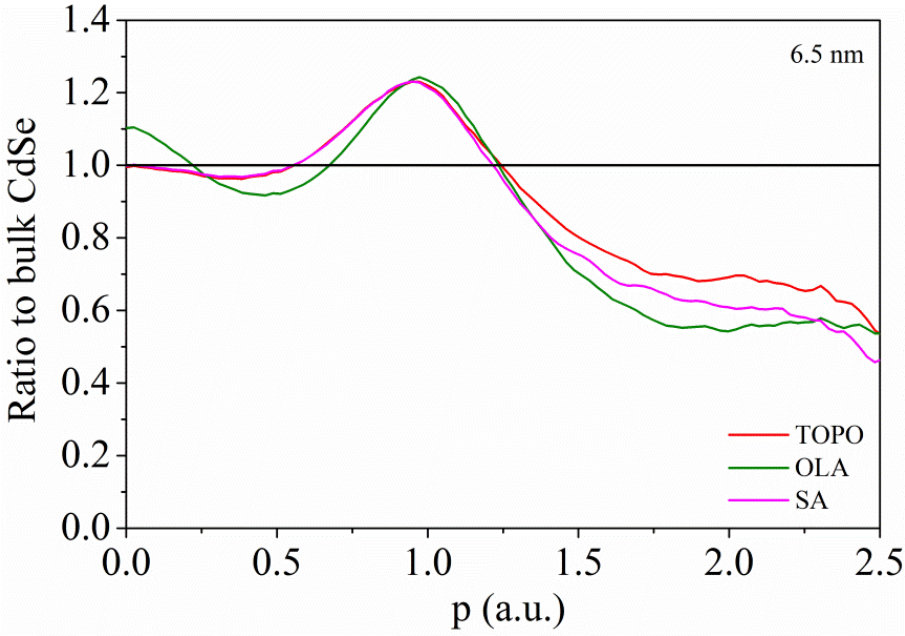

Figure 5.2. (a) and (b) The ratio curves of 1D-ACAR momentum distributions for CdSe QDs with various ligands. All curves are normalized to the directionally averaged 1D-ACAR distribution of bulk CdSe. (a.u. = atomic units).

In order to explore the different behaviour of CdSe QDs and PbSe QDs as seen by positron annihilation, we compared ratio curves of the PEMDs of CdSe QDs and PbSe QDs. Compared with the ratio curves of the PEMDs of PbSe QDs with a size between 5 nm and 6 nm, we can

observe that the intensity of the quantum confinement peak of the ratio curve (1.2-1.3) for CdSe QDs (6.5 nm) is significantly smaller than that for the PbSe QDs (1.5-1.8)[7] at around 1 a.u.. This indicates that electrons in the valence band in a 6.5-nm CdSe QD experience a weaker confinement than the valence electrons in a PbSe QD of similar size. This indicates that the wave functions of the Se(4p) valence electrons in PbSe QDs are more confined than in CdSe QDs. Also, it is a conceivable that the positron wave function for PbSe QDs is more confined, leading to additional broadening of the PEMDs of PbSe QDs.

Another notable observation is that the variation in PEMD intensities in the high momentum region from 2.0 a.u. to 2.5 a.u., as caused by the TOPO, OA, SA, and OLA ligands, is smaller for CdSe QDs than for PbSe QDs. First, the intensity for CdSe QDs in the momentum range from 2.0 a.u. to 2.5 a.u. is smaller than that for the bulk CdSe. The reduced intensity relative to that of the bulk by 30% - 40% reveals an increased probability of positron trapping near Se atoms and an increased annihilation probability with atoms of ligands at the surface of CdSe QDs. The corresponding reduction in intensity at high momentum is much less for the case of PbSe QDs (10% - 20%) [7]. This is probably due to a higher positron trapping probability at Se atoms at the QD surface for CdSe QDs than that for PbSe QDs, where annihilation takes place with both valence electrons of the excess Pb atoms and of the atoms of ligands connected at the surface sites. Indeed, previous studies showed that CdSe QDs are terminated by a shell of Se atoms[14] due to surface relaxation of the Se and Cd atoms, while PbSe QDs tend to be enclosed by a layer of excess Pb atoms[15]. The effects of the ligands on the intensity of the ratio curves at high momentum for CdSe QDs are therefore smaller than for PbSe QDs. For PbSe QDs, the intensity of the ratio curve at higher momentum region (2.0 a.u.–2.5 a.u.) increases from 0.8 to 0.9 when changing the capping ligands from OLA to OA, while for CdSe, the variation of the intensity in the ratio curve is twice smaller. Possibly, this can further be attributed to a difference in the positron surface state in CdSe and PbSe QDs. PbSe has Pb-Se bonds with a strong ionic character, while CdSe shows mainly covalent Cd-Se bonds. When capped with ligands with an anchor group of –(C=O)O–, the binding mode between oxygen atoms and the Pb and Cd metal atoms at the QD surface will thus be ionic and covalent, respectively. This could lead to that a significantly larger overlap of the positron wavefunction with O atoms than with Pb atoms for PbSe QDs, while for CdSe QDs the positron wave function tends to overlap with Cd, Se, and O atoms more equally. Thus, the positron is less sensitive to probe the presence of O atoms at the surface of CdSe QDs.

5.4. Conclusions

The 2D-ACAR method shows the sensitivity of positron annihilation in probing the modification of the surface composition of CdSe QDs induced by the variation in ligand capping (TOPO, OA, OLA, and SA) obtained through ligand exchange. The majority of the positrons are strongly trapped at the surface of CdSe QDs, annihilating with Cd atoms and Se atoms at the surface and the atoms (O or N) of ligands binding with the CdSe QDs. CdSe QDs with OA and SA ligands have similar intensity at the higher momentum region, since they

possess the same anchor group –(C=O)O– and a large $C_{17}H_{33}$ or $C_{17}H_{35}$ tail. CdSe QDs with TOPO, OA, and SA ligands show a higher intensity at the high momentum region than OLA ligands, because O(1s) core electrons of oxygen contribute to high momentum intensity. However, when comparing with PbSe QDs, the positron is less sensitive in probing the surface composition of CdSe QDs, as the observed change in the intensity of the momentum distribution of CdSe QDs at the high momentum region caused by the ligands is much smaller than that of PbSe QDs. This is attributed to the covalent nature of the bonds between O (or N) atoms and Cd atoms, leading to a similar probability of annihilation with electrons of O (or N) atoms and Se atoms, unlike the case of PbSe QDs, where the positron predominantly annihilates with electrons of O (or N) atoms that are attached to the excess Pb atoms forming a shell on PbSe QDs.

References

[1] C. R. Kagan, E. Lifshitz, E. H. Sargent, and D. V. Talapin, Science **353**, aac5523 (2016).

[2] A. Stavrinadis, S. Pradhan, P. Papagiorgis, G. Itskos, and G. Konstantatos, ACS Energy Letters **2**, 739 (2017).

[3] E. M. Sanehira, A. R. Marshall, J. A. Christians, S. P. Harvey, P. N. Ciesielski, L. M. Wheeler, P. Schulz, L. Y. Lin, M. C. Beard, and J. M. Luther, Science Advance **3**, eaao4204 (2017).

[4] N. C. Anderson, M. P. Hendricks, J. J. Choi, and J. S. Owen, Journal of the American Chemical Society **135**, 18536 (2013).

[5] S. W. H. Eijt, A. (Tom) van Veen, H. Schut, P. E. Mijnarends, A. B. Denison, B. Barbiellini, and A. Bansil, Nature materials **5**, 23 (2006).

[6] L. Chai, W. Al-Sawai, Y. Gao, A. J. Houtepen, P. E. Mijnarends, B. Barbiellini, H. Schut, L. C. van Schaarenburg, M. A. van Huis, L. Ravelli, W. Egger, S. Kaprzyk, A. Bansil, and S. W. H. Eijt, APL Materials **1**, 022111 (2013).

[7] W. Shi, S. W. H. Eijt, C. S. Suchand Sandeep, L. D. A. Siebbeles, A. J. Houtepen, S. Kinge, E. Brück, B. Barbiellini, and A. Bansil, Applied Physics Letters **108**, 081602 (2016).

[8] V. Callewaert, R. Saniz, B. Barbiellini, A. Bansil, and B. Partoens, Physical Review B **96**, 085135 (2017).

[9] W. Shi, V. Callewaert, B. Barbiellini, R. Saniz, M. Butterling, W. Egger, M. Dickmann, C. Hugenschmidt, B. Shakeri, R. W. Meulenberg, E. Brück, B. Partoens, A. Bansil, and S. Eijt, Physical Review Letters (submitted) (2018).

[10] B. Shakeri and R. W. Meulenberg, Langmuir : the ACS journal of surfaces and colloids **31**, 13433 (2015).

[11] A. van Veen, H. Schut, J. de Vries, R. A. Hakvoort, and M. R. Ijpma, AIP Conference Proceedings 218, 171 (1990).

[12] M. Weber, K. Lynn, B. Barbiellini, P. Sterne, and A. Denison, Physical Review B **66**, 041305 (2002).

[13] S. W. H. Eijt, P. E. Mijnarends, L. C. van Schaarenburg, A. J. Houtepen, D. Vanmaekelbergh, B. Barbiellini, and A. Bansil, Applied Physics Letters **94**, 091908 (2009).

[14] A. Puzder, A. Williamson, F. Gygi, and G. Galli, Physical Review Letters **92**, 217401 (2004).

[15] V. Petkov, I. Moreels, Z. Hens, and Y. Ren, Physical Review B **81**, 241304 (2010).

Chapter 6

Evolution and Role of Vacancy Clusters at Grain Boundaries of ZnO:Al during accelerated Degradation of Cu(In,Ga)Se_2 Solar Cells revealed by Positron Annihilation

Abstract

Positron Annihilation Lifetime Spectroscopy (PALS) and Doppler Broadening Positron Annihilation Spectroscopy (DB-PAS) depth profiling demonstrate pronounced growth of vacancy clusters at the grain boundaries of as-deposited Al-doped ZnO films deposited as Transparent Conductive Oxide (TCO) on Cu(In,Ga)Se_2 (CIGS) solar cells upon accelerated degradation at 85 ^{o}C/85% relative humidity (RH). Quantitative fractions of positrons trapped either in the vacancy clusters at the grain boundaries or in Zn mono-vacancies inside the grains of ZnO:Al were obtained by detailed analysis of the PALS data using a positron trapping model. The time- and depth-dependence of the positron Doppler depth-profiles can be accurately described using a planar diffusion model, with an extracted diffusion coefficient of 35 nm^2/hour characteristic for in-diffusion of molecules such as H_2O and CO_2 into ZnO:Al TCO films via the grain boundaries, where they react with the ZnO:Al. This leads to increased open volume at the grain boundaries that imposes additional transport barriers and may lead to charge carrier trapping and non-radiative recombination. Simultaneously, a pronounced increase in series resistance and a strong reduction in efficiency of the ZnO:Al capped CIGS solar cells is observed on a remarkably similar timescale. This strongly indicates that these atomic scale processes of molecular in-diffusion and creation of open volume at the grain boundaries play a key role in the degradation of the solar cells.

This chapter is based on the published paper:

W. Shi, M. Theelen, A. Illiberi, N. Barreau, S. J. van der Sar, M. Butterling, H. Schut, W. Egger, M. Dickmann, C. Hugenschmidt, M. Zeman, E. Brück, and S. W. H. Eijt, Evolution and Role of Vacancy Clusters at Grain Boundaries of ZnO:Al during accelerated Degradation of Cu(In,Ga)Se_2 Solar Cells revealed by Positron Annihilation, Physical Review Materials **2**, 105403 (2018)

6.1. Introduction

Thin-film $Cu(In,Ga)Se_2$ (CIGS) solar cells are promising in view of their high efficiency and low cost. Research-cell efficiencies have reached 22.6% for a CIGS cell,[1] currently the highest efficiency for thin-film solar cells employing a single absorber layer, besides (expensive) III-V based solar cells. Recently reported progress in high-efficiency CIGS cells using e.g. alkali post-deposition treatment[2] or alternative buffer layers[3] (Zn(O,S)) leads to high expectations for expanding the commercial application of CIGS solar cells. Nevertheless, stability issues are still drawing considerable attention, since larger-scale commercial introduction of CIGS photovoltaic (PV) technology requires cheap and highly efficient modules with long and predictable lifetimes. Unfortunately, knowledge about the lifetime of CIGS modules is still limited, which is reflected in the results of field studies: degradation rates varying from nearly 0 to approximately 4 percent per year were observed.[4-7] Therefore, considerable costs are made for reliable package materials, which are especially high for flexible modules. These costs can be reduced by more intrinsically stable solar cells. Clearly, environmental degradation of CIGS solar cells needs to be prevented, making the identification of the degradation mechanisms of CIGS solar cells a crucial aspect in their development.

A key component of CIGS solar cells is the transparent conducting oxide (TCO) electrode. Al-doped ZnO (ZnO:Al) is a very promising TCO for photovoltaic cells because of its good optoelectronic properties, which include both high transparency and high electrical conductivity simultaneously. Furthermore, ZnO:Al consists of elements with a high abundancy and is a cheap material. However, ZnO:Al as the TCO window material of CIGS solar cells is notably sensitive to moisture.[7] When exposed to accelerated damp-heat (DH) testing, the optical properties of ZnO:Al exhibit only minor changes, mainly in the infrared region by degradation-induced changes in the charge carrier densities. However, its electrical properties deteriorate significantly.[8] This can be attributed to the decreased charge carrier concentrations[9] and reduced mobility of minority charge carriers,[8,9] caused by an increase in the concentration of scattering centres and changes in the potential barriers at the grain boundaries of the ZnO:Al layer.[8,9] Insights into the electronic and atomic-scale structure of grain boundaries of $Cu(In,Ga)Se_2$ thin film absorber layers is crucial for the development of CIGS solar cells as well, in order to reveal the nature of the influence of the grain boundaries in CIGS on charge carrier transport.[10,11] These grain boundaries also play an important role in understanding the in-diffusion of Na^+ (and K^+) into the $Cu(In,Ga)Se_2$ and CdS layers of CIGS solar cells, a key process in the formation of optimized CIGS/CdS heterojunctions required to achieve very high solar cell efficiencies.[12] Although quite some studies have been performed to monitor the degradation of ZnO:Al TCO films, few characterization techniques can detect the impact of degradation on the nanoscale properties of ZnO:Al film directly. For example, UV-VIS optical reflection-transmission spectroscopy hardly detects any change in the optical spectra in the UV and visible range after degradation. A recent X-Ray Diffraction (XRD) study reveals a pronounced increase in the compressive in-plane stress, which can be attributed to the in-diffusion of molecules and stress

build-up due to the subsequent chemical reactions in the grain boundaries.[13] Nevertheless, it provides an indirect view on the possible mechanism of degradation.

In this study, we apply positron annihilation as a proven depth-sensitive technique[14] in order to examine the depth-resolved changes resulting from damp-heat degradation of unpackaged ZnO:Al/i-ZnO/CdS/CIGS/Mo solar cells deposited on soda lime glass at 85 ^{o}C/85% RH. Positron annihilation spectroscopy is an effective way to probe point defects, and is in particular sensitive to the presence of neutral and negatively charged vacancies.[15] Positron annihilation lifetime spectroscopy (PALS) has a proven sensitivity to determine vacancy concentrations in the range of about 10^{-6} – 10^{-4}, depending on the type of material.[15,16] Point defects are known to have an important effect on the electronic and opto-electronic properties of ZnO. For example, Zn-vacancies act as the dominant type of compensating acceptor in Al-doped ZnO.[17,18] Also, hydrogen may bind to oxygen and form shallow donor complexes in ZnO.[19] Positron annihilation has been used extensively to clarify the nature of vacancy-related defects and hydrogen-vacancy interactions in ZnO and their relationship with the micro-electronic and opto-electronic properties of ZnO and ZnO-based devices.[20-24]

Clearly, in order to gain a better understanding of the degradation mechanism of CIGS cells, it is important to identify and quantify the presence and evolution of such point defects in the ZnO:Al layer. Depending on their kinetic energy, positrons can reach the various individual layers in a CIGS solar cell and provide detailed insights into the defect properties of each individual layers separately, including the ZnO:Al TCO and CIGS absorber layer. In this study, we show that positrons trap and annihilate inside grains as well as at grain boundaries of the ZnO:Al layer. The corresponding positron lifetimes and Doppler broadening momentum distributions provide key information on the growth of open volume defects in the grains and at the grain boundaries, resulting from the accelerated degradation by exposure to moisture and heat. In particular, the type and concentration of vacancy-related defects and their evolution in the ZnO:Al layer during the degradation process were determined by the Positron Annihilation Lifetime Spectroscopy (PALS) and Doppler Broadening Positron Annihilation Spectroscopy (DB-PAS) methods, providing important insights into the mechanisms of the degradation in opto-electronic properties of CIGS solar cells using Al-doped ZnO:Al as TCO by DH accelerated degradation.

6.2. Experimental

The unpackaged CIGS solar cells consisted of a multilayer of aluminium-doped zinc oxide (ZnO:Al)/ intrinsic zinc oxide (i-ZnO)/cadmium sulphide (CdS)/Cu(In,Ga)Se_2 (CIGS)/molybdenum (Mo) on Soda Lime Glass (SLG), with an additional Ag front contact and an additional Ag back contact on the Mo film for the devices used in the photocurrent-voltage (*I-V*) solar cell characterization. The CIGS absorber layer (with an average thickness of 2.6 μm) was produced by 3-stage coevaporation at a maximum deposition temperature of 580 ^{o}C, using a synthesis procedure very similar to the one described in Ref. 25. The CdS layer (with a

thickness of 50 nm) was synthesized using Chemical Bath Deposition (CBD). The ZnO:Al and i-ZnO layers (with a thickness of 220 nm and 50 nm, respectively) were produced by RF-sputtering, using 2 wt% Al_2O_3 for the synthesis of the ZnO:Al layer. The thickness of the Mo coating of the SLG glass was 650 nm. A schematic of the ZnO:Al/i-ZnO/CdS/CIGS/Mo/SLG layer composition of the investigated solar cells is presented (without Ag contacts) in Figure 6.1. Nine samples with a size of about 1.25 cm × 1.5 cm, sawn from a single 2.5 cm × 7.5 cm CIGS solar cell slide produced in Nantes, were degraded simultaneously by exposure to 85^{o}C/85% RH heat-moisture conditions in a damp-heat chamber during various time intervals, with a maximum total degradation time of 1218 hours. According to International Electrotechnical Commission (IEC) standard 61646, 1000 hours of exposure to these conditions should mimic 25 years of field exposure in Miami (it should be noted here that the exact correspondence between accelerated degradation and field testing is topic of debate). Each sample was used to produce a 9x9 mm^2 sample for the positron annihilation measurements and 3x3 mm^2 samples, with a surface area of 8 mm^2 effectively available for optical illumination after the Ag contact was established, for the solar cell device characterization. The differences in the solar cell parameters (V_{OC}, J_{SC}, FF, η), obtained under standard AM1.5 illumination conditions, among 9 samples degraded at the same conditions were not statistically significant (see Table 6.1 for the averaged values). This verifies that the samples sawn from the single large solar cell slide were rather uniform, and their degradation behaviour at different time intervals can be directly compared. As described in Ref. 26, *I-V* measurements were performed by a Keithley 2440 5A source meter, with the data collection system positioned outside the damp-heat chamber. The series and shunt resistance of the solar cell were determined by the definition of the slope of the *I-V* curves. After each degradation step at Solliance/TNO Eindhoven, the samples without Ag electrodes were sealed and sent to Delft University of Technology for the positron annihilation measurements. The samples were stored in an Ar-filled glovebox when they were not measured.

Doppler Broadening Positron Annihilation Spectroscopy (DB-PAS) measurements were performed at room temperature using the mono-energetic positron beam VEP. The implantation energy of positrons was varied from 0.1 keV to 25 keV. The intensity of the low-energy positron beam at sample position is around 10^4 e^+/s, and the FWHM size of the beam is 7 mm in diameter.[27] A liquid-nitrogen-cooled high-purity Ge (HPGe) detector with an energy resolution of 1.3 keV was used to determine the energy of the emitted annihilation γ-rays. The Doppler broadening of the photopeak is determined by the electron momentum distributions $N^{2\gamma}(p)$ as seen by the annihilating positrons. S and W parameters were extracted from the measured Doppler broadened annihilation γ-ray photo-peak, defined as the fraction of counts in the central region and in the wing regions of the 511 keV annihilation photo-peak ($N^{2\gamma}(p)$), respectively. The momentum windows used to deduce the S parameter and W parameter are $p_L < 0.41$ a.u. (1 a.u. = 7.2974 $\cdot 10^{-3}$ $m_o c$) and 1.12 a.u. < p_L < 3.21 a.u., respectively, with longitudinal momentum $p_L = 2\Delta E/c$ and ΔE the Doppler shift in energy of the detected annihilation γ-ray. The S parameter is a measure of positron annihilation with valence electrons, which provides sensitivity to the electronic structure and the presence of open volume defects such as vacancies or vacancy

clusters.[16,28,29] The increase in concentration or size of vacancies or vacancy clusters in an otherwise identical material generally leads to an increase of the S parameter. The W parameter is a measure of annihilation with (semi-)core electrons which provides chemical sensitivity to the positron trapping site.[16,28,29] The S-parameter depth profiles were analyzed using the VEPFIT program, which solves the full positron implantation-diffusion problem for a system of layers and calculated S(*E*) curves are fitted to the experimental data, with the S-parameter of the respective layer, its thickness and positron diffusion length for each layer with a given mass density as fit parameters. Makhovian implantation profiles were assumed with an average implantation depth (in nm) according to $z_{ave} = \alpha_p E^n/\rho$, with the positron implantation energy E in keV, the empirical value for the exponent set at n=1.62, α_p = 4.0 μgcm^{-2}keV$^{-1.62}$ and the density ρ in g/cm^3.[28]

Coincident Doppler Broadening (CDB) was used to determine the electron-positron momentum distributions $N^{2\gamma}(p)$ at higher momentum resolution and significantly reduced background. The CDB measurements were performed using the intense reactor-based low-energy positron beam POSH. The intensity of the POSH beam is around $1 \cdot 10^8$ e^+/s, and the positron implantation energy can be varied between 0.1 keV and 13.5 keV.[30] Two collinear HPGe detectors were used to increase the peak-to-background ratio in the electron-positron momentum distributions collected at an energy resolution of 0.9 keV in the CDB experiments. At each selected positron implantation energy, 10^7 counts of positron annihilation events were collected. The 1D electron-positron momentum distributions obtained from the CDB measurements were normalized to the reference 1D electron-positron momentum distribution obtained for a hydrothermal (HT) grown ZnO single crystal (Mateck GmbH) at a positron implantation energy of 12 keV.

The CIGS solar cells were further examined in positron annihilation lifetime spectroscopy (PALS) studies using the pulsed low-energy positron lifetime spectrometer (PLEPS) instrument[31] of the neutron induced positron source (NEPOMUC) facility[32] at the Heinz Maier–Leibnitz Zentrum (MLZ) research reactor in Garching. Measurements on the CIGS solar cells were performed at selected positron energies between 1 to 18 keV. Around $4 \cdot 10^6$ counts were collected for each lifetime spectrum. The lifetime spectra were fitted by using the LT program.[33]

The morphology and grain size of as-deposited and degraded (1056 h) ZnO:Al films was determined by the scanning electron microscopy using a Nova NanoSEM 650 (FEI) microscope at TNO-Rijswijk.

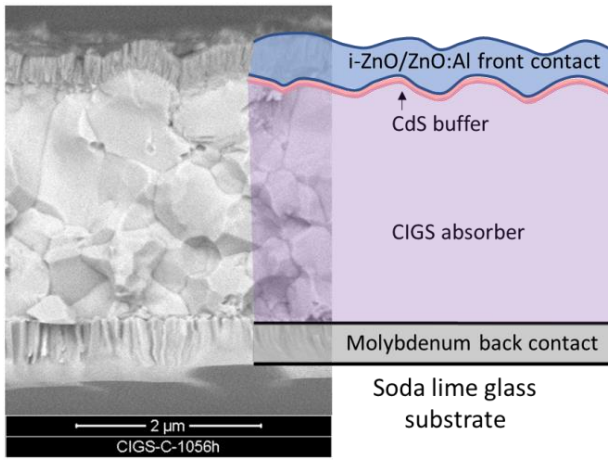

Figure 6.1. Schematic representation of the ZnO:Al/i-ZnO/CdS/CIGS/Mo/SLG layer composition of the CIGS solar cells merged with a representative SEM image.

6.3. Results and Discussion

6.3.1. Time dependence of accelerated degradation of CIGS solar cells

Figure 6.2(a) shows the evolution of the current-density-voltage (*J-V*) curves, determined under AM1.5 illumination, of unpackaged CIGS solar cell devices as a function of accelerated degradation time of up to 683 hours of exposure to temperature-moisture conditions of 85^{o}C/85% RH. The corresponding time-dependence of the solar cell parameters, as extracted from the *J-V* curves and normalized to those of the as-deposited CIGS solar cells, is shown in Figures 6.2(b) and 6.2(c), including the solar cell efficiency (η), Fill Factor (*FF*), open circuit voltage (V_{OC}), short circuit current (J_{SC}), series resistance (R_S), and shunt resistance (R_{sh}). The efficiency of the CIGS solar cells decreases substantially from 14.0% in the as-prepared state to 5.3% after a degradation time of 683 h, demonstrating that substantial degradation takes place on this time scale. Clearly, a major drop in Fill Factor occurs, in parallel to a large increase in series resistance (R_S) and a fast decrease in shunt resistance (R_{sh}). On the other hand, the open circuit voltage V_{OC} and open circuit current J_{SC} show more moderate decreases of 11% and 20%, respectively. Thus, the Fill Factor *FF* is the dominant factor in the decrease in solar cell efficiency, and is in its turn largely affected by both R_S and R_{sh}. The series resistance relates to the transport of current through the semiconductor layers and interfaces of the ZnO:Al/i-ZnO/CdS/CIGS multilayer device, and through the contacts with the Mo film and Ag electrodes. In particular, it is known that the series resistance is very sensitive to changes in the ZnO:Al TCO layer, making it a key factor in the degradation of CIGS solar cells employing Al-doped ZnO as TCO. In order to determine key aspects of the nanoscale mechanism of degradation, detailed insights into the layer-resolved defect evolution in the ZnO:Al/i-ZnO/CdS/CIGS thin film solar cells is gained by employing depth-sensitive positron annihilation methods, as described in the next Sections.

(a)

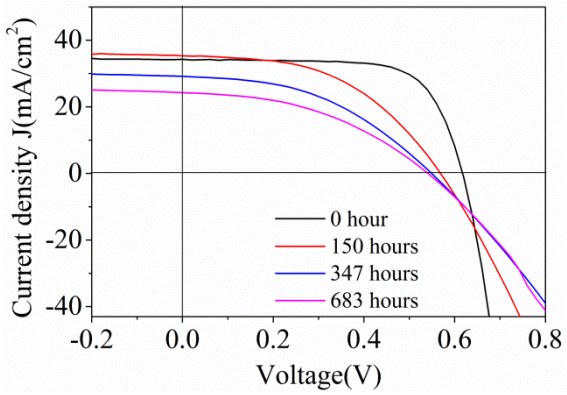

(b)

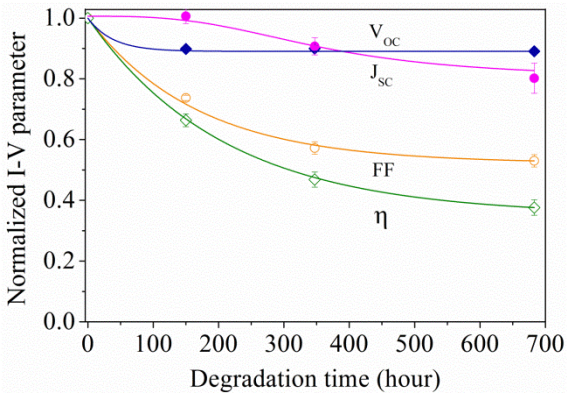

(c)

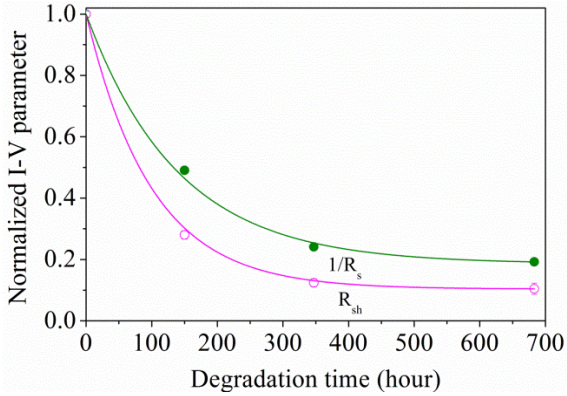

Figure 6.2. (a) Current-density-Voltage (J-V) curves at AM1.5 illumination of CIGS solar cells degraded from 0 h to 683 h at 85°C/85% RH. (b) CIGS solar cell parameters as a function of damp-heat degradation time, normalized to the parameters for the as-deposited state; open circuit voltage, V_{OC} (blue solid diamonds), short circuit current, J_{SC} (magenta solid circles), Fill Factor, *FF* (orange open circles), efficiency, η (green open diamonds). (c) Shunt resistance, R_{sh} (magenta open circles), and inverse of the series resistance, $1/R_s$ (green solid circles) as a function of damp-heat degradation time, normalized to the parameters for the as-deposited state.

Table 6.1. Current-density-Voltage (J-V) parameters for as-prepared CIGS solar cells under AM1.5 illumination (error bars correspond to 1 standard deviation derived from measured values for 9 samples)

CIGS solar cells	η (%)	*FF* (%)	V_{OC} (mV)	J_{SC} (mA/cm^2)	R_s (Ohm cm^2)	R_{sh} (Ohm cm^2)
as-deposited	14.0±0.3	72.1±0.3	604±5	32.3±0.5	2.2±0.1	840±20
683-hour degradation	5.3±0.3	38±2	537±4	26±2	12±2	88±20

6.3.2. Doppler Broadening depth profiles of as-deposited and degraded CIGS solar cells with a ZnO:Al TCO top layer

In order to examine which parts of the CIGS solar cell are degraded during the damp-heat treatment, we first used positron Doppler broadening depth-profiling to monitor the ZnO:Al/i-ZnO/CdS/CIGS/Mo samples as a function of degradation time at 85 ℃ and 85% RH (Figure 6.3). The S parameter of the as-deposited sample shows a rapid decrease as a function of positron implantation energy in the low energy range up to about 1.5 keV (Figure 6.2(a)) due to (1) annihilation of epithermal (i.e. non-thermalized) positrons,[28] and (2) the decrease in fraction of positrons (with increased implantation energy) that, after implantation and thermalization in the sub-surface region, are able to diffuse back and annihilate at surface.[28] Correspondingly, a rather short *effective* positron diffusion length of $L_+ = 2 \pm 1$ nm was extracted by VEPFIT analysis[28] of the S(E) and W(E) depth profiles. Subsequently, a plateau is reached where positrons probe the Al-doped ZnO TCO layer, after which the S-parameter increases gradually up to the highest positron implantation energy of 25 keV where positrons primarily are stopped and annihilate in the CIGS absorber layer, corresponding to an average positron implantation depth of about 1.1 μm. The Mo metal electrode layer underneath the CIGS absorber layer was situated at too large depth below the surface of the solar cell and could thus not be detected. The dependence of the W parameter on positron implantation energy shows a similar, mirrored pattern (Figure 6.3(b)).

The depth profiles of the as-deposited sample could be fitted using VEPFIT analysis with three layers, ZnO:Al, CdS and CIGS (Table 6.2 and Figure 6.4). The presence of the thin intermediate CdS buffer layer was hidden and was not revealed in the positron depth profiles, since its characteristic S and W parameter are in-between those of ZnO:Al and CIGS, as determined for other samples where the ZnO:Al TCO was not deposited and the CdS layer formed the top layer. The presence of the CdS buffer layer was experimentally verified by Raman spectroscopy using an Ar ion laser at 514.5 nm, since the Raman spectra were dominated by the characteristic wurtzite CdS LO peaks at 302 cm^{-1} and 605 cm^{-1}. The parameters for the CdS layer are given in Table 6.2 and were kept constant in the VEPFIT analysis. In the VEPFIT model, the ~50 nm i-ZnO layer was included as a part of the bottom ZnO:Al layer, assuming the same S and W parameters as the bottom ZnO:Al layer both in the as-prepared state and during the degradation process. Table 6.2 provides an overview of the best-fit parameters for the three layers. The

fractions of positrons annihilating in each layer of the as-deposited CIGS solar cell, extracted using VEPFIT analysis, are shown in Figure 6.4 as a function of positron implantation energy.

(a) (b)

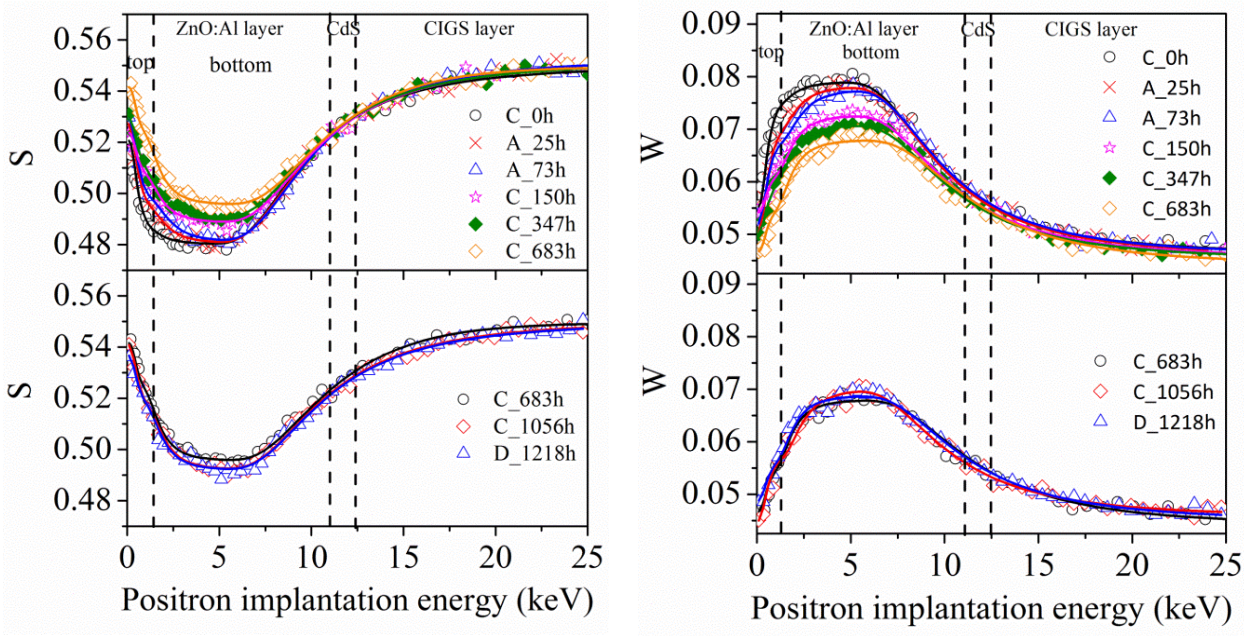

Figure 6.3. (a) Doppler S parameter as a function of positron implantation energy for CIGS solar cells at various degradation times at 85°C/85% RH. Symbols are experimental data and solid lines are fit curves obtained by VEPFIT analysis employing a 4-layer model (3-layers for the as-deposited state). (b) Doppler W parameter as a function of positron implantation energy for CIGS solar cells at various degradation times at 85°C/85% RH.

Figure 6.3 shows that the degradation leads to pronounced changes in the S and W parameter at low positron implantation energies. The S parameter shows a strong increase already for relatively short degradation times of 25 and 73 h in the low energy range up to 4 keV. The rise in S parameter continues for longer degradation times up to 683 h, extending towards increasingly higher positron implantation energies of up to at least 8 keV. This indicates that the nanostructural changes of the ZnO:Al layer occur at increasingly large depths below the surface with prolonged degradation time, consistent with an in-diffusion mechanism in which in-diffusion of atmospheric molecules such as H_2O and CO_2 plays a key role.[8,26] A saturation of the S and W of the ZnO:Al layer seems to set in for longer degradation times beyond 683 h. As shown in Figure 6.3, there is no visible change in the CIGS absorber layer, while the accelerated degradation affects the ZnO:Al layer substantially. This result is consistent with previous research,[8,26] which indicated that the CIGS solar cell degradation mechanism induced by damp-heat exposure can be mainly attributed to the degradation of ZnO:Al TCO and the Mo metal back-contact. The increase in S and decrease in W suggest that the degradation of the ZnO layer involves the formation of open volume, such as mono-vacancies or small vacancy clusters. Namely, trapping of positrons in neutral or negatively charged vacancies leads to less overlap

with core electrons, while valence electron orbitals of the surrounding atoms extend farther into the open space where the positron resides. The resulting higher fraction of annihilation with valence electrons leads to the detected increase in the S parameter. Also, the S parameter of the surface is seen to increase, which is expected in view of the large changes that start at the surface and in time affect a substantial part of the ZnO:Al layer.

Table 6.2. VEPFIT analysis best-fit parameters for as-deposited CIGS solar cell using a 3-layer model

layer	Density (g/cm^3)	L_+ (nm)	Layer width (nm)	*S* parameter	*W* parameter
ZnO:Al	5.606	2	257	0.482±0.0002	0.078±0.001
CdS	4.83	2	18	0.554±0.0003	0.041±0.001
CIGS	5.7	2	∞	0.550±0.0003	0.046±0.001

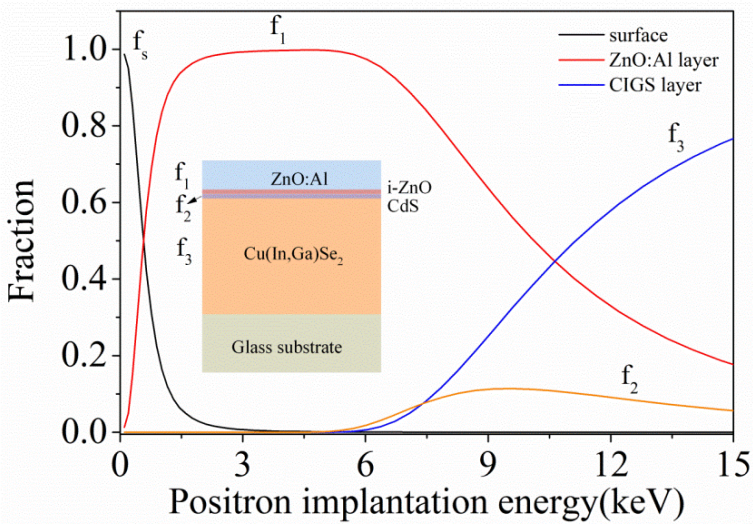

Figure 6.4. Fraction of positrons that annihilate in each layer of the as-deposited ZnO:Al/CIGS solar cell as a function of positron implantation energy, extracted from the VEPFIT program; f_s – surface, f_1 – ZnO:Al/i-ZnO, f_2 – CdS, f_3 –CIGS.

In order to gain a better insight into the nature of the observed changes in the Doppler depth profiles and the evolution of the involved defect structures during the degradation process, we first employed a conventional approach to the analysis of the depth profiles, assuming a layered model within VEPFIT. Once degradation had started, a satisfactory analysis of the depth-profiles of the degraded samples could only be obtained using four layers instead of three layers, as was immediately visible by eye judged from the comparison of experimental and fit curves, confirmed by the strong difference in χ^2–parameter obtained from the VEPFIT analysis using either three or four layers in the model. Now, two layers (a top layer and a bottom layer) were required to fit the Al-doped ZnO TCO layer satisfactorily, and further a thin CdS buffer layer and the CIGS layer were included. Figure 6.5 presents the extracted evolution of S and W parameters in the top ZnO:Al layer with a thickness of 20±3 nm and in the bottom layer of ZnO:Al (260±15 nm) as a function of degradation time. At the start of the degradation process,

the S parameter of the top layer increases rapidly while the S parameter of the bottom layer still stays constant and starts to increase only after a delay of about 50-100 h. This delay points to a direct connection to the diffusion process which has been proposed as primary cause for the solar cell degradation, involving molecules such as H_2O and CO_2 from the atmospheric environment in the DH chamber that penetrate and diffuse into the layer, starting from the surface.[8] Furthermore, Figure 6.5 shows that the S and W parameter in both the top and bottom layers level off for degradation times beyond about 400 hours, indicating that the nanostructural changes of the ZnO:Al TCO layer occur on a time scale similar to the decay of the solar parameters such as solar cell efficiency and series resistance (Figure 6.1). This suggests a direct relationship between the in-diffusion of environmental gas molecules leading to solar cell degradation and the formation of additional open volume defects such as vacancies or vacancy clusters in the ZnO:Al top and bottom layers as a result of the damp-heat accelerated degradation treatment. In the next Section, we therefore present a new way to analyze the depth- and time-dependence of the positron Doppler depth profiles based on a direct connection to the in-diffusion process.

For completeness, in order to examine whether the observed changes could alternatively be primarily due to changes at the surface of the sample, we analysed the S parameter depth profiles using two alternative models.[34] The analysis shows that both of these models can be disregarded, however, either (1) because of failure to provide satisfactory fits to the Doppler depth profiles (model S1), or (2) the model leads to parameters inconsistent with the evolution of defects in the ZnO:Al (model S2). Noteworthy, model S2 shows that surface annihilation contributes to at most a (very) minor fraction in the range of positron implantation energies of 2-8 keV.[34] Figure 6.4 shows that at 1 keV surface annihilation contributes only ~10% to the positron annihilation, and consequently the variation in surface annihilation cannot explain the large changes observed in the range from ~1 keV and beyond.

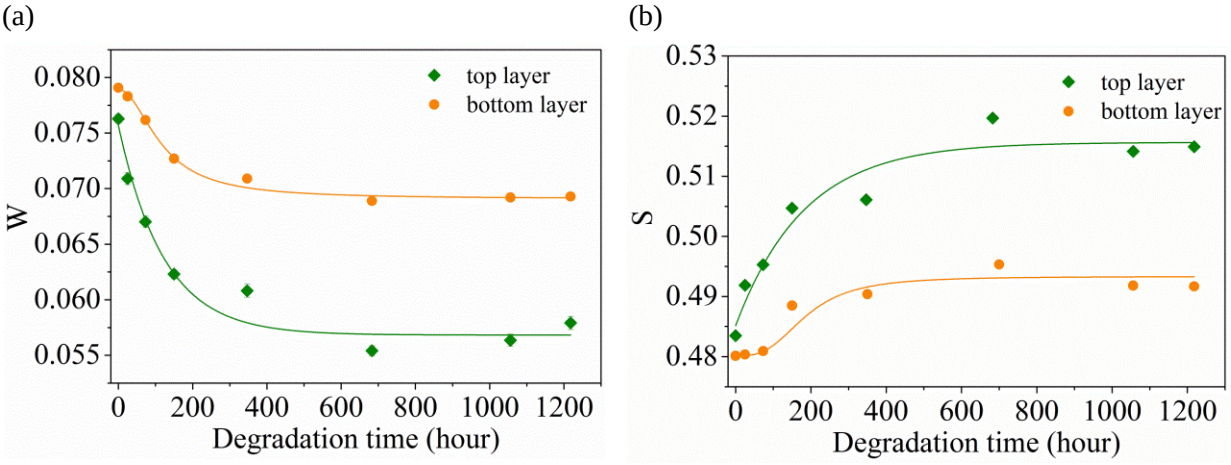

Figure 6.5. (a) S and (b) W parameters as a function of the damp-heat degradation time for the 20±3 nm ZnO:Al top layer and 260±15 nm ZnO:Al bottom layer, respectively, obtained from VEPFIT analysis of Doppler S and W depth profiles.

6.3.3. Diffusion model analysis of the degradation-induced changes in the Doppler-broadening depth-profiles

In order to examine whether the evolution of the Doppler depth profiles is consistent with an in-diffusion mechanism as suggested by the evolution of the S and W parameters with degradation time, we apply in this Section, an in-diffusion model to fit the depth- and time-dependence of the changes in the S(E) and W(E) profiles caused by accelerated degradation of the CIGS solar cells. When exposed to 85 ^{o}C/85% RH conditions, atmospheric species such as H_2O and CO_2 diffuse into the ZnO:Al layer covering the remainder of the CIGS solar cell. The in-diffusion may occur through the grain boundaries of the ZnO:Al film, and also, possibly generated H^+ might diffuse into the bulk of the grains. The in-diffused molecules will chemically react with the ZnO:Al at the grain boundaries, leading to the local removal of atoms and to the creation of new phases such as $Zn(OH)_2$ and Zn-based carbonates which may exert a stress on the local environment.[8,13] These processes may therefore induce the formation of additional open volume at the grain boundaries as well as increase the size and/or concentration of vacancies inside the grains, respectively, as indicated from the Doppler broadening experiments by the increase in S parameter.

To the author's knowledge, a model that takes into account the effect of a diffusion-related depth distribution of open volume defects on positron Doppler broadening depth profiles has not been reported in literature, and we describe the model in more detail in Appendix A (section 6.5). Briefly, in the diffusion model, it is assumed that the concentration of in-diffused atmospheric species is described by planar one-dimensional diffusion in a semi-infinite medium at a diffusion coefficient *D* that we assume to be constant over time and depth below the surface. The solution of the corresponding diffusion equation with concentration *C(0)* at the surface can be expressed by an error function:[35]

$$C(z,t) = C(0)(1 - erf(\frac{z}{2\sqrt{Dt}})), \tag{6.1}$$

where $C(z,t)$ is the concentration as a function of depth z below the surface and t is the degradation time. In the model, we assume that the formation of additional open volume is proportional to the concentration of in-diffused molecules, and that the created open volume defects in turn lead to a proportional increase ΔS and decrease $|\Delta W| = -\Delta W$. In order to derive the dependence on positron implantation energy of $\Delta S(E)$ and $|\Delta W(E)|$, Makhovian distributions of order m=2 for the positron implantation profiles were used, given by:

$$P(z,E) = \frac{2z}{z_0^2} e^{-(z/z_0)^2}, \tag{6.2}$$

where z_0=1.13z_{ave} with the mean depth $z_{ave}=\alpha_p E^n/\rho$, ρ is the density of the ZnO:Al, and E is the positron implantation energy. In the analysis, the parameters α_p=4.0 μgcm^{-2}keV$^{-1.62}$ and n=1.62 were used.[28,36] Diffusion of thermalized positrons is not taking into account in the model, which

limits the validity of the model to the case where the positron diffusion length $L_+ << z_0$,[28,37] *i.e.* for films with moderate to high defect concentrations, or to sufficiently high positron implantation energies. In practice, back diffusion of thermalized positrons to the surface of the ZnO:Al TCO layer as well as epithermal positron annihilation is only appreciable for positron implantation energies ≤ 1.5 keV, indicating that the model can conveniently be applied at energies starting from ~1.5 keV as is included in our analysis implicitly, as explained further on.

One can thus derive that the dependence on positron implantation energy of the changes in the S and W parameter due to the degradation of the ZnO:Al TCO, $\Delta S_{ZnO:Al}(E,t)$ and $\Delta W_{ZnO:Al}(E,t)$, is described by (Appendix A (section 6.5))

$$\Delta S_{ZnO:Al}(E,t) = \Delta S_0 \cdot \left[1 - e^{-(d/z_0)^2} - \int_0^d erf\left(\frac{z}{2\sqrt{Dt}}\right) \frac{2z}{z_0^2} e^{-(z/z_0)^2} dz \right] \tag{6.3}$$

and

$$|\Delta W_{ZnO:Al}(E,t)| = \Delta W_0 \cdot \left[1 - e^{-(d/z_0)^2} - \int_0^d erf\left(\frac{z}{2\sqrt{Dt}}\right) \frac{2z}{z_0^2} e^{-(z/z_0)^2} dz \right] \quad (= -\Delta W), \tag{6.4}$$

with d the thickness of the ZnO:Al TCO layer. $\Delta S_0 = I_{\Delta S} \cdot C(0)$ and $\Delta W_0 = I_{\Delta W} \cdot C(0)$ are the change in *S* and *W* for annihilation of thermalized positrons inside the ZnO:Al just below the surface, with $I_{\Delta S}$ and $I_{\Delta W}$ intensity proportionality pre-factors connecting ΔS_0 and ΔW_0 with the concentration of molecules at the surface $C(0)$. The cut-off at $z = d$ takes into account that at high positron implantation energies more and more positrons annihilate in the CdS and CIGS layers,[28,37] that apparently are not affected by the in-diffusion of molecules. These positrons obviously do not probe the degradation-induced changes in the ZnO:Al layer.

The in-diffusion model was used in numerical simulations for the analysis of the observed changes $\Delta S_{\exp}(E)$ and $-\Delta W_{\exp}(E)$ in the Doppler depth profiles. Figure 6.6(a) presents the experimental curves for the change in S parameter $\Delta S_{\exp}(E,t) - \Delta S_s(t) f_s(E)$ as a function of positron implantation energy, where $\Delta S_{\exp}(E,t)$ is defined as the difference in the depth profile measured after degradation time *t* and that of the as-deposited state. Clearly, the S-parameter of surface annihilation increases with degradation time $(\Delta S_s(t) > 0)$ due to the strong impact of the environmental exposure on the local composition and structure of the ZnO:Al outer surface (Figure 6.3). The factor $\Delta S_s(t) f_s(E)$ accounts for the change in surface annihilation contribution at low positron implantation energies, in which the surface annihilation fraction $f_s(E)$ for the as-deposited sample determined by the VEPFIT analysis was used (Figure 6.4). The contribution of surface annihilation was subtracted from $\Delta S_{\exp}(E,t)$ to show separately the degradation-induced changes that occur in the ZnO:Al layer separately. The change in the S

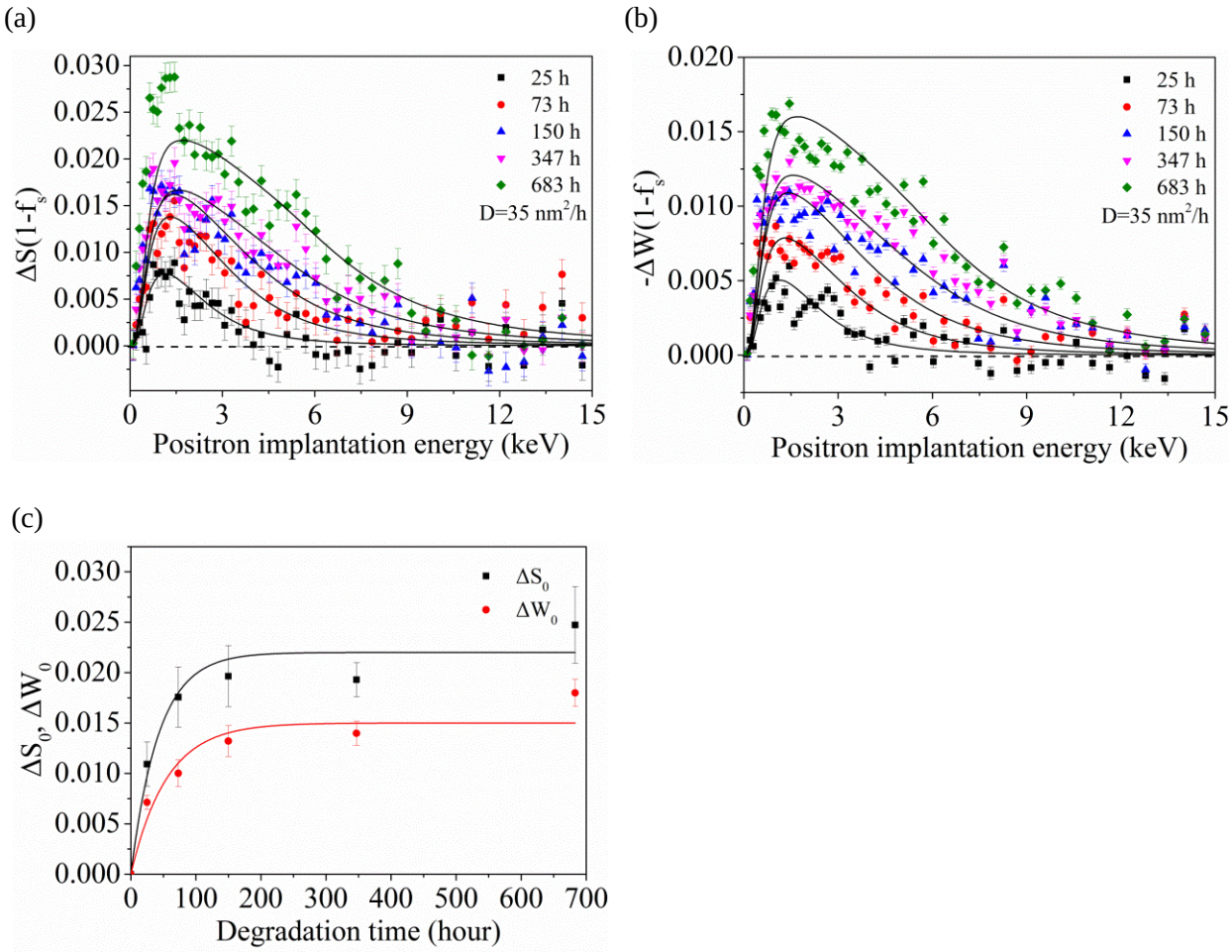

Figure 6.6. Depth-dependence of the change in Doppler depth profiles at various degradation times. (a) $\Delta S_{ZnO:Al}(E)(1-f_s(E))$, (b) $-\Delta W_{ZnO:Al}(E)(1-f_s(E))$, (c) Time-dependence of ΔS_0 and ΔW_0 for the ZnO:Al layer, extracted using the in-diffusion model best-fit analysis (solid lines in diagrams (a) and (b)) described in the text and in Appendix A (section 6.5).

parameter for surface annihilation $\Delta S_s(t)$ was derived from the experimental values at the lowest positron implantation energies. The full curves in Figure 6.6(a) represent best-fits of the experimental data to numerically generated depth profiles $\Delta S_{ZnO:Al}(E,t)(1-f_s(E))$ of the in-diffusion model, where the factor $(1-f_s(E))$ used in the simulations takes into account the fraction of positrons that annihilate at the surface due to back diffusion of thermalized positrons and due to epithermal positrons, which starts to dominate in the low-energy sub-surface range for energies below ~1.5 keV. The corresponding experimental and numerically generated depth profiles for $-\Delta W_{ZnO:Al}(E)(1-f_s(E))$ are given in Figure 6.6(b). The same apparent diffusion coefficient D is used in the best-fit analysis of both S and W for all degradation times. Finally, Figure 6.6(c) presents the degradation-time-dependence of $\Delta S_0(t) = I_{\Delta S}(t)\cdot C(0)$ and $\Delta W_0(t) = I_{\Delta W}(t)\cdot C(0)$ obtained from the analysis based on Eqs. (6.3) and (6.4).

Clearly, the in-diffusion model describes the experimental depth-profiles satisfactorily, using only two independent parameters, the (apparent) diffusion coefficient D and ΔS_0 (or ΔW_0) for all degradation times in the range of 0-683 h. A good agreement with the experimental data as a function of degradation time could be obtained with a diffusion coefficient of $D = 35\ nm^2 / h$. This reveals that the diffusion model provides a good description of the evolution of the S and W depth profiles with the degradation time. Furthermore, Figure 6.6(c) shows that ΔS_0 and ΔW_0 depend in a very similar way on degradation time, providing further support to the validity of the model. Nevertheless, ΔS_0 and ΔW_0 are not constant in the initial phase up to ~200 h of degradation, in contrast to what would be expected if the change in S and W at depth *z* is directly proportional to the concentration of in-diffused molecules. This can be understood, since S and W not only depend on the concentration of in-diffused molecules, but also on the type of vacancy-related defects, in particular their size. The initial increase in ΔS_0 and ΔW_0 thus seems to reflect the growth in size of the vacancy clusters. This is indeed observed in the PALS experiment described in Section 6.3.5 and is furthermore inferred from the evolution of the coincidence Dopper broadening momentum distributions described in Section 6.3.4 for degradation times up to 150 h. The initial increase in ΔS_0 and ΔW_0 thus reflects the fact that the S and W parameters are a measure for the open volume created by the in-diffusion of molecules and release of local stress induced by chemical reactions, rather than a direct measure for the concentration of in-diffused molecules.

We note that, for long degradation times, the model curves in Figures 6.6(a,b) deviate slightly from the experiment data at low positron energy. This points to more severe changes in the near-surface region that occur upon prolonged degradation and are not accounted for in the model. This may also affect the fraction of positrons that can diffuse back and annihilate at the surface, changing the surface annihilation fraction $f_s(E)$, which is assumed here to remain the same for all degradation times, identical to that for the as-deposited sample as derived from VEPFIT analysis.

The diffusion coefficient of $D = 35\ nm^2 / h$ extracted from the analysis should be considered as an apparent diffusion coefficient, since the model assumes that the open volume generated is proportional to the number of in-diffused molecules, while the actual relationship can be more complex. Nevertheless, within this assumption, the apparent diffusion coefficient can be used to estimate the characteristic time scale of in-diffusion of molecules into the ZnO:Al layer with a thickness of $d = 280nm$. Using $d = 2\sqrt{Dt^*}$, we obtain $t^* = d^2 / 4D \sim 560\ h$, which is the time scale on which the changes in the positron Doppler depth profiling experiments are seen to saturate. Noteworthy, it is remarkably similar to the time scale on which important solar cell parameters such as the series resistance and solar cell efficiency are seen to decay, demonstrating that the process behind the changes in the Doppler depth-profiles, i.e. creation of

open volume by in-diffusion of molecules, is one of the key processes leading to degradation of the solar cells.

In order to determine the type and concentration of the open volume defects involved, we analyzed the S and W parameters of the ZnO:Al films by comparison to two hydrothermally grown ZnO single crystals, and performed Coincidence Doppler Broadening (CDB) and Positron Annihilation Lifetime Spectroscopy (PALS) experiments described in the next Sections 6.3.4 and 6.3.5.

6.3.4. Doppler broadening identification of the vacancies generated in the ZnO:Al layer

6.3.4.1. Evolution of the S-W points of the top and bottom ZnO:Al layer with degradation time

In order to examine which types of open volume defects correspond to the observed changes in Doppler parameters with degradation time, the S-W points obtained from the conventional layer-model VEPFIT analysis (Section 6.3.2) for the ZnO:Al top and bottom layer, respectively, are presented in the S-W diagram of Figure 6.7. The S-W points were normalized with respect to that of the first ZnO single crystal (c-ZnO #1).[34] The S-W point of the second ZnO single crystal (c-ZnO #2) shows a small difference compared to the first ZnO single crystal, which does not affect the main conclusions deduced from the S-W analysis. The solid line indicates the direction of change in S-W parameters going from positron annihilation in defect-free c-ZnO to the characteristic S-W point for positron annihilation in the Zn mono-vacancy in ZnO ($S(V_{Zn})/S_{ZnO} \cong 1.055$, $W(V_{Zn})/W_{ZnO} \cong 0.81$), where the average of the values reported in Ref. 38 and Ref. 39 was used. In the interpretation of the (normalized) S-W diagram it should be taking into account that our positron annihilation lifetime and Doppler broadening studies indicated that the HT grown ZnO crystals contain a significant concentration of positron trapping point defects.[34] As reported in previous studies on HT grown c-ZnO, these might correspond to negatively charged substitutional Li on Zn positions (Li_{Zn}^{-})[42,61] and/or zinc monovacancies decorated with a hydrogen atom (V_{Zn}:H).[40] Saturation trapping at such types of defects is expected to lead to a shift in S-parameter of the order of +1% to +2% for the c-ZnO crystals compared to defect-free ZnO.[40, 42, 61] Therefore, the 'true' reference point for defect-free ZnO is expected to be located somewhat further away into the top-left direction of Figure 6.7, and the S-parameter for saturation trapping in a Zn monovacancies is expectedly to be located roughly around $S(V_{Zn})/S_{c\text{-}ZnO}$~1.03-1.04 in this S-W diagram. Also, it should be noted that even normalized values of S and W are affected by the energy resolution of the HPGe detector and the energy windows for S and W.[60] The detector resolution and energy windows employed in this study are close to the corresponding settings of Ref. [38] and [42], resulting in a systematic difference in normalized S of at most -0.3%.

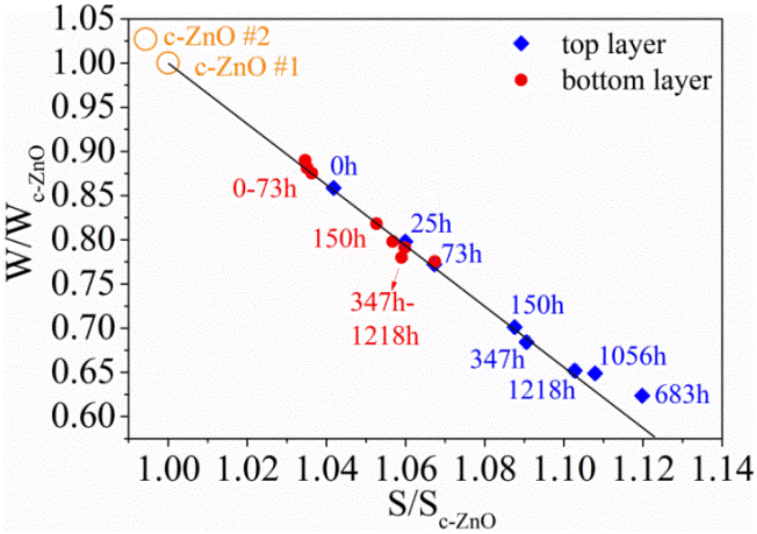

Figure 6.7. Evolution of the S-W parameters for the top layer (blue solid diamonds) and bottom layer (red solid circles) of the ZnO:Al with degradation time, presented as ratio to the S-W parameters of the single crystal c-ZnO #1. The orange open circles are the reference S-W points for c-ZnO (#1 and #2). The solid line indicates the characteristic direction of change in S-W from defect-free ZnO to the Zn mono-vacancy in ZnO.[38,39,41]

Nevertheless, it is clear that the S-W points for the top and bottom layer of the as-deposited sample are positioned on a line that is very close to the shift direction between the S-W points of ZnO and the Zn mono-vacancy in ZnO. This indicates that most positrons trap and annihilate in Zn mono-vacancies in the ZnO:Al film, while some positrons may even annihilate in larger vacancy clusters already for the as-deposited films. Upon degradation, a strong shift towards higher S and lower W is observed, resulting from increased positron trapping in open volume defects with a size larger than a monovacancy,[41] consistent with our quantitative results obtained using positron annihilation lifetime spectroscopy (PALS) as described in Section 6.3.5. The top layer contains more or larger positron trapping vacancy clusters[41] both in the as-deposited state and after prolonged degradation as compared to the bottom ZnO layer, as will be quantitatively discussed in Section 6.3.5 based on our PALS results. Clearly, the quantitatively different behavior in the bottom layer, with less open volume generated compared to the top layer, is consistent with the diffusion model presented in the previous Section 6.3.3.

6.3.4.2. Coincidence Doppler Broadening ratio curves

Further support for presence of these types of vacancy-related defects in the ZnO:Al layer and their evolution upon degradation comes from coincidence Doppler broadening (CDB) spectra collected at a positron implantation energy of 1.4 keV and 5 keV. These energies correspond to mean positron implantation depths centered in the top and the bottom layer of the ZnO:Al TCO, respectively. Figure 6.8 shows the 1D electron-positron momentum distributions extracted from the CBD measurements, presented as the ratio to the momentum distribution for the ZnO single crystal #1.

The ratio curves presented in Figure 6.8(a) for the ZnO:Al top layer in the as-deposited state and after 25h of degradation show very similar features as that for the Zn mono-vacancy in ZnO reported in previous experimental and theoretical studies,[41] indicating the presence of Zn mono-vacancies already in the as-deposited films. Upon prolonged degradation for 150 to 683 hours, the shape of the ratio curves changes remarkably. The shoulder at 1.3 a.u. and valley around 2 a.u. characteristic for annihilation in Zn mono-vacancies flatten out. Simultaneously, the intensity at high momenta reduces substantially, while the intensity at low momenta below 0.5 a.u. is seen to increase further. This clearly indicates that positron annihilation at (larger) vacancy clusters starts to dominate after prolonged degradation on a time scale of 150-683 h, consistent with the evolution of the Doppler S and W parameters discussed in the previous sub-Section 6.3.4.1 and the PALS spectra in Section 6.3.5.

The features of the ratio curve for the ZnO:Al bottom layer in the as-deposited state presented in Figure 6.8(b) are also very similar to the ratio curve calculated for the Zn mono-vacancy. However, the features are somewhat flattened out towards the bulk reference. Thus, Zn mono-vacancies are clearly also present in the bottom layer, albeit that the concentration of open volume defects seems smaller than in the top layer. Upon degradation, the ratio curve of the bottom layer increases below 0.5 a.u. and decreases in the full range beyond 0.5 a.u., quite similar to the ratio curves of the top layer. Nevertheless, the shoulder at 1.3 a.u. and the valley at 2 a.u. remain here distinctly visible, revealing that Zn mono-vacancies stay more dominant, even though larger vacancy clusters start to contribute for degradation times of 150 h and longer. This is fully consistent with the evolution of the S-W point of the bottom layer and the inferred formation of (smaller) vacancy clusters with prolonged degradation, as discussed in the previous sub-Section 6.3.4.1, and consistent with the PALS results discussed in the next Section 6.3.5.

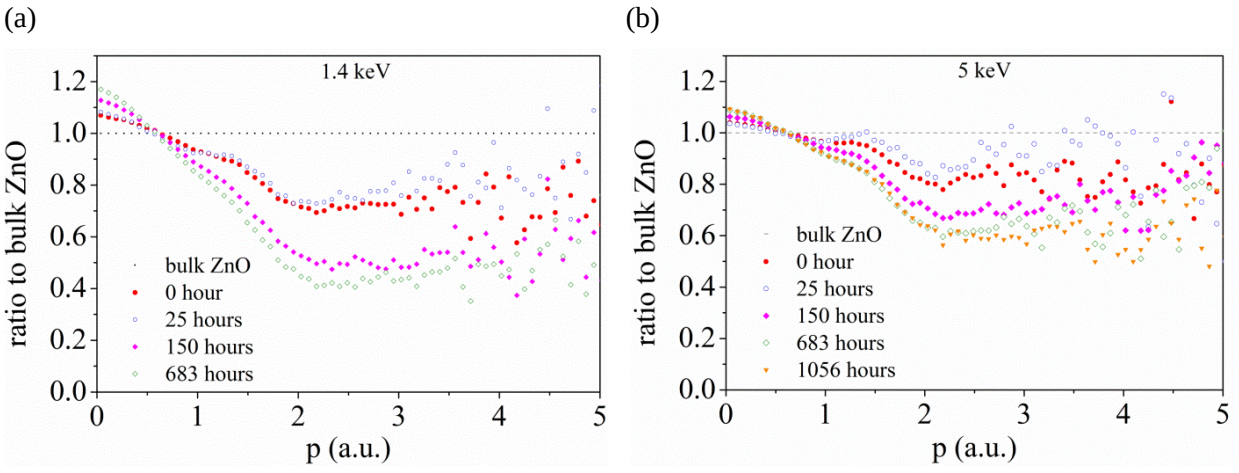

Figure 6.8. Ratio curves of the 1D electron-positron momentum distributions as a function of the degradation time, obtained from coincidence Doppler broadening (CDB) measurements at a positron implantation energy of (a) 1.4 keV, and (b) 5 keV, respectively. The data are presented as the ratio to the 1D electron-positron momentum distribution of c-ZnO #1 collected at 12 keV. (a.u. = atomic units, 1 a.u. = $7.2974 \cdot 10^{-3}$ $m_o c$)

6.3.5. Evolution of the size of vacancies and vacancy clusters as extracted from Positron Annihilation Lifetime studies

Positron Annihilation Lifetime Spectroscopy (PALS) is a sensitive method to probe the size and concentration of vacancy-related defects. Therefore, positron lifetime spectra were collected at selected positron implantation energies for the ZnO:Al based CIGS solar cells at various stages of degradation, including 0 h, 73 h, 600 h, 1056 h and 1218 h of accelerated degradation. The positron lifetime spectra were fitted by using the LT program with four lifetime components. Figure 6.9 shows the lifetimes and intensity of the two major (short) lifetime components in the spectra for the top layer (corresponding to averaged values obtained from the two PALS spectra collected at 1 and 2 keV) and the bottom layer (collected at 5 keV) of ZnO:Al at the beginning of the degradation process (0 hour and 73 hours) and after long-time degradation (600 hours, 1056 hours and 1218 hours). The third and fourth positron lifetimes are in the range of 1 to 5 ns, but show very low intensities between 0.2% and 3%, demonstrating that large voids and corresponding formation of ortho-positronium are nearly absent. For the top layer, a short lifetime τ_1 for the as-deposited sample of 224±5 ps is obtained from the LT analysis, which is in the range of 220-240 ps reported for the Zn mono-vacancy.[42,43] The second lifetime τ_2 of 369±9 ps is due to larger vacancy clusters (Figure 6.9(a)), and corresponds to a size of the order of a six-vacancy, since the lifetime is similar to that of a $3V_{Zn}$-$3V_O$ vacancy cluster according to theoretical calculations presented in Ref. 17. Upon prolonged degradation for t=1218 h, τ_1 and τ_2 of the top layer increase to 256±5 ps and 438±7 ps, respectively, revealing an increase in the size of vacancies. In particular, these lifetimes indicate that multi-vacancies (possible tri-vacancies or four-vacancies such as $V_{Zn-m}V_O$, m=2, 3)[41] and larger vacancy clusters with a typical size similar to 6 missing V_{Zn}-V_O pairs, respectively, are formed in the top layer of ZnO:Al. In the bottom layer of ZnO:Al, the trend is similar to the top layer. However, τ_1 stays more constant in the range of 224 ps to 242 ps during the accelerated degradation process, while the second lifetime τ_2 of 321±8 ps at the beginning of the degradation process is smaller than that in the top layer (369±9 ps), and increases to a value of ~410 ps after prolonged degradation, indicating that the open volume defects in the bottom layer grow also, but they stay smaller than in the top layer. Most likely the lifetime of 242±5 ps still corresponds mainly to annihilation in Zn mono-vacancies with some divacancies present, while the longer lifetime of ~410 ps points to vacancy clusters with a size of the order of 4 missing V_{Zn}-V_O pairs.

As shown in Figure 6.9(b), the intensity of the short lifetime τ_1 component of 64% for the top layer of as-deposited ZnO:Al, is about 1.8 times larger than that for the long lifetime τ_2 component (35%) at the beginning of the degradation process, showing that around two third of positrons trap and annihilate in Zn mono-vacancies, while around one third of positrons annihilate in the larger open spaces such as six-vacancies. Upon prolonged degradation, the intensity of the short lifetime component first remains rather constant up to a degradation time of 600 h, and decreases from 64% to 56% for the longest degradation times, while the fraction for the second lifetime component increases from 35% to 40%, which might indicate that the concentration of large vacancy cluster has increased, leading to increased trapping and

annihilation of more positrons in the larger vacancy clusters. However, since the vacancy clusters have grown, it should be noted that the trapping efficiency of the open volume defects may also have increased, which will lead to an increase in the intensity of the second lifetime component as well. For the bottom layer of as-deposited ZnO:Al, 74.5% of positrons trap and annihilate in the Zn mono-vacancies, while 25% annihilate in the large vacancy clusters at the start of the degradation process. Upon prolonged degradation beyond 600 h, the intensity of the short lifetime component decreases for the bottom layer also, while the intensity of the second lifetime component increases (Figure 6.9(b)), indicating preferred trapping in more abundant larger vacancy clusters for the bottom layer of the ZnO:Al as well. Thus, the bottom layer shows a similar behavior as the top layer, albeit that smaller open space is present and created. The smaller intensity of the second lifetime component compared to that for the top layer indicates that this also leads to less trapping at the vacancy clusters.

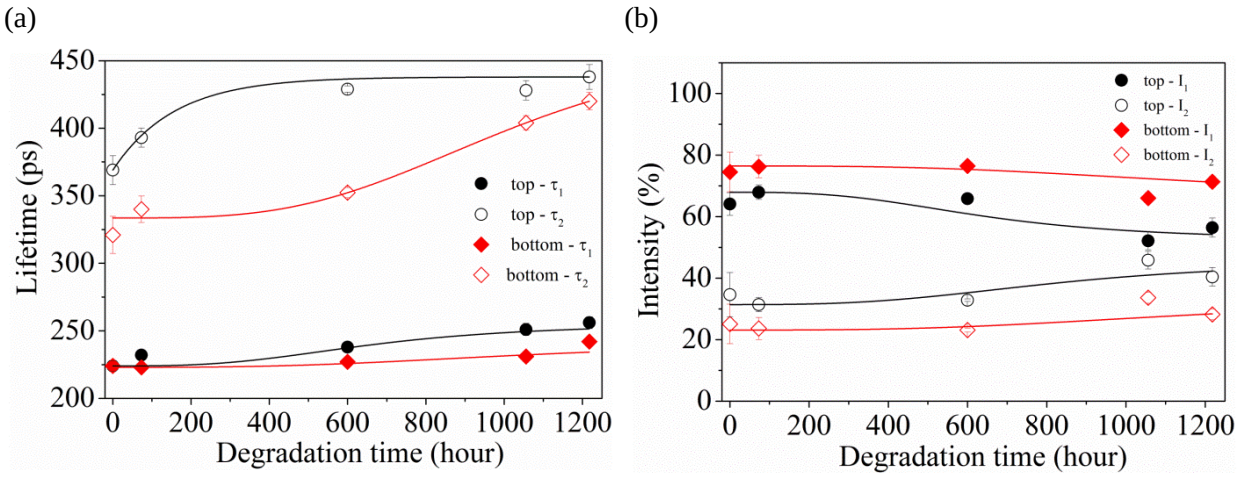

Figure 6.9. (a) Positron lifetime τ_1 and τ_2, and (b) intensity I_1 and I_2 for the top and bottom layer of the ZnO:Al TCO of a CIGS solar cell as a function of time of accelerated degradation. Full lines are guides-to-the-eye.

Clearly, the shortest lifetime τ_1 corresponds to positron trapping in the Zn mono-vacancies, which could be located either in the bulk of a ZnO:Al grain or at the grain boundaries of ZnO:Al. Noteworthy, in n-type Al-doped ZnO the formation of Zn mono-vacancies is favorable,[44] where they form the dominant charge compensating acceptor defects.[22,45] Trapping in Zn mono-vacancies, formed inside ZnO:Al grains during deposition, can thus be expected. However, it should be noted that some of the detected Zn mono-vacancies could correspond to similarly sized open space at the grain boundaries, since the formation energy of Zn vacancies at grain boundaries is also relatively low compared to the case of pure ZnO.[46] The second lifetime component points to the presence of larger vacancy clusters which most likely are located at the grain boundaries, as was also proposed in some previous studies[43,47] and is inferred from the diffusion model analysis presented in the previous Section 6.3.3. The picture thus emerges that the as-deposited ZnO:Al layers contain Zn mono-vacancies inside the grains and larger vacancy clusters at their grain boundaries. During accelerated degradation, the larger vacancy clusters at

the grain boundaries show a pronounced increase in size, while their concentrations possibly do not change significantly except for the longest degradation times of ~1000 h and beyond, as indicated by the positron lifetime intensities.

In the next Section we provide evidence for the emerging picture of positron trapping in Zn mono-vacancies inside the ZnO:Al grains and in larger vacancy clusters at their grain boundaries. The evidence is obtained by analysis of the collected positron annihilation lifetimes and intensities in the framework of a detailed positron trapping model involving grain boundaries and vacancies inside the grains as trapping sites, as developed by Würschum *et al.*.[48]

6.3.6. Positron trapping model with intragranular vacancies and grain boundary trapping

In the grain boundary positron trapping model presented by Würschum *et al.*,[48] the positron annihilation lifetime spectrum is decomposed into components related to the fractions of positrons that trap and annihilate in vacancy-type point defects inside spherically shaped grains and in open-volume-type defects at the grain boundaries, respectively, and further into components associated to bulk 'free' positron annihilation in the grains. The positron annihilation lifetime spectra can be written as a sum of exponential decay functions, each characterized by an intensity I_i and lifetime τ_i [48]

$$n(t) = I_v \exp(-t/\tau_v) + I_b \exp(-t/\tau_b) + \sum_{j=1}^{\infty} I_{0,j} \exp(-\lambda_{0,j} t), \quad (6.5)$$

where I_v and τ_v are the annihilation fraction and positron lifetime in the vacancy-type defects inside the grain, I_b and τ_b are the corresponding positron annihilation parameters associated with the open-volume-type defects in the grain boundaries, and further a sequence of decay rates $\lambda_{0,j}$ with associated annihilation fractions $I_{0,j}$, corresponding to a modification of the conventional bulk 'free' positron annihilation induced by the diffusion-limited positron trapping in vacancies and at grain boundaries.

We employed the positron trapping model to simulate the positron annihilation fractions in vacancies inside the grain and in the grain boundaries. In this model,[34] 7 empirical parameters are required, namely r_0 the radius of the grains, D_+ and τ_f, the positron diffusion coefficient and positron lifetime in the bulk of the grain, respectively, σ_v, and τ_v, the positron trapping coefficient and positron lifetime, and finally α and τ_b, the trapping rate at the grain boundaries and positron lifetime of the open-volume defects at the grain boundaries, respectively. The parameters deduced for the studied ZnO layers are listed in Table 6.3. Among these parameters, a grain radius $r_0 = 62 \pm 2\ nm$ for the ZnO:Al layer in the as-deposited CIGS sample and $r_0 = 58 \pm 2\ nm$ after degradation for 1056 h, indicating that the grain size had not changed, was derived from cross-sectional SEM measurements.[34] A positron lifetime of $\tau_{V_{Zn}} = 224 \pm 5\ ps$ for

the monovacancy V_{Zn} inside the grains and a positron lifetime of $\tau_b = 369 \pm 9\ ps$ (top layer) and of $\tau_b = 321 \pm 8\ ps$ (bottom layer) for the vacancy clusters at grain boundaries were obtained from the PALS spectra reported in the previous Section. After degradation, the experimentally extracted positron lifetimes increase significantly. Therefore, in the simulations performed for the comparison with the 1056 h degraded sample, the corresponding experimental lifetimes were included (see Table 6.3).

Table 6.3. Parameters used in the positron trapping model[34,48]

ZnO:Al	Parameter name	Symbols	Parameter value	
			As-deposited	1056-hour degradation
Grain	Positron lifetime V_{Zn}	$\tau_{V_{Zn}}$	224 ps	251 ps (top) 231 ps (bottom)
	Trapping coefficient V_{Zn}	$\sigma_{V_{Zn}}$	$1.7 \cdot 10^3$ ps^{-1} [a,b]	$1.7 \cdot 10^3$ ps^{-1} [a,b]
	Positron diffusion coefficient	D_+	520 nm^{2}ps^{-1} [b]	520 nm^{2}ps^{-1} [b]
	Free positron lifetime	τ_f	161 ps [b]	161 ps [b]
	Grain radius	r_0	62 nm	58 nm
Grain boundary	Trapping rate at the grain boundary	α	1.5 nm ps^{-1} (top) 1 nm ps^{-1} (bottom) [c]	1.5 nm ps^{-1} (top) 1 nm ps^{-1} (bottom) [c]
	Positron lifetime grain boundary	τ_b	369 ps (top) 321 ps (bottom)	428 ps (top) 404 ps (bottom)

[a]Reference 16.
[b]Reference 49.
[c]Reference 50.

Figure 6.10(a) presents the average lifetime in the top and bottom layers of the ZnO in the as-deposited CIGS samples calculated using this model as a function of C_v, the concentration of the vacancy-type defects inside the grain. For small vacancy concentrations (~10^{-6}), most positrons diffuse to the grain boundaries and are trapped there, while a fraction of ~5% also annihilates as bulk 'free' positrons inside the grains. With an increase of C_v, positrons increasingly trap and annihilate at point defects in the grain, leading to a reduction in the average positron lifetime. At large values of C_v, this process becomes dominant and the average lifetime $\bar{\tau}$ approaches $\tau_{V_{Zn}}$.

The experimentally observed average positron lifetime of 247±3 ps for the bottom layer can be used to derive the corresponding concentration of intragranular point defects V_{Zn} of $C_V = 7 \cdot 10^{-5}$, as indicated by the dashed lines in Figure 6.10(a). It is reasonable to assume that the concentration of vacancies for the top layer is about the same as for the bottom layer. Within the positron trapping model, consistency with the observed positron annihilation parameters,

including the average positron lifetime of 271±3 ps for the top layer, is maintained, requiring only a slight increase in the trapping rate of positrons at the grain-boundaries of $\alpha = 1.5\ nm\ ps^{-1}$ in the top layer. Such a higher trapping rate can be understood, since the size of the open volume defects at the grain boundaries is clearly larger in the top layer compared to the bottom layer, and therefore they can act as stronger positron trapping sites.

Also, the positron annihilation fractions are consistently retrieved using the positron trapping model with parameters given in Table 6.3. Figure 6.10(c) shows the calculated positron annihilation fractions in vacancies inside the grains (I_v) and at the grain boundaries (I_b) upon variation of intragranular vacancy concentration C_V for the ZnO:Al film in the as-deposited CIGS samples. Clearly, with increasing intra-granular vacancy concentration C_V , the annihilation fraction in the mono-vacancies I_v increases while I_b decreases for both the top and bottom layer of ZnO:Al layer. Using the extracted concentration of $C_V = 7 \cdot 10^{-5}$ (Figure 6.10(a)), the calculated fractions I_v and I_b are 63% and 35% for the top layer, respectively, while for the bottom layer calculated fractions of I_v and I_b of respectively 71% and 28% are obtained. These positron annihilation fractions in vacancies inside the grains and at the grain boundaries are in a good quantitative agreement with the intensities determined from the experimental PALS spectra of I_v = 64% and I_b = 35%, respectively, for the top layer, and I_v = 74.5% and I_b = 25%, respectively, for the bottom layer of the as-deposited sample. Notably, the model accurately reproduces the larger annihilation fraction at the grain boundaries for the top layer compared to the bottom layer, showing the consistency of the applied positron trapping model.

A similar analysis was performed for the Al-doped ZnO layer for the 1056 h degraded sample. Figure 6.10(b) and (d) presents the corresponding average lifetime and positron annihilation fractions for the top layer and bottom layer as a function of intra-granular vacancy concentration C_V . In the positron trapping model, only the (experimentally determined) values for the positron lifetimes of the vacancies in the grain and of the vacancy clusters at the grain boundaries were changed as input parameters in the calculations (see Table 6.3), which turned out to be sufficient to retrieve consistency with all experimental results from the positron lifetime study. Figure 6.10(b) shows that an intra-granular vacancy concentration of about $C_V = 5 \cdot 10^{-5}$ for both the top and bottom layer of ZnO:Al is now deduced, using the average lifetime $\bar{\tau} = 327 \pm 3 ps$ for the top layer and $\bar{\tau} = 288 \pm 3 ps$ for the bottom layer as obtained from the PALS spectra, indicating that the concentration of vacancies inside the grains remains nearly constant. Figure 6.10(d) presents calculated fractions of I_v and I_b , inferring annihilation fractions of I_v = 52% and I_b = 45%, respectively, for top layer and I_v = 61% and I_b = 37%, respectively, for bottom layer using $C_V = 5 \cdot 10^{-5}$. This shows that the fraction of positrons that trap and annihilate at vacancies inside the grains (I_v) decreases, while annihilation at the grain boundaries (I_b) increases, consistent

with the observed experimental trends given in Figure 6.9(b) for prolonged degradation of ~1000 h and more.

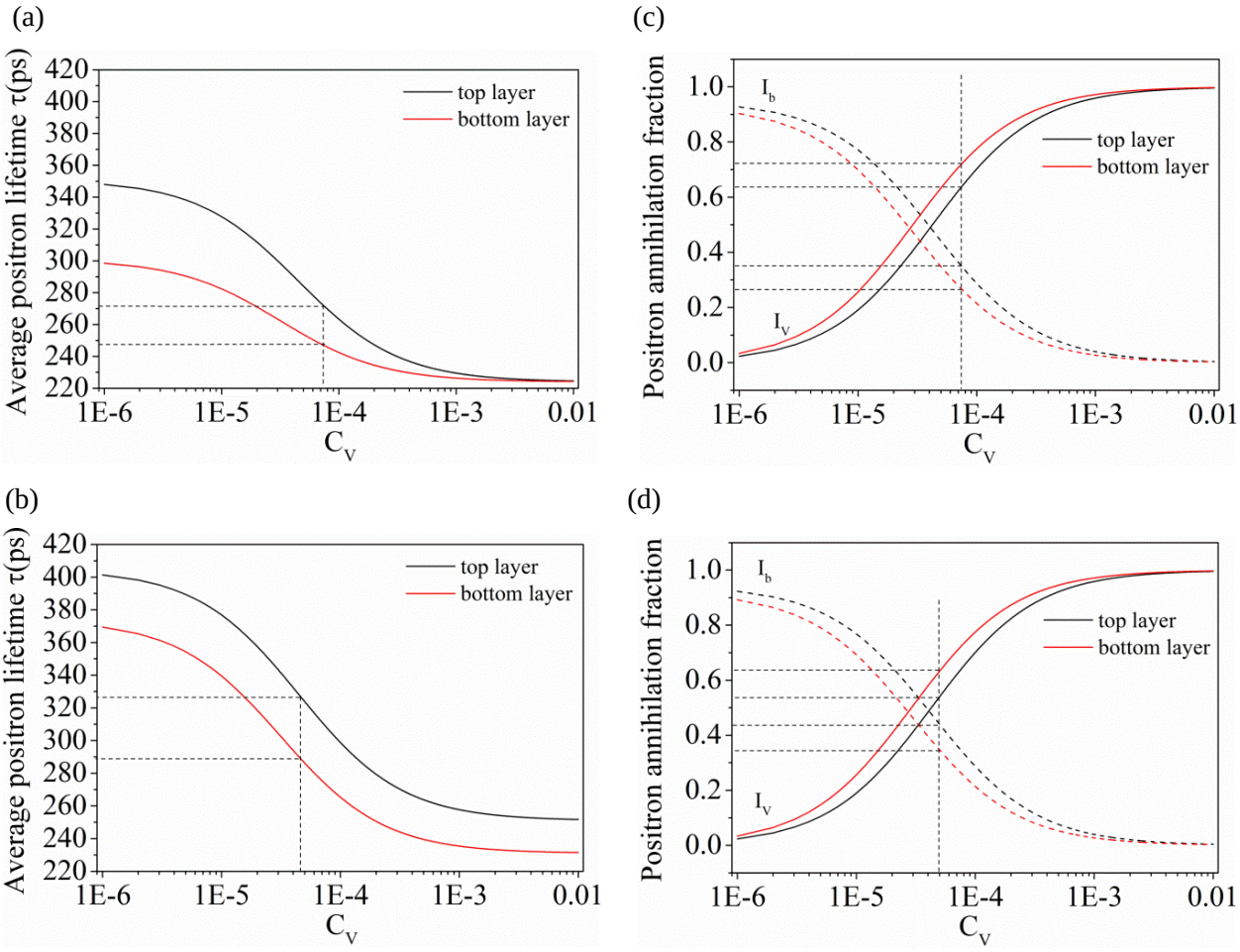

Figure 6.10. (Left) Average positron lifetime as a function of vacancy concentration C_v inside the grains for (a) as-deposited ZnO:Al and (b) 1056-h degraded ZnO:Al films, calculated using the positron-trapping model of Ref. 48 using the parameters given in Table 6.3. Dashed horizontal lines correspond to the measured PALS results. (Right) Calculated positron annihilation fractions in vacancies inside the grains I_v and at the grain boundaries I_b as a function of vacancy concentration C_v for (c) as-deposited ZnO:Al and (d) 1056 h degraded ZnO:Al films.

In conclusion, the positron trapping model consistently shows that most positrons (60%-70%) trap and annihilate in Zn mono-vacancies V_{Zn} inside the grains, while 30%-40% of positrons trap and annihilate in vacancy clusters $(V_{Zn})_m(V_O)_n$ at the grain boundaries, with a higher fraction of positrons annihilating in larger vacancy clusters in the top layer compared to the bottom layer. The model also demonstrates that the fraction of positrons annihilating from a bulk-like 'free' delocalized state is small for all studied samples, consistent with the absence of a short bulk-like lifetime component in the positron annihilation lifetime spectra.

6.3.7. Degradation mechanism

An important factor in the decrease in efficiency of the CIGS solar cell is the deterioration of the ZnO:Al transparent conductive oxide window layer. In this study, a strong increase and corresponding decrease in respectively the S and W parameter of the ZnO:Al layer is observed in the positron annihilation depth profiling experiments, that evolve on a remarkably similar timescale as the decrease in solar cell efficiency. This marks the development of increased open volume defect densities and sizes of the vacancy clusters at the grain boundaries, and possibly also inside the grains, that bears a direct relationship to the degradation of the CIGS solar cells. In contrast, no visible change in S or W parameter of the CIGS layer emerged from the depth-resolved experiments.

In previous studies, the degradation of the ZnO:Al TCO was linked to the formation of $Zn(OH)_2$ and Zn-based carbonates including mixtures of these, i.e. $Zn_x(OH)_y(CO_3)_z$), at the grain boundaries due to the reaction with ZnO of H_2O and CO_2 molecules after diffusion into the layer via the grain boundaries. The present study indicates that the creation of open volume in the ZnO:Al layer also plays an essential role in the degradation. A substantial fraction of positrons is observed to trap and annihilate at the grain boundaries in the ZnO:Al film with grain sizes of ~60 nm. Clearly, a strong increase in the size of the open volume at the grain boundaries is revealed. In addition, part of the positrons trap in V_{Zn} mono-vacancies or in small V_{Zn} vacancy complexes, and a minor increase in their size with degradation is also observed. Two related processes could thus possibly be involved in the degradation of the ZnO:Al layer treated in the damp heat chamber (85 ^{o}C/85% RH).

The first, most important process is related to the grain boundaries of the Al-doped ZnO layer. At the grain boundary, not-fully-passivated zinc, oxygen and aluminum ions will be present. Under the condition of 85 ^{o}C/85% RH, small molecules, like H_2O and carbon dioxide from the environment that diffuse into the grain boundary and contribute to the formation of $Zn(OH)_2$ complexes and Zn-based carbonates from reaction of the ZnO:Al with the water and CO_2 molecules.[8] This means that Zn and O atoms will be locally removed from the ZnO lattice, and vacancies and small vacancy clusters can be formed at the grain boundaries.

Clearly, the time-scale of diffusion extracted from the formation concentration profile of vacancies and vacancy clusters, of the order of $t^* = \frac{d^2}{4D} \sim 560\ h$, is similar to that of the in-diffusion of environmental molecules, extracted from SIMS profiles in previous studies by Theelen[50] and by Hüpkes.[51] Indeed, the diffusion coefficient of $D = 35\ nm^2 / h$ extracted from the positron depth-profiling studies is of same order of magnitude as the one extracted from SIMS profiles of in-diffused deuterium, $D_{D^+} \sim 100\ nm^2 / h$,[51] which arguably is related to in-diffusion via the grain boundaries. Thus, the present study provides further support for the conclusion that in-diffusion of molecular species via grain boundaries is a major cause for

degradation of the ZnO:Al layer. A similar mechanism was also reported for polycrystalline H-doped In_2O_3 (IO:H).[52] Here, pronounced formation of open volume defects at the grain boundaries is observed, directly connected to the occurrence of chemical reactions and formation of $Zn(OH)_2$, Zn-based carbonates and mixtures of these (e.g. $Zn_x(OH)_y(CO_3)_z$), inferred from previous studies. The formed Zn-based compounds together with the increase in open space at the grain boundaries will effectively disturb lateral charge carrier transport through the ZnO:Al TCO layer, by imposing increasingly large transport barriers and reducing charge carrier mobility due to enhanced scattering at the grain boundaries. Moreover, charge carriers could be more effectively trapped and/or suffer from non-radiative recombination at the open space formed at grain boundaries, reducing the charge carrier density. These factors will lead to a strong increase in series resistance (as observed), and correspondingly, a large reduction in Fill Factor and efficiency of the ZnO:Al/i-ZnO/CdS/CIGS/Mo solar cells. In actual modules, ZnO:Al TCO layers with a larger thickness of typically ~1 μm are used, leading to substantially slower, but otherwise similar, degradation of the solar cell Fill Factor.

A second, minor degradation process might occur inside of the grains, related to formation of di-vacancies out of Zn mono-vacancies present inside the grains of the as-deposited ZnO:Al. Namely, it was observed in Ref. 8 and Ref. 51 that H^+ is formed in the films during damp-heat treatment for prolonged degradation times. Especially, H^+ showed high concentrations in the top 100 nm of ZnO:Al films.[8] The formed H^+ may easily enter the grain, where fast in-diffusion via interstitial sites is expected, in view of the very high diffusion coefficient in ZnO of $D_{H_i} \sim 10^7\ nm^2/h$ (at 380 K).[53,54] H^+ may occupy body-centered interstitial sites in ZnO, where it leads to plastic deformation of the ZnO crystal lattice, and the formation of additional Zn mono-vacancies and growth of larger vacancies such as V_{Zn}-V_O inside the grain can therefore be expected.[55,56] Indeed, in the positron lifetime experiment, the corresponding shortest lifetime τ_1 of the top ZnO:Al increases to 256 ± 5 ps during prolonged degradation, indicating that larger vacancies are created. These point defects may also contribute to increased scattering of charge carriers and the observed increase in series resistance of the CIGS solar cell. Nevertheless, this study shows that the in-diffusion of molecules via grain boundaries and the formation of open volume at the grain boundaries form the key (and rate-limiting) factor to the degradation of the ZnO:Al. This is underlined by the observed diffusion coefficient of $D = 35\ nm^2/h$, demonstrating that this rate-limiting step is orders of magnitude slower than interstitial diffusion of H^+ with a diffusion coefficient of $D_{H_i} \sim 10^7\ nm^2/h$, while larger species such as O_2, H_2, H_2O and CO_2 will show negligible diffusion into the ZnO grains.[57]

6.4. Conclusions

The accelerated degradation of Al-doped ZnO TCO layers on top of CIGS solar cells was examined using various positron annihilation techniques. The PALS and Doppler broadening studies indicate that the formation and growth of vacancy clusters at grain boundaries is a key

component of the degradation mechanism of the ZnO:Al/i-ZnO/CdS/CIGS/Mo solar cells. Quantitative information on the sizes of the vacancy clusters and fractions of positrons trapping at the grain boundaries was obtained by detailed comparison of the positron annihilation lifetime results to a positron trapping model developed by Würschum *et al.*.[48] The evolution of open volume at the grain boundaries may contribute substantially to increase transport barriers upon degradation, reducing charge carrier mobility, and may further give rise to increased charge carrier trapping. The formation and growth of open volume at the grain boundaries in the ZnO:Al TCO layer thus forms a major factor to the observed large increase in series resistance and the reduction in solar cell Fill Factor, which is the main cause for the largely reduced solar cell efficiency upon prolonged moisture-heat degradation for solar cells without a costly water protective glass-based packaging.

Positron Doppler depth profiling is shown to be a sensitive method to monitor the depth resolved vacancy generation as a function of degradation time. The positron study establishes a direct correlation between the depth-profiles of the generated vacancy clusters and the previously observed in-diffusion of molecules such as H_2O and CO_2 via the grain boundaries of the ZnO:Al TCO layer, with a convincing match in the characteristic time scale of diffusion and solar cell degradation, providing further evidence for a key role in the degradation. This infers that the reactions of these molecules at the grain boundaries leads to the creation of the observed additional open volume. The formation of H^+ at the grain boundaries might also affect the degradation via a second process, in which H^+ enters and rapidly diffuse into the ZnO:Al grains, where the H^+ ions may cause plastic deformation of the ZnO lattice leading to an increase in size of Zn vacancies. The mechanisms of degradation suggest that synthesis methods should be explored which either lead to a reduced density of grain boundaries or the use an additional suitable barrier layer to prevent infiltration of environmental molecules.

6.5. Appendix A: Diffusion induced changes in positron Doppler Broadening depth profiles

In this Appendix a model is described in order to account for the effect of a diffusion-related depth distribution on positron Doppler broadening depth profiles. To the authors' knowledge, a similar model has not been reported in literature. The diffusion model assumes that the formation of additional open volume is proportional to the concentration of in-diffused molecules, and in turn the created open volume defects lead to a proportional increase ΔS and decrease ΔW . Starting point is the solution for diffusion in a semi-infinite homogenous medium with a constant diffusion coefficient *D*, taking as the boundary condition a constant concentration *C(0)* at the surface, given by[35]

$$C(z) = C(0)erfc(\frac{z}{2\sqrt{Dt}}), \qquad \text{(A6.5.1)}$$

where $C(z)$ is the concentration as a function of depth z below the surface, $erfc(x) = 1 - erf(x)$ is the complementary error function, and t is the degradation time. In order to derive the dependence on positron implantation energy of $\Delta S(E)$ and $\Delta W(E)$, Makhovian distributions for the positron implantation profiles were used, given by

$$P(z,E) = \frac{2}{z_0}\left(\frac{z}{z_0}\right)^{m-1} e^{-(z/z_0)^m}, \tag{A6.5.2}$$

where $z_0 = 1.13 z_{ave}$ with the average positron implantation depth $z_{ave} = \alpha_p E^n/\rho$, ρ is the density of the medium, and E is the positron implantation energy. In the analysis, the parameters $m = 2$, $n = 1.62$, and $\alpha_p = 4.0$ μgcm^{-2}keV$^{-1.62}$ were used,[28,36]

The depth dependence of the concentration of in-diffusion atmospheric species in the diffusion model and the positron stopping profile given by Eqs. (A6.5.1) and (A6.5.2) can be used to derive expressions for the change in S and W parameters as a function of positron implantation energy. If one assumes that the open volume generated is proportional to the concentration of in-diffused atomic and molecular species, and leads to a proportional change in S and W, the change in S parameter, $\Delta S(E)$, and in W parameter, $\Delta W(E)$, at a specific positron implantation energy is given by the integrated product of the concentration depth profile and the Makhovian implantation profile for positron implantation energy E

$$\Delta S(E,t) = I_{\Delta S} \cdot \int_0^\infty C(z) P(z,E) dz, \tag{A6.5.3}$$

$$\Delta W(E,t) = I_{\Delta W} \cdot \int_0^\infty C(z) P(z,E) dz, \tag{A6.5.4}$$

where $I_{\Delta S}$ and $I_{\Delta W}$ are proportionality pre-factors. Diffusion of thermalized positrons is not taking into account in the model. This limits the validity of the model to the case where the positron diffusion length $L_+ << z_0$,[28,37] *i.e.* for films with moderate to high defect concentrations leading to a short positron diffusion length, or to sufficiently high positron implantation energies. Using the expressions for the concentration depth profile Eq. (A6.5.1) and the Makhovian implantation profile Eq. (A6.5.2), the integral in Eqs. (A6.5.3) and (A6.5.4) can be rewritten as follows:

$$\int_0^\infty erfc\left(\frac{z}{2\sqrt{Dt}}\right)\frac{2z}{z_0^2} e^{-(z/z_0)^2} dz = \int_0^\infty \left[1 - erf\left(\frac{z}{2\sqrt{Dt}}\right)\right]\frac{2z}{z_0^2} e^{-(z/z_0)^2} dz$$

$$= \int_0^\infty \frac{2z}{z_0^2} e^{-(z/z_0)^2} dz - \int_0^\infty erf\left(\frac{z}{2\sqrt{Dt}}\right)\frac{2z}{z_0^2} e^{-(z/z_0)^2} dz = 1 - \frac{z_0}{\sqrt{z_0^2 + 4Dt}}, \tag{A6.5.5}$$

where we used the table of integrals reported by Ng and Geller in Ref. 58 to solve for the second integral.

This means that the positron-implantation energy dependent change in *S* and *W* can be described by

$$\Delta S(E) = \Delta S_0 \cdot \left[1 - \frac{z_0}{\sqrt{z_0^2 + 4Dt}} \right] \quad \text{and} \quad \Delta W(E) = \Delta W_0 \cdot \left[1 - \frac{z_0}{\sqrt{z_0^2 + 4Dt}} \right], \tag{A6.5.6}$$

valid for one-dimensional diffusion in a semi-infinite medium. This is also a good approximation for the case of a finite layer with thickness d, provided that the diffusion length $L = \sqrt{Dt} << d$, or, for the case $L = \sqrt{Dt} \sim d$, that the average positron implantation depth $z_{ave} = 1.13 z_0 << d$, *i.e.* for low positron implantation energies. For the case of $L = \sqrt{Dt} \sim d$ or larger (i.e. for long degradation times), the solution of the diffusion problem of a finite slab instead of a semi-infinite planar medium for the concentration profile $C(z)$ needs to be considered.[35] Here, we neglect the corresponding (moderate) changes in the concentration profile $C(z)$ that first primarily occur near the ZnO/CdS interface, since these expectedly will have a minor effect on the Doppler depth-profiles in this study, in view of the broad positron implantation profiles at the high positron energies required to probe the region of the ZnO/CdS interface ($z_0 \sim d$). In the equations, $\Delta S_0 = I_{\Delta S} \cdot C(0)$ and $\Delta W_0 = I_{\Delta W} \cdot C(0)$ are the change in *S* and *W* for annihilation of thermalized positrons inside the ZnO:Al just below the surface, with $I_{\Delta S}$ and $I_{\Delta W}$ intensity proportionality pre-factors connecting ΔS_0 and ΔW_0 with the surface concentration $C(0)$.

In general, an integral over a finite slab extending to $z_{max} = d$ instead of an integration over a semi-infinite system needs to be performed, in order to properly include the behavior of $\Delta S(E)$ and $\Delta W(E)$ at high positron implantation energies. The corresponding integral can be solved numerically, according to

$$\Delta S_{ZnO:Al}(E) = \Delta S_0 \cdot \left[1 - e^{-(d/z_0)^2} - \int_0^d erf\left(\frac{z}{2\sqrt{Dt}}\right) \frac{2z}{z_0^2} e^{-(z/z_0)^2} dz \right] \tag{A6.5.7}$$

and

$$\Delta W_{ZnO:Al}(E) = \Delta W_0 \cdot \left[1 - e^{-(d/z_0)^2} - \int_0^d erf\left(\frac{z}{2\sqrt{Dt}}\right) \frac{2z}{z_0^2} e^{-(z/z_0)^2} dz \right]. \tag{A6.5.8}$$

The cut-off at $z = d$ takes into account that at high positron implantation energies more and more positrons annihilate in the CdS and CIGS layers underneath the ZnO:Al layer,[28,37] and do not probe the degradation-induced changes in the ZnO layer. The model assumes that the CdS and CIGS layers are not affected significantly by the in-diffusion of molecules.

In order to provide the connection to the experimentally observed depth profiles, we start by noting that the depth profiles for the as-deposited sample $S_{AD}(E)$ and $W_{AD}(E)$ can be written as

$$S_{AD}(E) = S_s(t=0)\, f_s(E) + S_{ZnO:Al}(t=0)\, f_1(E) + S_2(t=0)\, f_2(E), \quad \text{(A6.5.9)}$$

$$W_{AD}(E) = W_s(t=0)\, f_s(E) + W_{ZnO:Al}(t=0)\, f_1(E) + W_2(t=0)\, f_2(E), \quad \text{(A6.5.10)}$$

where S_s , $S_{ZnO:Al}$, and S_2 are the S parameter for the surface, the ZnO:Al layer and the CdS/CIGS layer, respectively, and $f_s(E)$, $f_{ZnO:Al}(E)$ and $f_2(E)$ are the positron implantation energy dependent fractions of positrons annihilating at the surface and in the two layers, respectively.

The difference in S and in W parameter, extracted from the experimentally observed depth profiles of the degraded ZnO:Al layer relative to that of the as-deposited solar cell, is defined by

$$\Delta S_{\exp}(E,t) = S_{\exp}(E,t) - S_{AD}(E), \quad \text{(A6.5.11)}$$

$$\Delta W_{\exp}(E,t) = W_{\exp}(E,t) - W_{AD}(E), \quad \text{(A6.5.12)}$$

and is in general caused by both the depth-dependent changes in the ZnO layer and at the surface. The latter is described by degradation-time-dependent surface annihilation parameters $S_s(t)$ and $W_s(t)$. In order to separate both contributions, we assume that the surface annihilation fraction $f_s(E)$ does not change upon degradation, *i.e.* back diffusion and surface trapping of positrons as well as annihilation of epithermal positrons remain unaffected by the degradation. In that case, one can subtract the factor $\Delta S_s f_s(E)$ and $\Delta W_s f_s(E)$ from Eqs. (A6.5.11) and (A6.5.12) to retrieve the net change in S and W related to positron annihilation in the ZnO:Al layer .

Subsequently, the experimental results can finally be compared to the in-diffusion model given by Eqs. (A6.5.7) and (A6.5.8), according to

$$\Delta S_{ZnO:Al}(E,t)(1 - f_s(E)) = \Delta S_{\exp}(E,t) - \Delta S_s(t)\, f_s(E), \quad \text{(A6.5.13)}$$

$$\Delta W_{ZnO:Al}(E,t)(1 - f_s(E)) = \Delta W_{\exp}(E,t) - \Delta W_s(t)\, f_s(E), \quad \text{(A6.5.14)}$$

in which the factor $1 - f_s(E)$ accounts for the reduction in positron annihilation fraction in the ZnO:Al layer in the low-energy range, since upon implantation at shallow depths, surface annihilation becomes a dominant factor. Eqs. (A6.5.13) and (A6.5.14) are used to compare the experimental depth profiles with theoretical curves obtained from the diffusion model.

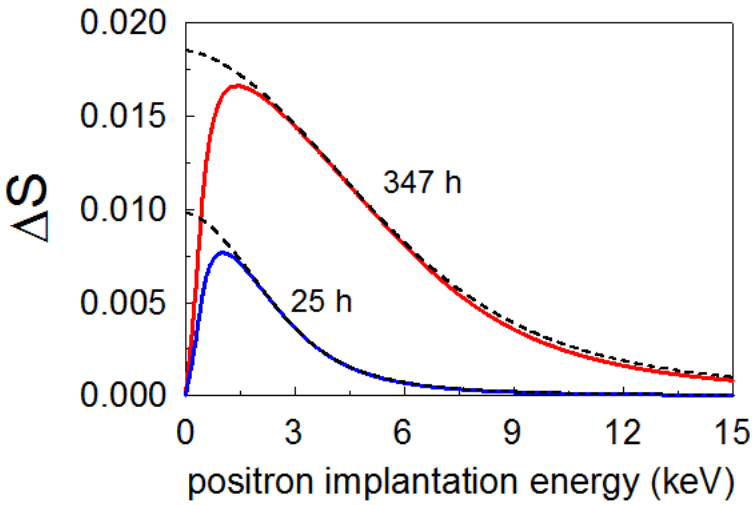

Figure A6.5.1. $\Delta S(E)(1-f_s(E))$ curves for 25 h and 347 h of degradation obtained using VEPFIT (full lines, model #1, see text) and $\Delta S(E) = \Delta S_0 \cdot (1 - \frac{z_0}{\sqrt{z_0^2 + 4Dt}})$ (dashed lines) for a semi-infinite ZnO medium, with $D = 35\ nm^2 / h$.

For completeness we demonstrate in Figure A6.5.1 that the diffusion analysis can also be incorporated into VEPFIT. Two simulations of the in-diffusion for degradation times of 25 h and 347 h, respectively, by VEPFIT are shown, using S parameter depth profiles $\Delta S(z) = \Delta S_0 \cdot (1 - erf(\frac{z}{2\sqrt{Dt}}))$ as input to the model #1 option of VEPFIT,[28] with a diffusion coefficient of $D = 35\ nm^2 / h$ as input parameter. The VEPFIT curves are based on a 22-point discrete $\Delta S_i(z_i)$ depth profile for the ZnO layer and a short positron diffusion length of 2 nm to satisfy the assumption of $L_+ << z_0$. In the Figure, also the curves obtained from the analytical case of an in-diffusion model with $L_+ << z_0$ for a semi-infinite medium, corresponding to $\Delta S(E) = \Delta S_0 \cdot (1 - \frac{z_0}{\sqrt{z_0^2 + 4Dt}})$ given in Eq. (A6.5.6). For short in-diffusion times, a close agreement is obtained, while for a diffusion time of 347 h, the VEPFIT curve is slightly lower than the curve for this analytical model for a semi-infinite medium at high positron implantation energies, reflecting the finite thickness of the ZnO layer. The agreement supports the reliability of the in-diffusion model analysis based on Eqs. (A6.5.7) and (A6.5.8). Furthermore, it shows that in principle positron diffusion can also be included as a refinement of the analysis by subsequent VEPFIT analysis for cases where $L_+ << z_0$ is not satisfied.

References

[1] Christian Roselund, *ZSW sets new thin film solar world record with 22.6% efficient CIGS PV cell*, PV Magazine **6** (2016). https://www.pv-magazine.com/2016/06/15/zsw-sets-new-thin-film-solar-world-record-with-22-6-efficient-cigs-pv-cell_100024995/

[2] P. Jackson, D. Hariskos, R. Wuerz, O. Kiowski, A. Bauer, T.M. Friedlmeier, and M. Powalla, Phys. Stat. Solidi - RRL **9**, 28 (2015).

[3] P. Xin, J.K. Larsen, F. Deng, and W.N. Shafarman, Sol. Energy Mater. Sol. Cells **157**, 85 (2016).

[4] D. Jordan, and S. Kurtz, Proc. 37th IEEE PVSC, 827 (2011).

[5] J. del Cueto, S. Rummel, B. Kroposki, C. Osterwald, and A. Anderberg, Proc. 33rd IEEE PVSC, 1 (2008).

[6] C. Radue, and E. van Dyk, Physica B **404**, 4449 (2009).

[7] M. Theelen, and F. Daume, Sol. Energy **133**, 586 (2016).

[8] M. Theelen, T. Boumans, F. Stegeman, F. Colberts, A. Illiberi, J. van Berkum, N. Barreau, Z. Vroon, and M. Zeman, Thin Solid Films **550**, 530 (2014).

[9] D.-K. Kim and H. B. Kim, Curr. Appl. Phys. **13**, 2001 (2013).

[10] M. Hafemeister, S. Siebentritt, J. Albert, M.Ch. Lux-Steiner, S. Sadewasser, Phys. Rev. Lett. **104**, 196602 (2010).

[11] D. Abou-Ras, B. Schaffer, M. Schaffer, S.S. Schmidt, R. Caballero, Th. Unold, Phys. Rev. Lett. **108**, 075502 (2012).

[12] A. Chirilă, P. Reinhard, F. Pianezzi, P. Bloesch, A.R. Uhl, C. Fella, L. Kranz, D. Keller, C. Gretener, H. Hagendorfer, D. Jaeger, R. Erni, S. Nishiwaki, S. Buecheler, and A.N. Tiwari, Nature Mater. **12**, 1107 (2013).

[13] M. Theelen, R. Hendrikx, N. Barreau, H. Steijvers, and A. Böttger, Solar Energy Materials and Solar Cells **157**, 943 (2016).

[14] S.W.H. Eijt, H. Leegwater, H. Schut, A. Anastasopol, W. Egger, L. Ravelli, C. Hugenschmidt, and B. Dam, J. All. Compd. **509**, S567 (2011).

[15] F. Tuomisto, and I. Makkonen, Rev. Mod. Phys. **85**, 1583 (2013).

[16] R. Krause-Rehberg, and H. Leipner, *Positron Annihilation in Semiconductors - Defect Studies*, (Springer Verlag, Berlin, 1999).

[17] Z. Q. Chen, M. Maekawa, S. Yamamoto, A. Kawasuso, X. L. Yuan, T. Sekiguchi, R. Suzuki, and T. Ohdaira, Phys. Rev. B **69**, 035210 (2004).

[18] D. Scorticati, A. Illiberi, T.C. Bor, S.W.H. Eijt, H. Schut, G.R.B.E. Römer, M. Klein Gunnewiek, A.T.M. Lenferink, B.J. Kniknie, R. Mary Joy, M.S. Dorenkamper, D.F. de Lange, C. Otto, D. Borsa, W.J. Soppe, and A.J. Huis in 't Veld, Acta Mater. **98**, 327 (2015).

[19] C.G. Van de Walle, Phys. Rev. Lett. **85**, 1012 (2000).

[20] J. Čížek, J. Valenta, P. Hruška, O. Melikhova, I. Procházka, M. Novotný, and J. Bulíř, Appl. Phys. Lett. **106**, 251902 (2015).

[21] E.H. Kahn, M.H. Weber, and M.D. McCluskey, Phys. Rev. Lett. **111**, 017401 (2013).

[22] F. Tuomisto, V. Ranki, K. Saarinen, and D.C. Look, Phys. Rev. Lett. **91**, 205502 (2003).

[23] G. Brauer, W. Anwand, D. Grambole, J. Grenzer, W. Skorupa, J. Čížek, J. Kuriplach, I. Procházka, C.C. Ling, C. K. So, D. Schulz, and D. Klimm, Phys. Rev. B **79**, 115212 (2009).

[24] F.A. Selim, M.H. Weber, D. Solodovnikov, and K.G. Lynn, Phys. Rev. Lett. **99**, 085502 (2007).

[25] F. Couzinie-Devy, E. Cadel, N. Barreau, L. Arzel, and P. Pareige, Appl. Phys. Lett. **99**, 232108 (2011).

[26] M. Theelen, N. Barreau, F. Daume, H. Steijvers, V. Hans, A. Liakopoulou, Z. Vroon, and M. Zeman, Proc. SPIE **9179**, 91790I (2014).
[27] L. Chai, MSc dissertation, Delft University of Technology (2010).
[28] A. van Veen, H. Schut, J. de Vries, R.A. Hakvoort, and M.R. IJpma, AIP Conf. Proc. **218**, 171 (1991).
[29] P. Schultz, and K.G. Lynn, Rev. Mod. Phys. **60**, 701 (1988).
[30] C.V. Falub, S.W.H. Eijt, P.E. Mijnarends, A. van Veen, and H. Schut, Nucl. Instr. Meth. A 488, 478 (2002).
[31] P. Sperr, W. Egger W. Kögel, G. Dollinger, C. Hugenschmidt, R. Repper, and C. Piochacz, Appl. Surf. Sci. 255, 35 (2008).
[32] C. Hugenschmidt, B. Löwe, J. Mayer, C. Piochacz, P. Pikart, R. Repper, M. Stadlbauer, and K. Schreckenbach, Nucl. Instr. Meth. A 593, 616 (2008).
[33] D. Giebel and J. Kansy, Mater. Sci. Forum **666**, 138 (2010).
[34] See Supplemental Material in Section 6.6 for the positron annihilation characterization of the two ZnO single crystals, two alternative models for the S parameter depth profiles, the details of the positron trapping model with intragranular vacancies and grain boundary trapping, and SEM analysis of as-deposited and degraded samples.
[35] The Mathematics of Diffusion, J. Crank (Oxford University Press, Oxford, 2nd Edition, 1979).
[36] A. Vehanen, K. Saarinen, P. Hautojärvi, and H. Huomo, Phys. Rev. B **35**, 4606 (1987).
[37] A. Zubiaga, J.A. García, F. Plazaola, F. Tuomisto, J. Zúñiga-Pérez, and V. Muñoz-Sanjosé, Phys. Rev. B **75**, 205303 (2007).
[38] A. Zubiaga, F. Tuomisto, V. Coleman, H. Tan, C. Jagadish, K. Koike, S. Sasa, M. Inoue, and M. Yano, Phys. Rev. B **78** 035125 (2008).
[39] M.H. Weber, F.A. Selim, D. Solodovnikov, and K.G. Lynn, Appl. Surf. Sci. **255**, 68 (2008).
[40] F. Lukáč, J. Čížek, I. Procházka, O. Melikhova, W. Anwand, and G. Brauer, Acta. Phys. Pol. A **125**, 748 (2014).
[41] I. Makkonen, E. Korhonen, V. Prozheeva, and F. Tuomisto, J. Phys. Condens. Matter. **28**, 224002 (2016).
[42] K.M. Johansen, A. Zubiaga, I. Makkonen, F. Tuomisto, P.T. Neuvonen, K.E. Knutsen, E.V. Monakhov, A.Y. Kuznetsov, and B.G. Svensson, Phys. Rev. B **83**, 245208 (2011).
[43] A. Karbowski, K. Fedus, J. Patyk, Ł. Bujak, K. Służewski, and G. Karwasz, Nukleonika **58**, 189 (2013).
[44] S. Lany and A. Zunger, Phys. Rev. Lett. **98**, 045501 (2007).
[45] D.C. Look, in *Zinc Oxide Bulk, Thin Films and Nanostructures*, edited by C. Jagadish and S.J. Pearton (Elsevier, Amsterdam, 2006), p. 37.
[46] H.S. Domingos, J.M. Carlsson, P.D. Bristowe, and B. Hellsing, Interface Sci. **12**, 227 (2004).
[47] R. Ono, T. Togimitsu, and W. Sato, J. Radioanal. Nucl. Chem. **303**, 1223 (2014).
[48] B. Oberdorfer and R. Würschum, Phys. Rev. B **79**, 184103 (2009).
[49] S.Brunner, W. Puff, A.G. Balogh, and P. Mascher, Mater. Sci. Forum **363-365**, 141 (2001).
[50] A. Dupasquier, R. Romero, and A. Somoza, Phys. Rev. B **48**, 9235 (1993).
[51] M. Theelen, K. Polman, M. Tomassini, N. Barreau, H. Steijvers, J. van Berkum, Z. Vroon, and M. Zeman, Surf. Coat. Tech. **252**, 157 (2014).
[52] J. Hüpkes, J. I. Owen, M. Wimmer, F. Ruske, D. Greiner, R. Klenk, U. Zastrow, and J. Hotovy, Thin Solid Films **555**, 48 (2014).

[53] T. Tohsophon, A. Dabirian, S. de Wolf, M. Morales-Masis, and C. Ballif, APL Mater. **3**, 116105 (2015).
[54] N.H. Nickel, Phys. Rev. B **73**, 195204 (2006).
[55] K. Ip, M.E. Overberg, Y.W. Heo, D.P. Norton, S.J. Pearton, C.E. Stutz, S.O. Kucheyev, C. Jagadish, J.S. Williams, B. Luo, F. Ren, D.C. Look, and J.M. Zavada, Solid-State Electron. **47**, 2255 (2003).
[56] J. Čížek, F. Lukáč, M. Vlček, M. Vlach, I. Procházka, F. Traeger, D. Rogalla, H. W. Becker, W. Anwand, G. Brauer, S. Wagner, H. Uchida, A. Pundt, and C. Bähtz,, Def. Diff. Forum **333**, 39 (2013).
[57] J. Čížek, N. Zaludova, M. Vlach, S. Danis, J. Kuriplach, I. Prochazka, G. Brauer, W. Anwand, D. Grambole, W. Skorupa, R. Gemma, R. Kirchheim, and A. Pundt, J. Appl. Phys. **103**, 053508 (2008).
[58] W. Beyer, J. Hüpkes, and H. Stiebig, Thin Solid Films **516**, 147 (2007).
[59] M. Geller and E. W. Ng, J. Res. Nat. Bur. Std. **71**, 191 (1969).
[60] F. Linez, I. Makkonen, and F. Tumisto, Phys. Rev, B **94**, 014103 (2016).
[61] K. M. Johansen, F. Tuomisto, I. Makkonen, and L. Vines, Mater. Sci Semicond. Proc. **69**, 23 (2017)

6.6. Supplemental Material

6.6.1. Positron annihilation characterization of two ZnO single crystals

Figure S6.6.1 presents the measured Doppler broadening S parameter as a function of the positron energy for two hydrothermally (HT) grown ZnO single crystals, c-ZnO #1 and c-ZnO #2 (Mateck GmbH). At low energies, a large fraction of epithermal positrons diffuses back to the surface and is reemitted as epithermal positronium, which contributes to the high values of the S parameter. As the positron energy increases, the fraction of positron annihilation at the surface decreases continuously. The S(E) curve is fitted by VEPFIT program.[1] A mean positron diffusion length of 131 nm is obtained for c-ZnO #1 from the VEPFIT analysis, which is shorter than the theoretically estimated value of 280 nm for defect-free crystalline ZnO,[2] revealing that the c-ZnO contains positron-trapping defects. The second HT grown ZnO (c-ZnO #2) from Mateck GmbH was also examined by Doppler broadening depth profiling. The diffusion length extracted from VEPFIT analysis is 42 nm, which is comparable to the typical values of 40-60 nm for ZnO single crystals measured by several research groups.[2-4] The S parameter of 0.4614±0.0002 of the second ZnO single crystal is lower than that of the first ZnO single crystal (S=0.4641±0.0002), indicating that the second c-ZnO single crystal contains less positron-trapping defects. The long diffusion length in the first c-ZnO single crystal is therefore probably not attributable to a lower concentration of positron traps, but can be caused by the presence of an internal electric field of the polar ZnO, drifting positrons implanted relatively deep inside the c-ZnO back towards the surface.

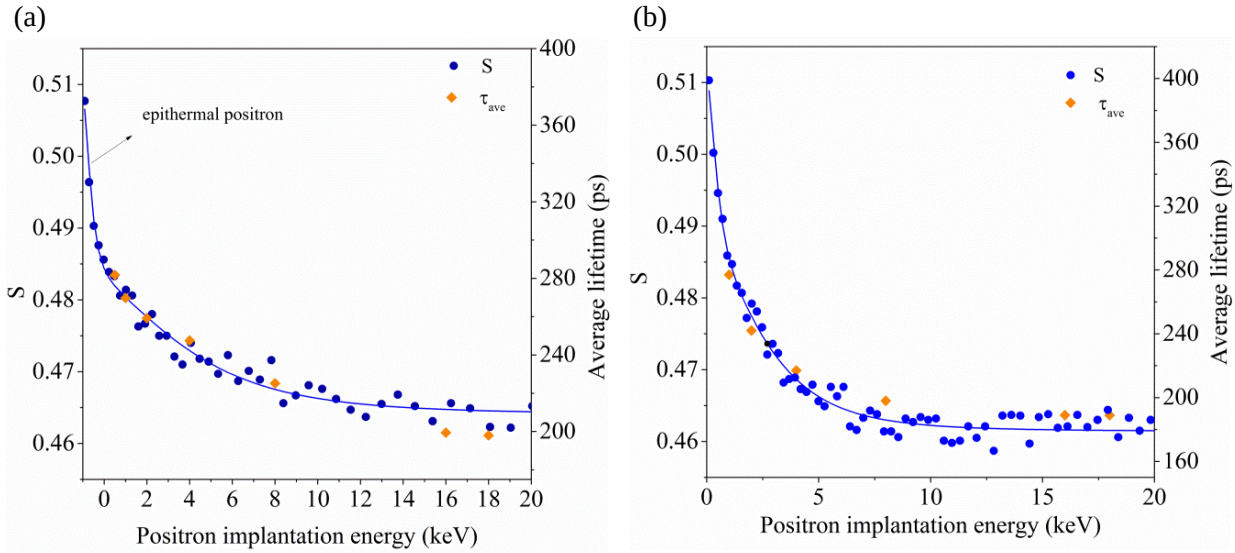

Figure S6.6.1. Dependence of S parameter (dark filled circles) and average positron lifetime (orange filled diamonds) on positron implantation energy for the HT grown ZnO single crystals (a) c-ZnO #1 (MaTeck) and (b) c-ZnO #2 (MaTeck). The S parameter depth profile is fitted by VEPFIT program (blue curve).

In order to further examine the quality of the first ZnO single crystals c-ZnO #1 and c-ZnO #2, we also collected positron annihilation lifetime spectra for the ZnO single crystals as a function

of positron implantation energy. The PALS spectra of c-ZnO #1 at 16 keV shown in Figure S6.6.2 was fitted with three lifetime components using the LT program, with the best-fit parameters listed in table 6.6.1. The average positron lifetime as a function of positron implantation energy is presented in Figure S6.6.1 by the orange solid squares. The average positron lifetime follows a very similar dependence on positron implantation energy as the Doppler broadening S parameter. The bulk lifetime of c-ZnO is determined as 188 ± 3 ps with the intensity of 95.5% at a positron implantation energy of 16 keV. The second ZnO single crystal, c-ZnO #2, showed a similar bulk lifetime of 186 ± 3 ps with the intensity of 99.6% at a positron implantation energy of 16 keV. These lifetimes are in the range of values of 183-189 ps for HT grown ZnO single crystals reported by Chen *et al.*.[5,6] This positron lifetime is longer than typical values reported for defect-free c-ZnO of 160-170 ps grown by other synthesis methods, and might be related to the presence of Li_{Zn}^{-} and/or $V_{Zn}:H$ point defects, that were reported as positron trapping defects in HT grown c-ZnO in previous studies.[2,7,8] Single-Trapping Model (STM)[9] analysis of the positron lifetime spectrum at 16 keV, involving single defect annihilation and defect-free bulk annihilation, showed that the reduced bulk lifetime is at most 15 ps (*i.e.* too small to be resolved) with a contribution of less than 1%, confirming saturation trapping at point defects. At low energies, only annihilation at point defects and surface annihilation contributed to the positron lifetime spectra.

The concentration of hydrogenated Zn mono-vacancy defects can be estimated from the Doppler depth profile using the Single Trapping Model (STM), following

$$C_V = \frac{1}{\sigma_V \tau_f}\left(\frac{L_{+,f}^2}{L_+^2} - 1\right), \qquad \text{(S6.6.1)}$$

in which the positron trapping rate is $\sigma_V = 1.7 \cdot 10^{15} s^{-1}$ (a typical value for a doubly charged negative vacancy).[9] For the defect-free sample, $\tau_f = 154 ps$ the lowest reported experimental (single component) bulk positron lifetime[10] and theoretical $L_{+,f} = 280\ nm$ as positron diffusion length is used.[2] For the reduced positron diffusion length due to defect trapping $L_+ = 42\ nm$ observed for the second ZnO single crystal is taken. According to Eq. (S6.6.1), the corresponding $V_{Zn}:H$ defect concentration is $C_V = 1.7 \cdot 10^{-4}$ ($1.4 \cdot 10^{19}\ cm^{-3}$). A corresponding fraction of 98% of the positrons will annihilated in the $V_{Zn}:H$ defects as estimated using the STM, following

$$f_{defect} = \left(\left(\frac{L_{+,f}}{L_+}\right)^2 - 1\right) / \left(\frac{L_{+,f}}{L_+}\right)^2, \qquad \text{(S6.6.2)}$$

consistent with the absence of a short, defect-free bulk-like component.

We use the value of (S,W) = (0.4641, 0.0889) determined for the first ZnO single crystal c-ZnO #1 by VEPFIT analysis as a reference in the Doppler broadening measurements.

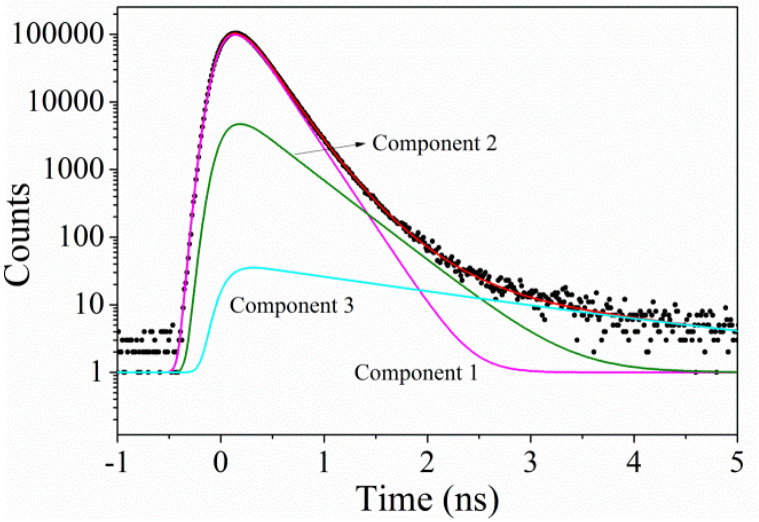

Figure S6.6.2. Three-lifetime-component LT analysis of the positron lifetime spectrum of the ZnO single crystal c-ZnO #1 collected at a positron implantation energy of 16 keV.

Table S6.6.1. Best-fit parameters obtained by LT analysis of the positron lifetime spectrum collected at a positron implantation energy of 16 keV for the ZnO single crystal c-ZnO #1.

Component	τ (ps)	I (%)
1	188±3	95.5
2	389±5	4.3
3	1.9×10^{3}	0.2

6.6.2 Two alternative models for the positron depth-profiles

In this section, we examined whether the changes observed in the Doppler S and W depth profiles can be attributed to primarily the changes at the surface of the sample under exposure of enhanced humidity and temperature conditions (85% relative humidity / 85 ^{o}C). We applied two alternative models that, in contrast to the two-layer model described in Sec. 6.3.2 and the in-diffusion model described in Sec. 6.3.3, only take surface annihilation and positron annihilation in a homogeneous ZnO:Al layer into account. These alternative models fail to provide either (1) a satisfactory fit of the Doppler depth profiles, or (2) lead to an evolution in the fit parameters that cannot be reconciled with the evolution of defects in the ZnO:Al upon accelerated degradation.

Model S1

Model S1 assumes that the surface (and its S parameter) is affected by the accelerated degradation, and the positron diffusion length in the near-surface region, that describes the positron back-diffusion to the surface of the sample, can also be affected. Further, homogeneous

layers are assumed, including a single ZnO:Al layer that is described by the same S parameter as for the as-deposited sample. The layer thickness of the ZnO:Al is a further fit parameter. Figure S6.6.3 shows the curves obtained from a best-fit analysis using VEPFIT, in comparison with the experimental $S(E)$ depth-profiles. In Table S6.6.2, the best-fit parameters are given.

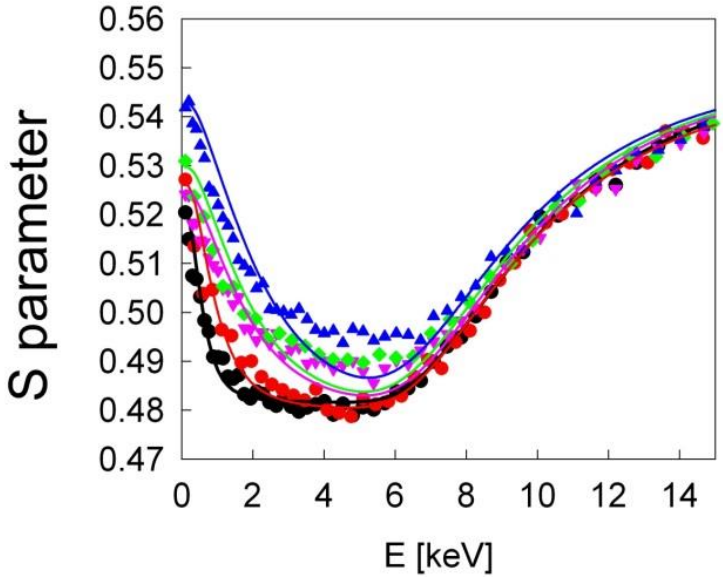

Figure S6.6.3. VEPFIT analysis of the S-parameter depth-profiles assuming that only the surface $S_{surface}$ parameter and the positron diffusion length in the near-surface region change upon accelerated degradation (● - as-deposited, ● - 25 h, ▼-150 h, ♦ - 347 h, # -683 h of accelerated degradation).

Figure S6.6.3 demonstrates that this model clearly fails to provide a good description of the experimental depth-profiles for degradation times of 150 h to 683 h.

Table S6.6.2. VEPFIT analysis best-fit parameters for model S1

Degradation time (h)	$S_{surface}$	$S_{ZnO:Al}$	L_+ (nm)	Layer width (nm)
0	0.522	0.4800 (fixed)	2	257
25	0.527	0.4800 (fixed)	6	256
150	0.525	0.4800 (fixed)	18	266
347	0.530	0.4800 (fixed)	19	260
683	0.543	0.4800 (fixed)	24	259

Model S2

Model S2, similar to model S1, assumes that the surface and the positron diffusion length in the near-surface region, that describes the positron back-diffusion to the surface, is affected by the accelerated degradation. Furthermore, the ZnO:Al, that is assumed to be homogeneous, can be affected by the acceleration degradation, and the S parameter for the single ZnO:Al layer is used as fit variable. We kept the layer thickness of the ZnO:Al fixed to the values obtained in the

two-layer model described in Section 6.3.2. Figure S6.6.4 shows the curves obtained from a best-fit analysis using VEPFIT, in comparison with the experimental $S(E)$ depth-profiles. In Table S6.6.3, the parameters for surface annihilation and annihilation in the ZnO:Al layer are given.

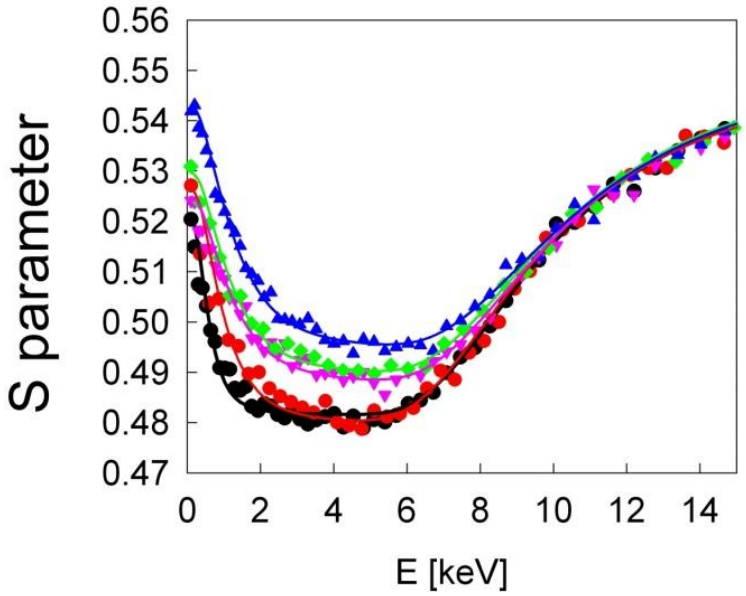

Figure S6.6.4. VEPFIT analysis of the S-parameter depth-profiles assuming that the surface $S_{surface}$ parameter, the positron diffusion length in the near-surface region and the $S_{ZnO:Al}$ of a homogeneous ZnO:Al layer change upon accelerated degradation (● - as-deposited, ● - 25 h, ▼-150 h, ♦ - 347 h, # - 683 h of accelerated degradation).

Clearly, model S2 describes the experimental data much better than model S1. Also, the fits are of a similar quality as for the two-model model (with top and bottom ZnO:Al layer) described in Sec. III.B. However, the positron diffusion length in the near-surface layer, that describes back-diffusion of positrons to the surface of the sample, increases with degradation time. This is clearly against expectations for a material that degrades in time, *i.e.* in which the amount of open volume defects will increase in time. This increase would lead to enhanced positron trapping in defects, and would correspondingly give result in a shorter diffusion length for back-diffusion of positrons to the surface of the sample. Furthermore, in this model, a homogeneous ZnO:Al layer accounts for the largest part of the change in S parameter in the range of 2-5 keV, rather than the changes at the surface of the sample. Namely, in this model, the variation in S-parameter at the surface contributes at 5 keV by at most 1% for all degradation times, and at most 20% at 2 keV for degradation times in the range of 150 – 683 h (and much less at smaller degradation times). This confirms that the variation in S parameter in the range of 2-5 keV is determined by degradation of the ZnO:Al layer well below the surface.

Table S6.6.3. VEPFIT analysis best-fit parameters for model S2

Degradation time (h)	$S_{surface}$	$S_{ZnO:Al}$	L_+ (nm)	Layer width (nm)
0	0.522	0.4800±0.0003	2	257 (fixed)
25	0.527	0.4798±0.0003	6	259 (fixed)
150	0.525	0.4878±0.0003	9	280 (fixed)
347	0.530	0.4895±0.0003	9	280 (fixed)
683	0.543	0.4947±0.0003	10	323 (fixed)

6.6.3. Positron trapping model with intra-granular vacancies and grain boundary trapping

In the grain boundary positron trapping model presented by Würschum *et al.*,[11] the positron lifetime spectrum is decomposed into components related to the fractions of positrons that trap and annihilate in vacancy-type point defects inside spherically shaped grains and in open-volume-type defects at the grain boundaries, respectively, and further into components associated to bulk 'free' positron annihilation in the grains. For completeness, we reproduce here the main parts of the specific model applied. The positron lifetime spectra can be written as[11]

$$n(t) = I_{\mathrm{v}} \exp(-t/\tau_{\mathrm{v}}) + I_b \exp(-t/\tau_b) + \sum_{j=1}^{\infty} I_{0,j} \exp(-\lambda_{0,j} t), \tag{S6.6.3}$$

where I_{v} and τ_{v} are the annihilation fraction and positron lifetime in the vacancy-type defects inside the grain, I_b and τ_b are the corresponding positron annihilation parameters associated with the open-volume-type defects in the grain boundaries, and further a sequence of decay rates $\lambda_{0,j}$ with associated annihilation fractions $I_{0,j}$, corresponding to a modification of the conventional bulk 'free' positron annihilation induced by the diffusion-limited positron trapping in vacancies and at grain boundaries. For the case of spherical grains, the annihilation fractions in vacancies inside the grain I_{v} and in the grain boundaries I_b can be written as[11]

$$I_{\mathrm{v}} = \sigma_{\mathrm{v}} C_{\mathrm{v}} \frac{\left[\alpha + \gamma_{\mathrm{v}} DL(\gamma_{\mathrm{v}} r_0)\right](\tau_f^{-1} + \sigma_{\mathrm{v}} C_{\mathrm{v}} - \tau_{\mathrm{v}}^{-1}) - \dfrac{3\alpha}{r_0}\gamma_{\mathrm{v}} DL(\gamma_{\mathrm{v}} r_0)}{\left[\alpha + \gamma_{\mathrm{v}} DL(\gamma_{\mathrm{v}} r_0)\right](\tau_f^{-1} + \sigma_{\mathrm{v}} C_{\mathrm{v}} - \tau_{\mathrm{v}}^{-1})^2}, \tag{S6.6.4}$$

$$I_b = \frac{\dfrac{3\alpha}{r_0}\gamma_b DL(\gamma_b r_0)}{\left[\alpha + \gamma_b DL(\gamma_b r_0)\right](\tau_f^{-1} + \sigma_{\mathrm{v}} C_{\mathrm{v}} - \tau_b^{-1})}, \tag{S6.6.5}$$

and the sum of bulk-like annihilation fractions naturally satisfies $\sum_{j=1}^{\infty} I_{0,j} = 1 - I_{\mathrm{v}} - I_b$.

In these equations the parameters γ_{v} and γ_b are given by[11]

$$\gamma_{\mathrm{v}}^2 = \frac{\tau_f^{-1} + \sigma_{\mathrm{v}} C_{\mathrm{v}} - \tau_{\mathrm{v}}^{-1}}{D} \quad \text{and} \quad \gamma_b^2 = \frac{\tau_f^{-1} + \sigma_{\mathrm{v}} C_{\mathrm{v}} - \tau_b^{-1}}{D} \tag{S6.6.6}$$

and $L(z)$ is the Langevin function $L(z) = \coth(z) - \frac{1}{z}$.

Further, r_0 is the radius of the grains, and D and τ_f are the positron diffusion coefficient and positron lifetime in the bulk of the grain, respectively; σ_{v}, τ_{v} and C_{v} are the positron trapping coefficient, positron lifetime and concentration of the vacancy-type defects inside the grain; finally α and τ_b are the trapping rate at the grain boundaries and positron lifetime of the open-volume defects at the grain boundaries, respectively.

The mean positron lifetime in this model is given by[11]

$$\bar{\tau} = \frac{\frac{3\alpha}{r_0}\gamma_0 DL(\gamma_0 r_0)\left[\tau_b(\tau_f^{-1} + \sigma_{\mathrm{v}} C_{\mathrm{v}}) - (1 + \sigma_{\mathrm{v}} C_{\mathrm{v}} \tau_{\mathrm{v}})\right] + \left[\alpha + \gamma_0 DL(\gamma_0 r_0)\right](\tau_f^{-1} + \sigma_{\mathrm{v}} C_{\mathrm{v}})(1 + \sigma_{\mathrm{v}} C_{\mathrm{v}} \tau_{\mathrm{v}})}{\left[\alpha + \gamma_0 DL(\gamma_0 r_0)\right](\tau_f^{-1} + \sigma_{\mathrm{v}} C_{\mathrm{v}})^2}, \tag{S6.6.7}$$

with

$$\gamma_0^2 = \frac{\tau_f^{-1} + \sigma_{\mathrm{v}} C_{\mathrm{v}}}{D}. \tag{S6.6.8}$$

6.6.4 SEM analysis of as-deposited and degraded samples

The morphology and average grain size of two ZnO:Al films was determined by SEM. In Figures S6.6.5 and S6.6.6, the top layer is the ZnO:Al TCO (and i-ZnO) film, below which the CdS and CIGS layers are visible. The SEM images show that the grains of the ZnO:Al film consist of very closely stacked pillars, extending throughout the film thickness. The average lateral sizes of the grains in the ZnO:Al film are 62±2 nm for the as-deposited CIGS sample and 58±2 nm for the CIGS sample after 1056-h of DH degradation at 85°C/85% RH. This indicates that the average grain size has not changed during degradation. The thicknesses of the ZnO:Al films are in the range of 260 nm to 280 nm (including the i-ZnO layer) for both the as-deposited and degraded samples, consistent with the thicknesses deduced from the positron Doppler depth profiles.

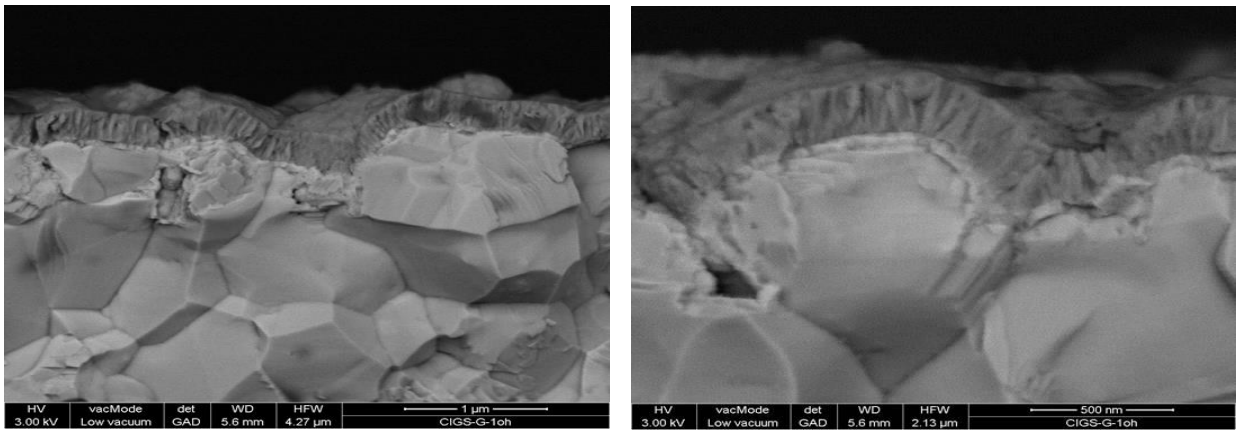

Figure S6.6.5. SEM images of cross-sections of the as-deposited ZnO:Al films on top of CdS/CIGS

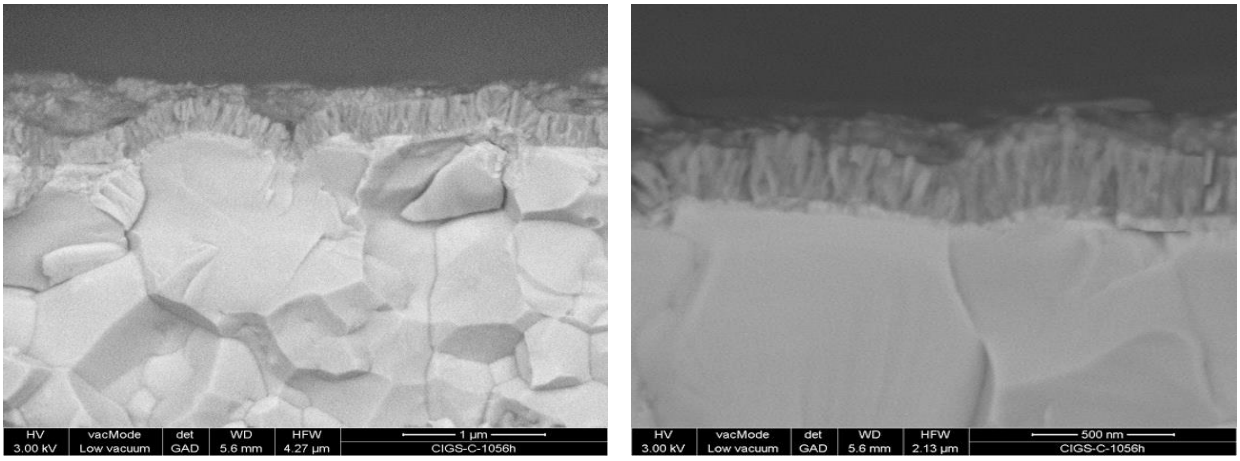

Figure S6.6.6. SEM images of cross-sections of the ZnO:Al films on top of CdS/CIGS after 1056 h of damp-heat degradation at 85°C/85% RH.

References

[1] A. van Veen, H. Schut, J. de Vries, R. A. Hakvoort, and M. R. IJpma, AIP Conference Proceedings **218**, 171 (1990).

[2] F. Lukáč, J. Čížek, I. Procházka, O. Melikhovaa, W. Anwandb, and G. Brauer, Acta Physica Polonica A **125**, 748 (2014).

[3] J. Čížek, F. Lukáč, M. Vlček, M. Vlach, I. Procházka, F. Traeger, D. Rogalla, H. W. Becker, W. Anwand, G. Brauer, S. Wagner, H. Uchida, A. Pundt, and C. B ähtz, Defect and Diffusion Forum **333**, 39 (2013).

[4] A. Uedono, T. Koida, A. Tsukazaki, M. Kawasaki, Z. Q. Chen, S. Chichibu, and H. Koinuma, Journal of Applied Physics **93**, 5 (2003).

[5] Z. Q. Chen, S. J. Wang, M. Maekawa, A. Kawasuso, H. Naramoto, X. L. Yuan, and T. Sekiguchi, Physical Review B **75**, 245206 (2007).

[6] Z. Q. Chen, S. Yamamoto, M. Maekawa, A. Kawasuso, X. L. Yuan, and T. Sekiguchi, Journal of Applied Physics **94**, 4807 (2003).

[7] K. M. Johansen, A. Zubiaga, I. Makkonen, F. Tuomisto, P. T. Neuvonen, K. E. Knutsen, E. V. Monakhov, A. Y. Kuznetsov, and B. G. Svensson, Physical Review B **83** (2011).
[8] K. M. Johansen, F. Tuomisto, I. Makkonen, and L. Vines, Materials Science in Semiconductor Processing **69**, 23 (2017).
[9] R. Krause-Rehberg, and H. Leipner, Positron Annihilation in Semiconductors - Defect Studies, (Springer Verlag, Berlin, 1999).
[10] S. Brunner, W. Puff, A. G. Balogh, and P. Mascher, Materials Science Forum **363-365**, 141 (2001).
[11] B. Oberdorfer and R. Würschum, Phys. Rev. B **79**, 184103 (2009).

Chapter 7

Gradients in vacancy and Ga concentrations in $Cu(In,Ga)Se_2$ Solar Cells studied by Positron Annihilation Spectroscopy and X-ray Diffraction

Abstract

The presence of vacancies and the composition of $Cu(In_{1-x}Ga_x)Se_2$ (CIGS) films grown by a two-stage process were probed by Doppler Broadening Positron Annihilation Spectroscopy (DB-PAS) and X-ray Diffraction (XRD). DB-PAS reveals the presence of a two-layer structure in all films, which is attributed to different concentrations of vacancy defects. The gradient in vacancy concentration is most probably caused by the inhomogeneous composition with depth in the CIGS absorber layer. XRD spectra show that each sample has a non-uniform distribution of Ga and In, and consists of at least three phases with different $In_{1-x}Ga_x$ composition.

7.1. Introduction

$Cu(In_{1-x}Ga_x)Se_2$ (CIGS) polycrystalline films have been intensively studied as absorber layers in solar cells because of their high optical absorption coefficients, high chemical stability, and excellent radiation tolerance. Currently, the efficiency of CIGS-based solar cell can reach 22.6%[1]. Among several methods of preparing CIGS thin films, co-evaporation from elemental sources and selenization of metal precursors are widely used in large-scale fabrication.[2-4] CIGS absorbers produced via these two deposition methods always reveal a Ga gradient.[2] The Ga grading can improve the efficiency of the CIGS solar cells, by engineering the band-gap grading[5,6] (increasing the short circuit current J_{SC}) and reducing recombination at the back contact or the front contact[5,6] (increasing the open circuit voltage V_{OC}). Several characterization techniques such as laterally resolved Photoluminescence (PL), Energy-dispersive X-ray Spectroscopy (EDX), and Secondary Ion Mass Spectrometry (SIMS) are used to characterize such inhomogeneous properties in CIGS thin films.

Positron annihilation is a powerful technique for evaluating the depth-dependent vacancy-type defects in thin film semiconductors. The defects in CIS, CGS, and CIGS thin films formed during the synthesis process (Cu-rich/Cu-poor and various Se fluxes) have been studied by several research groups using positron techniques[7-9]. V_{Cu} monovacancies and V_{Cu}-V_{Se} divacancies were reported to exist in $CuGaSe_2$[7,10] and $CuInSe_2$[10-12] thin film synthesized with various Cu/(In+Ga) ratios. V_{Se}-V_{Cu} complexes were reported to exist in CIGS thin films deposited by a three-stage evaporation process, and these could be affected by the applied Se flux[8] and Se beam equivalent pressure[9]. However, few studies[13,14] report on the influence of Ga grading on the defects within the whole thickness in CIGS absorber layer, which is also important for the solar cell parameters.

In this Chapter, we used depth-dependent positron techniques and X-ray Diffraction (XRD) to study the structure of vacancy defects and the composition in CIGS thin films grown by a two stage process. Samples were grown with different synthesis parameters by varying the selenization temperature and the substrate temperature during the selenization process. In the present study, it was found that the variation of these synthesis parameters only has a relatively small impact on the defect structures and compositions in the CIGS absorber layer. For all samples, the CIGS absorber layer consist of two layers, as obtained from the analysis of the positron depth profiles using the VEPFIT program. The S parameter of the top layer is generally higher than that in the bottom layer of each film, which is attributed to a higher concentration of vacancy defects in the top layer, that in turn may be caused by an inhomogeneous composition with depth of the CIGS absorber layer. XRD spectra show that each CIGS film consists of at least three phases with variation in the $In_{1-x}Ga_x$ composition.

7.2. Experimental

Polycrystalline CIGS films were provided by Dr. Mirjam Theelen, TNO Solliance, Eindhoven. CIGS films with a typical thickness of around 2 μm were grown on Mo-coated soda-lime glass

(SLG) substrates through a two-stage process. This synthesis method consists of two steps, namely (1) the metal deposition of the metals, and (2) selenization (See Figure 7.1(a)). At a specific substrate temperature T(sub.), Cu, In, and Ga are evaporated on the Mo coated SLG substrate as stacked layers, and subsequently the selenization is done under Se vapor at a selenization temperature T(Se), presented in table 7.1. For samples CIGS18500, CIGS24500, and CIGS252000, the precursors were prepared by depositing Se, Cu, Ga, and In layers on Mo-coated SLG substrates, while for samples CIGS5, CIGS10, CIGS12, CIGS24, and CIGS25, Cu, Ga, and In layers are deposited as the precursors. The adjustable parameters were restricted to the selenization step and temperatures as indicated in Figure 7.1(b). The parameters used for each sample are listed in table 7.1.

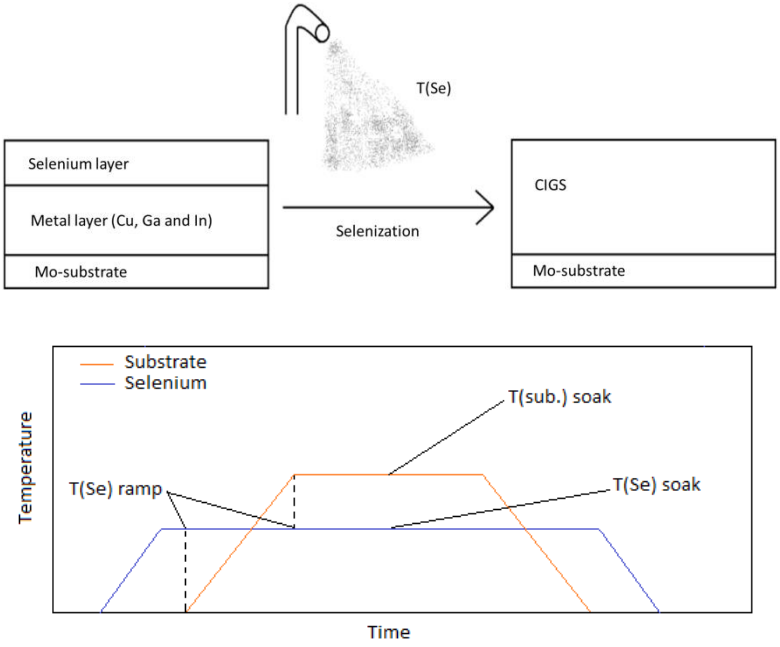

Figure 7.1.(a) Selenization process; (b) Schematic representation of the time evolution of the parameters of the selenization step[15]

Table 7.1. Synthesis conditions of CIGS samples[15]

Sample name	**Se layer thickness (nm)**	**T(Se) Ramp (℃)**	**T(sub.) soak (℃)**	**T(Se) soak (℃)**	**CdS layer (y/n)**
CIGS5	0	390	550	430	n
CIGS10	0	390	590	390	n
CIGS12	0	430	590	390	n
CIGS24	0	390	590	430	y
CIGS25	0	430	550	430	y
CIGS18500	500	200	590	430	y
CIGS24500	500	390	590	430	y
CIGS252000	2000	430	550	430	y

Doppler Broadening Positron Annihilation Spectroscopy (DB-PAS) measurements were performed at room temperature using the mono-energetic positron beam VEP. The implantation energy of positrons was varied from 0.1 keV to 25 keV. The intensity of the low-energy positron beam at the sample position is around 10^4 e^+/s, and the FWHM size of the beam is 7 mm in diameter. A liquid-nitrogen-cooled high-purity Ge (HPGe) detector with an energy resolution of 1.2 keV (~$4.7 \cdot 10^{-3}$ m_0c) was used to determine the energy of the emitted annihilation γ-rays. S and W parameters were extracted from the measured Doppler broadened annihilation γ-ray photo-peak, defined as the fraction of counts in the central region and in the wing regions of the 511 keV annihilation photo-peak, respectively. The momentum windows used to deduce the S parameter and W parameter are $p_L/m_oc < 3.0 \cdot 10^{-3}$ m_oc and $8.2 \cdot 10^{-3}$ $m_oc < p_L/m_oc < 23.4 \cdot 10^{-3}$ m_oc, respectively, with longitudinal momentum $p_L=2\Delta E/c$ and ΔE the Doppler shift in energy of the detected annihilation γ-ray.

The structure of the CIGS films was investigated by X-ray Diffraction (XRD) using a PANalytical X'Pert PRO diffractometer with a Cu Kα beam of 1.5406 Å at 40 mA and 45 kV. An X-ray diffractogram is recorded with step size of 0.008˚and step time of 29.8 s. The data are analysed by using Profile Fitting in the HighScore X'Pert program.

7.3. Results and discussion

7.3.1 Doppler Broadening spectroscopy

In figure 7.2(a) and 7.2(b), the S parameter of bare CIGS/Mo/SLG samples (CIGS5, CIGS10, and CIGS12), and of CIGS/Mo/SLG samples with a CdS layer deposited on top (CIGS24, CIGS24500, CIGS25, CIGS252000, and CIGS18500) are shown as a function of positron implantation energy. The S parameter at E = 0.1 keV is primarily due to positron annihilation at the CIGS surface (0.564) for samples CIGS5, CIGS10, and CIGS12 or at the surface of CdS (0.549) for the other samples. All the S and W depth profiles could be fitted satisfactorily using the VEPFIT program, that is based on the solution of the diffusion equation in each layer of a heterostructure, taking into account the energy-dependent positron implantation profiles.[16] For CIGS24, CIGS24500, CIGS25, CIGS252000 and CIGS18500, the presence of the CdS layer can be distinguished with a fitted thickness of around 20 nm. For all the samples, the depth profiles indicate that the CIGS absorber layer is divided into two layers, most probably due to different chemical compositions or different concentrations of defects formed during the deposition. Figure 7.2(c) shows the layer structure of the samples deduced from the VEPFIT analysis for two representative samples. The mean depth of positrons can be calculated by the formula $< z >= (\frac{\alpha}{\rho})E^n$ ($\rho = 5.7\ \mathrm{g} \cdot cm^{-3}$ is the mass density of CIGS and widely used empirical values are: $\alpha = 4\ \mu g \cdot cm^{-2}$, n=1.6). For the 8 samples, there are only small differences in the S parameter for the CIGS layers under different synthesis conditions.

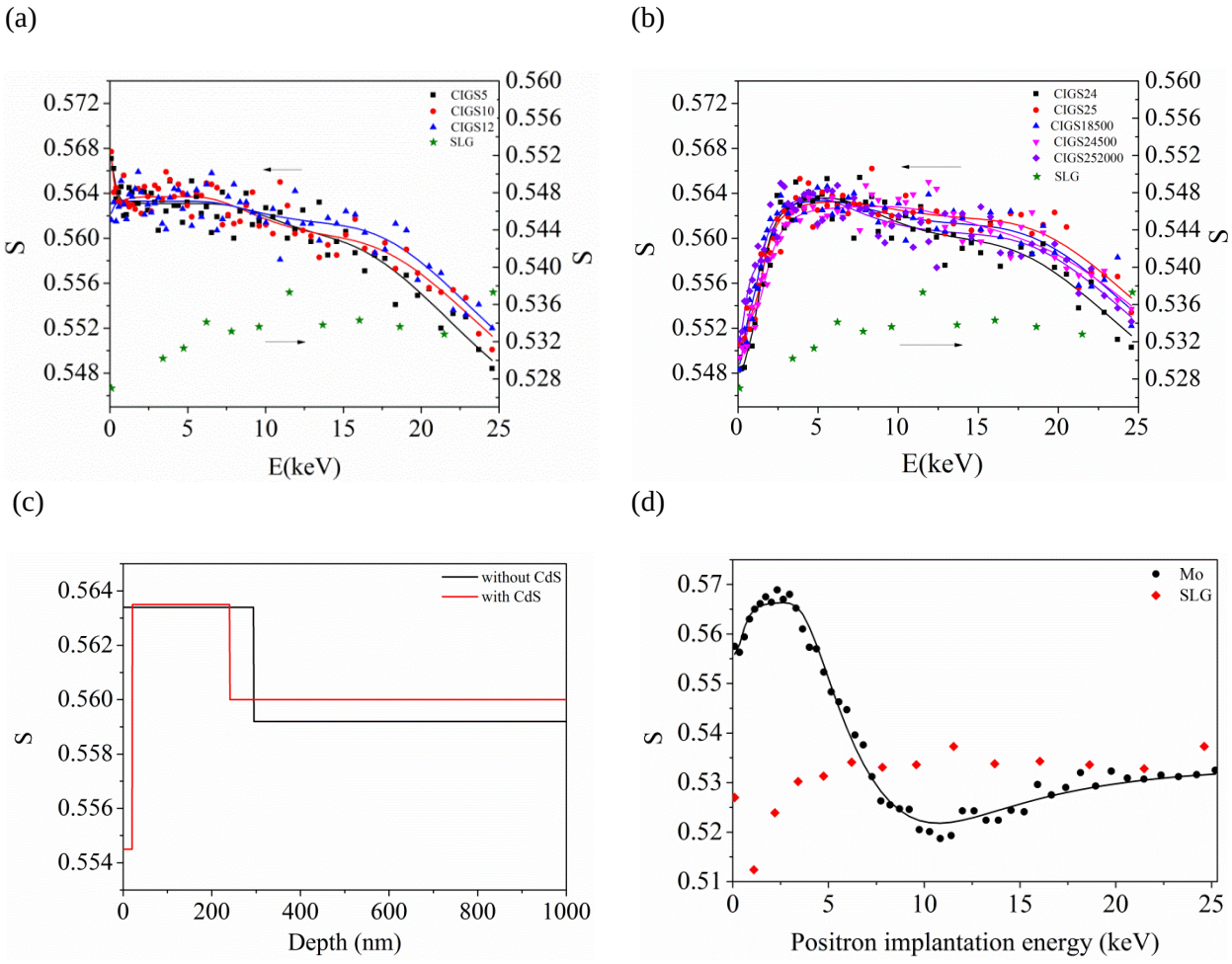

Figure 7.2. S parameters as a function of the positron implantation energy for CIGS films without CdS layer on top (CIGS5, CIGS10, and CIGS12) (a) and with CdS layer on top (CIGS24, CIGS25, CIGS18500, CIGS24500, and CIGS252000) (b) under various synthesis conditions; (c) The layer structure of two representative samples (CIGS10 and CIGS18500) obtained from the VEPFIT analysis; (d) S parameter as a function of the positron implantation energy for Mo layer on top of the SLG substrate and for the bare SLG substrate, respectively. The solid lines are fits to the experimental data obtained by using VEPFIT program.

In order to know the relative contributions of the CIGS layer, Mo layer, and SLG substrate to the S parameter at the high positron implantation energies, the CIGS layer was peeled off from one sample and the Mo layer is revealed on the top. Besides, the bare SLG substrate was probed using the positron beam from the back side of the sample. Figure 7.2(d) shows the corresponding S parameters as a function of the positron implantation energy for the bare Mo layer and the bare SLG substrate. At high positron energies, the majority of positrons reach the SLG substrate in both cases, with an extracted S parameter of 0.534, consistent with the value for the SLG substrate measured from the back side of the sample. The data was fitted by the VEPFIT program, and the presence of two layers for the Mo film with a thickness of 94 nm and 203 nm, respectively, was deduced from the best-fit process. The top layer could correspond to

$MoSe_2$ formed at the interface of the Mo and CIGS films during the deposition of CIGS layer.[17,18] The observed decrease in S at high positron implantation energy region (25 keV) in figure 7.2(a) and 7.2(b) is due to an increasingly large fraction of positron annihilation in the Mo layer and the SLG substrate.

7.3.2. S-W mapping

An important property of S and W is their linearity. We can examine the presence of positron trap states in a material by replotting the S and W of a specific Doppler depth profile in a so-called S-W graph. If vacancies (or different phases) exist in a material, the parameter W will depend linearly on the S parameter, going from the defect-free material to the case with increasingly large vacancy concentrations (or going from annihilation in one pure phase to the other phase for the case of two phases). Therefore, the S-W plot of each sample is presented in figure 7.3, drawn separately for clarity. The S-W plot graphs (a)-(c) reveal a similar trend for samples CIGS5, CIGS10, CIGS12. The arrow along the S-W trajectory shows the direction of increased positron implantation energy. The S-W plots show that there are most likely two types of vacancies or two different composition layers for the CIGS film in these three samples, consistent with the fitting results from VEPFIT program in figure 7.2(a). Besides, the low energy part of the curve shows a different trend because of positron annihilation at the surface. At high energies, the S-W points move in a direction towards the S-W point of the Mo/SLG substrate. For the samples CIGS 24, CIGS24500, CIGS25, CIGS252000 and CIGS18500, the S-W plots show a different trend at low energies because of the presence of the CdS top layer. It is obvious that there are three layers in these samples, one CdS layer and two CIGS layers. The initial part of the plot again reflects positron annihilation at the surface.

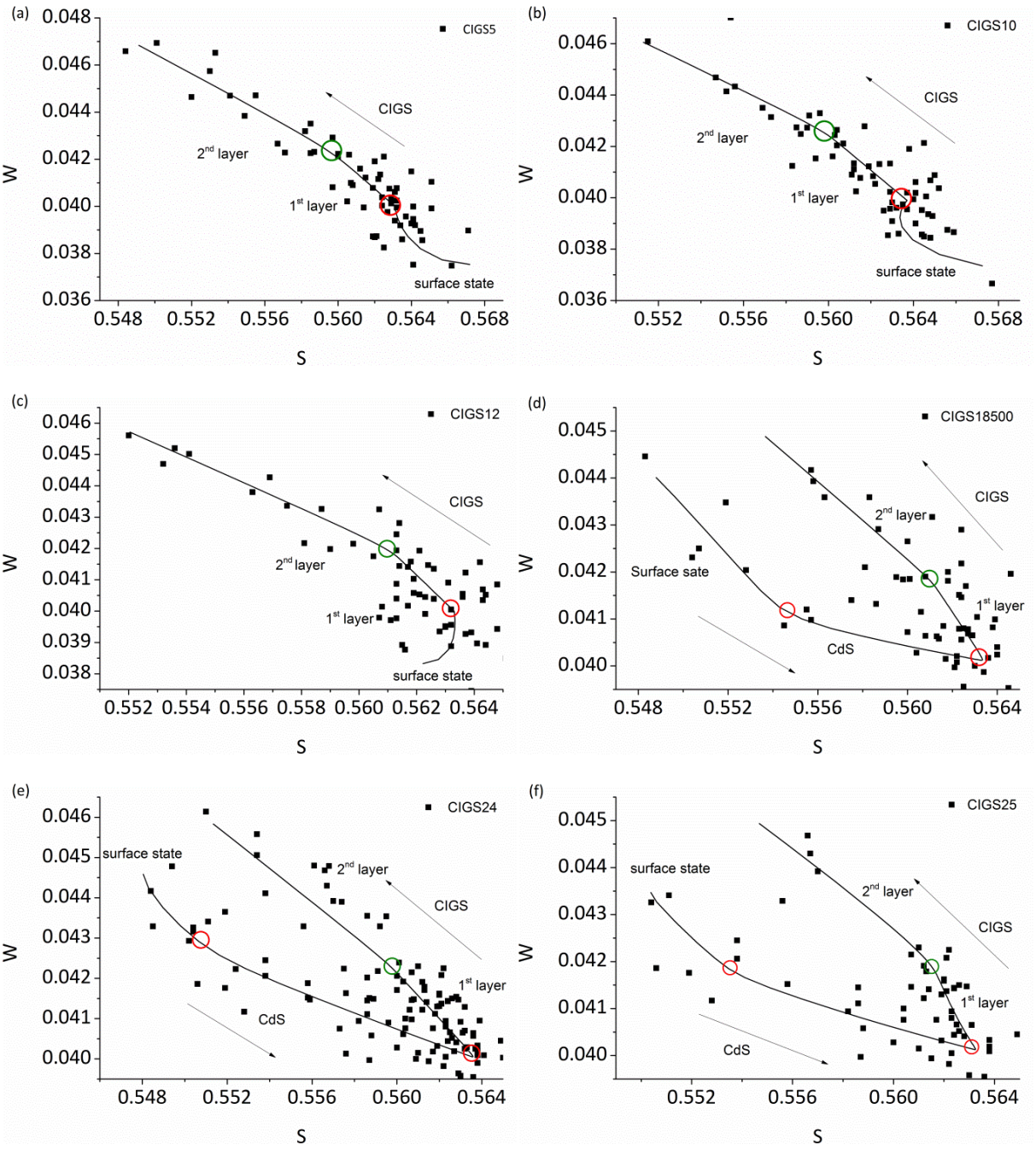

Figure 7.3. S-W graph for the CIGS samples. The arrow along the S-W trajectory shows the direction of increased positron implantation energy (increased average depth). The circles indicate the identified annihilation sites in the samples.

7.3.3. X-ray Diffraction pattern

Figure 7.4 shows X-ray Diffraction patterns of these 8 CIGS samples, consisting mainly of diffraction peaks of $Cu(In_{1-x}Ga_x)Se_2$ and Mo with their Miller indices indicated in the figure. Diffraction peaks of the thin layer CdS were not observed in the spectra. The diffraction data are modeled by a profile fitting procedure in X'pert Highscore plus, using pseudo-Voigt functions

which are a linear combination of Gaussian and Lorentzian components to fit each diffraction peak independently. This method can be used to determine accurately peak positions and peak intensities in a complex diffraction pattern composed of several diffraction peaks. In the analysis, we did not take into consideration the effects of sample displacement and transparency of X-rays on the peak position and peak intensity, respectively. Figure 7.5(a) shows one representative XRD pattern together with the fitted data, and the difference between measured and fitted data for sample CIGS25. The main (112) and (220)/(204) peaks that are characteristic for $Cu(In_{1-x}Ga_x)Se_2$, show that the CIGS films consist in fact of (at least) three phases, extracted from the profile fitting procedure (figure 7.5(b) and (c)). The fit was performed assuming three phases, but leads to fairly broad maxima indicating a spread in lattice constants. The lattice parameters a and c for the tetragonal CIGS phase are calculated by the (112) and (220)/(204) peak position and listed in table 7.2(a). These parameters calculated from (112) and (220) peak position differ slightly from the calculation from (112) and (204) peak position shown in table 7.2(b) with CIGS5 as an example, probably due to the effects of inaccuracy in the zero angle position, sample displacement, and/or lattice strain. Thus, we used their average value for a and c parameters with uncertainties as shown in table 7.2(b). The uncertainties also lead to uncertainty in the $In_{1-x}Ga_x$ composition calculated by using Vegard's law below. One also should notice that it is not trivial to assign (220) peak and (204) peak for each phase, since the (220) peak and (204) peak will overlap when c/a=2 or even reverse their order when c/a >2, which corresponds to a low content of Ga ($x<0.2$).[19] The position of the (112) peak ② for the intermediate phase is prone to error, since it is very broad and partially overlaps with the (112) peak ① and (112) peak ③, as shown in figure 7.5(b). The lattice parameters calculated are listed in table 7.2. According to Vegard's law[19],

$$a = 5.774 - 0.169x \tag{7.1}$$

$$c = 11.603 - 0.636x \tag{7.2}$$

the $In_{1-x}Ga_x$ composition can be estimated, also listed in table 7.2(a).

As shown in table 7.2(a), each sample consists of (at least) three phases with variation in Ga content. The compositions in each phase are similar among the eight samples, indicating that the synthesis condition in our case does not significantly affect the compositions in CIGS. For each CIGS film, the intensity of In-rich phase is the highest, probably indicating that this In-rich phase is dominant or it is positioned at the surface since the penetration depths of the X-rays also has a significant effect on the peak intensity.

7.3.4 Interpretation of the positron Doppler parameters

An increase of Ga composition in $Cu(In_{1-x}Ga_x)Se_2$ leads to smaller unit cell parameters. These could have different effects on the positron data. First, the volume contraction could be expected to contribute to a decrease of the S parameter, since the valence electron states will be more confined, leading to an increase in their (average) momentum, and corresponding broadening of

the electron momentum distribution N(p). Second, Ga 3d electrons are more tightly bound than In 4d electrons and the outer d electrons have smaller spatial extent, which leads to lower annihilation probability of the outer d electrons with positrons. While these Ga 3d electrons will contribute to a broader and more slowly descending contribution in momentum space than In 4d electrons[20], the relatively increased annihilation probability with s-p valence electrons is expected to result in a higher S and perhaps also in a lower W parameter. Thus, here it is hard to determine the contribution of Ga and In in the positron data of CIGS without further experiments or theoretical calculations as a reference. Third, volume contraction will lead to a decrease of the interstitial open volume for positrons[21] in $Cu(In_{1-x}Ga_x)Se_2$. The calculated positron annihilation lifetime in the delocalized state in defect-free (bulk) CGS (220 ps) is slightly smaller than in CIS (232 ps).[9]

However, the combined variation of unit cell parameters and $In_{1-x}Ga_x$ composition probably has a relatively small effect on the positron data, since the difference between the two lifetimes is small when varying Ga_x from 0 to 1. More importantly, Figure 7.6 shows the reference (S, W) data points for bulk CIS and CGS extracted from Ref. [10] marked with dark open circles. In this paper[10], the authors indicated that their CIS bulk crystal is nearly defect-free from a positron annihilation point of view, exhibiting perfect crystal structure while they indicate that about 50% of the positrons trapped at the divacancies V_{Cu}-V_{Se} in the CGS bulk crystal.[10] However, the authors also extracted the (S, W) data point for a CGS sample grown under Cu excess, leading to very small concentrations of vacancies. This (S, W) point can be used as a reference for defect-free CGS, and is marked with a red open circle in Figure 7.6. The closeness of the values of the (S, W) data points extracted in this way for CIS and CGS further indicates that the $In_{1-x}Ga_x$ composition has only little effect on the positron Doppler data as well. In CIGS samples, the strong variation of the S and W parameter with the depth in the CIGS film could thus most probably be attributed to the vacancy defects that can be created due to the lattice distortion caused by the variation of the $In_{1-x}Ga_x$ composition[13,19,22]. The (S, W) data points extracted from the 1st layer and 2nd layer of CIGS of the 8 samples are shown in figure 7.6. The shift in S-W from the top to the bottom layer is remarkably similar for all 8 samples. Comparison with the data of Ref. [10] indicates that the vacancy defects in the top layer of the current CIGS samples (1st layer and 2nd layer) could also be V_{Cu}-V_{Se} complexes[10], since the parameter $R = \triangle S/\triangle W = 1.5 \pm 0.3$ that presents the shift direction in the S-W plot upon an increase in positron trapping in the vacancy defects is quite comparable with the corresponding parameter R=2 for CGS and R=1.8 for CIS, respectively, characteristic for positron trapping in the V_{Cu}-V_{Se} divacancy in CGS and CIS[10]. Please note that the data points are far away from the reference data of Ref. [10], which could be due to the differences in the energy resolution[23-25] and energy window[25] chosen to determine the S and W parameters.

(a)

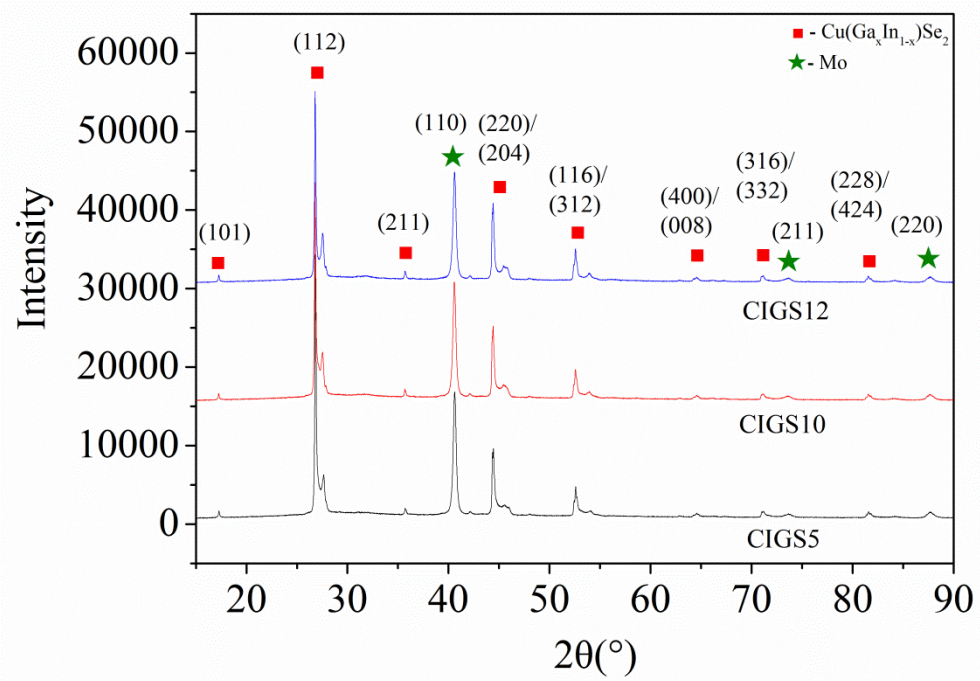

(b)

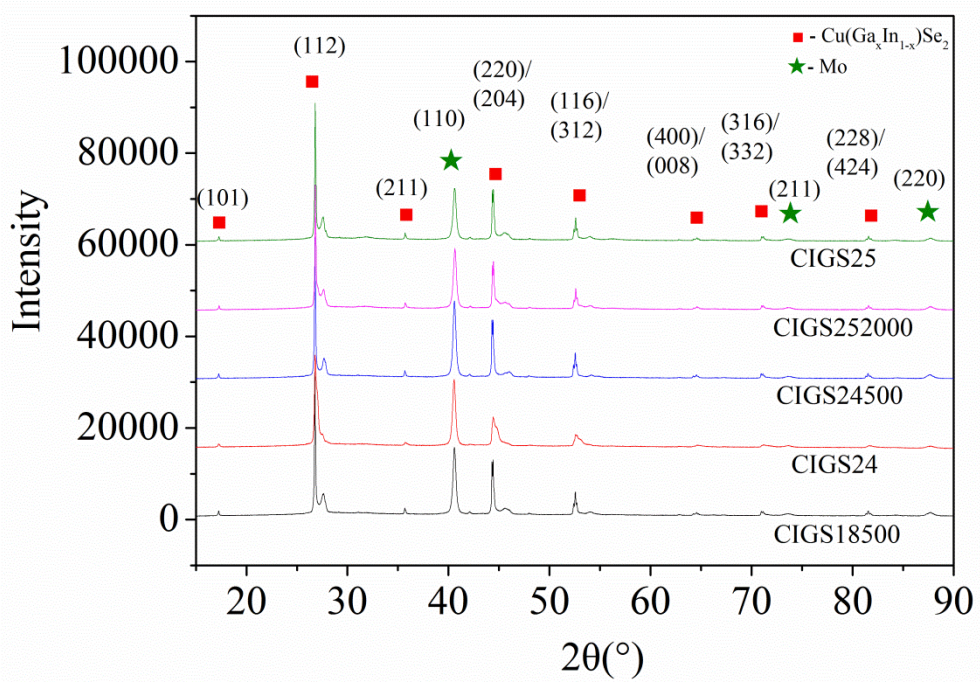

Figure 7.4. X-ray Diffraction patterns of the 8 CIGS samples; (a) without CdS top layer, and (b) with CdS top layer.

(a)

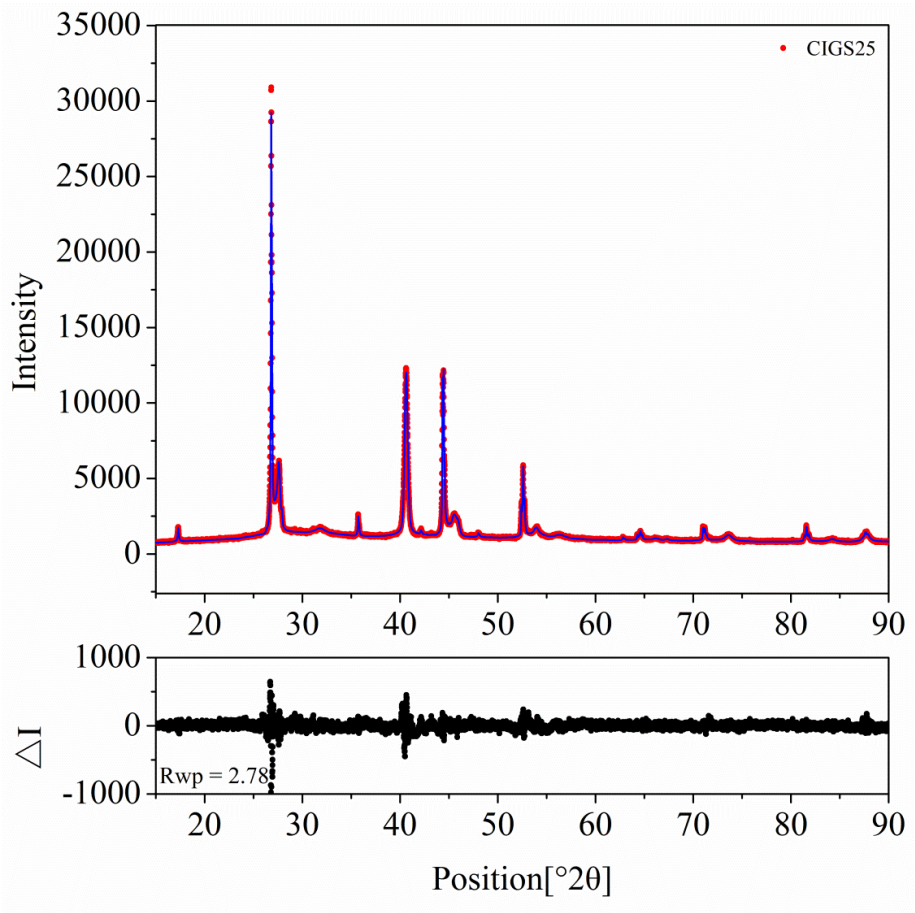

(b)

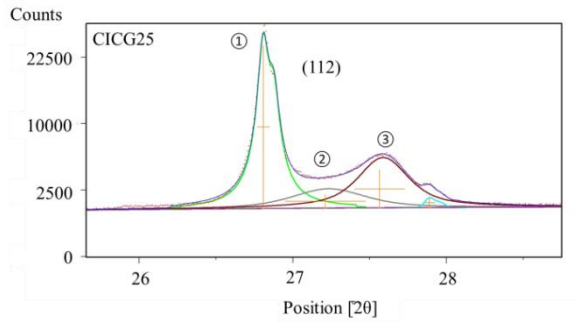

(c)

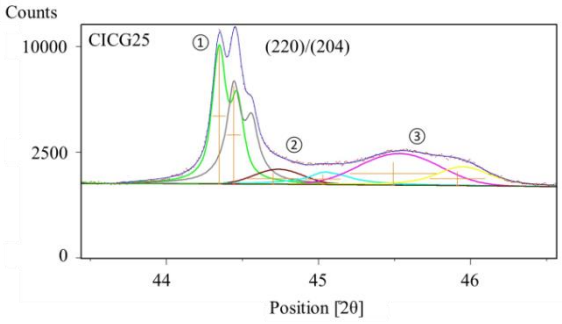

Figure 7.5. (a) XRD data for sample CIGS25 and fitted data by the profile fitting procedure described in the text; (b) and (c) Profile fitting of respectively the (112) and (220)/(204) peaks of sample CIGS25. (dot line: experimental diffraction data; blue line: fitted data by profile fitting; orange solid line: the peak positions; green, grey, and brown line: diffraction peaks plotted for each phase separately, as calculated by the profile fitting procedure)

Table 7.2.(a) Lattice parameters for each phase in the 8 investigated CIGS samples

Sample	Phase	Lattice parameter		Intensity(counts)
		a(Å)	c(Å)	
CIGS5	$Cu(In_{0.86}Ga_{0.14})Se_2$	5.75(0.02)	11.50(0.08)	26089
	$Cu(In_{0.70}Ga_{0.30})Se_2$	5.716(0.003)	11.37(0.01)	1878
	$Cu(In_{0.13}Ga_{0.87})Se_2$	5.673(0.009)	11.07(0.03)	3181
CIGS10	$Cu(In_{0.89}Ga_{0.11})Se_2$	5.76(0.01)	11.51(0.05)	22595
	$Cu(In_{0.65}Ga_{0.35})Se_2$	5.711(0.007)	11.32(0.03)	1596
	$Cu(In_{0.22}Ga_{0.78})Se_2$	5.63(0.02)	11.17(0.08)	3813
CIGS12	$Cu(In_{0.88}Ga_{0.12})Se_2$	5.76(0.02)	11.50(0.06)	18582
	$Cu(In_{0.70}Ga_{0.30})Se_2$	5.730(0.007)	11.32(0.03)	1065
	$Cu(In_{0.20}Ga_{0.80})Se_2$	5.636(0.001)	11.104(0.003)	13146
CIGS24	$Cu(In_{0.89}Ga_{0.11})Se_2$	5.76(0.02)	11.52(0.06)	13146
	$Cu(In_{0.81}Ga_{0.19})Se_2$	5.727	11.414	6893
	$Cu(In_{0.27}Ga_{0.73})Se_2$	5.68(0.02)	11.04(0.08)	1466
CIGS24500	$Cu(In_{0.90}Ga_{0.10})Se_2$	5.77(0.01)	11.51(0.05)	25522
	$Cu(In_{0.69}Ga_{0.31})Se_2$	5.735(0.009)	11.29(0.04)	434
	$Cu(In_{0.11}Ga_{0.89})Se_2$	5.620(0.004)	11.05(0.02)	2554
CIGS25	$Cu(In_{0.87}Ga_{0.13})Se_2$	5.76(0.01)	11.50(0.06)	24383
	$Cu(In_{0.54}Ga_{0.46})Se_2$	5.68(0.05)	11.3(0.2)	878
	$Cu(In_{0.27}Ga_{0.83})Se_2$	5.632(0.003)	11.08(0.01)	2972
CIGS252000	$Cu(In_{0.86}Ga_{0.14})Se_2$	5.73(0.04)	11.50(0.07)	22564
	$Cu(In_{0.78}Ga_{0.22})Se_2$	5.76(0.03)	11.3(0.1)	3204
	$Cu(In_{0.13}Ga_{0.87})Se_2$	5.625(0.003)	11.06(0.01)	2513
CIGS18500	$Cu(In_{0.90}Ga_{0.10})Se_2$	5.769(0.008)	11.50(0.03)	25249
	$Cu(In_{0.79}Ga_{0.21})Se_2$	5.723	11.383	647
	$Cu(In_{0.17}Ga_{0.83})Se_2$	5.637(0.003)	11.07(0.01)	2627

Table 7.2.(b) Lattice parameters for each phase in CIGS samples

CIGS5		Lattice parameter		Vegard's law	
				a=5.774-0.169x	c=11.603-0.636x
		a (Å)	c (Å)	Ga_x	Ga_x
(112)/(220)	Phase ①	5.773	11.427	0.004	0.276
	Phase ②	5.713	11.378	0.123	0.353
	Phase ③	5.630	11.042	0.855	0.882
(112)/(204)	Phase ①	5.735	11.577	0.226	0.041
	Phase ②	5.719	11.354	0.323	0.392
	Phase ③	5.613	11.104	0.951	0.784
Average value	Phase ①	5.75(0.02)	11.50(0.08)	0.12(0.11)	0.16(0.12)
	Phase ②	5.716(0.003)	11.37(0.01)	0.22(0.10)	0.37(0.02)
	Phase ③	5.673(0.009)	11.07(0.03)	0.90 (0.05)	0.83(0.05)

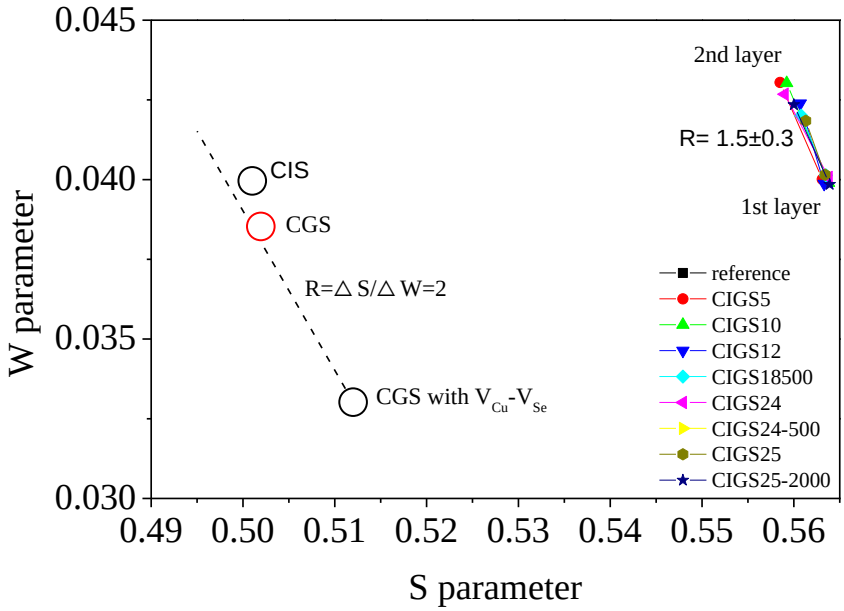

Figure 7.6. (S, W) data points extracted from Doppler Broadening spectra of CIGS. The data points for CIS, CGS and CGS with 50% positron trapping in V_{Cu}-V_{Se} vacancy complex (open circles) extracted from the Ref. [10].

7.4. Conclusion

We used Doppler Broadening Positron Annihilation Spectroscopy (DB-PAS) to study the defect structure and the layer structure of 8 CIGS samples grown by a two-stage process. Upon varying the synthesis conditions, including selenization temperature and substrate temperature during the selenization process, it was observed that the S (W) parameters show relatively little differences among these samples. Further, the CdS buffer layer could be distinguished for sample CIGS24, CIGS25, CIGS18500, CIGS24500, and CIGS252000 in the Doppler depth profiles. For all CIGS absorber layers, it was seen in the Doppler depth profiles that the CIGS film actually consists of two layers. The S parameter in the top region is generally higher than that in the bottom region of each film, which is probably due to the higher concentration of vacancy defects, that we attribute to the presence of V_{Cu}-V_{Se} di-vacancies, based on previous positron studies. The defects might in turn be associated with the inhomogeneous composition (variation in Ga contents) along with the depth in the CIGS absorber layer. XRD spectra show that each sample consists of (at least) three phases with variation of the $In_{1-x}Ga_x$ composition. In order to further identify the types of vacancy defects in CIGS films, good reference samples, like defect-free $CuInSe_2$ or $CuGaSe_2$ bulk crystals, are required and further positron experiments, such as coincidence Doppler Broadening of Positron Annihilation Spectroscopy (CDB) and Positron annihilation lifetime spectroscopy (PALS) are necessary in order to extract the local chemical environment of the defects and their size, respectively. In order to examine the possible correlation between the vacancy defects and the presence of a Ga gradient in CIGS films, the depth-dependent Ga contents could be quantified by Energy-dispersive X-ray Spectroscopy (EDX) or Secondary Ion Mass Spectrometry (SIMS).

References

[1] P. Jackson, R. Wuerz, D. Hariskos, E. Lotter, W. Witte, and M. Powalla, Physica Status Solidi (RRL) **10**, 583 (2016).

[2] W. Witte, D. Abou-Ras, K. Albe, G. H. Bauer, F. Bertram, C. Boit, R. Brüggemann, J. Christen, J. Dietrich, A. Eicke, D. Hariskos, M. Maiberg, R. Mainz, M. Meessen, M. Müller, O. Neumann, T. Orgis, S. Paetel, J. Pohl, H. Rodriguez-Alvarez, R. Scheer, H.-W. Schock, T. Unold, A. Weber, and M. Powalla, Progress in Photovoltaics: Research and Applications **23**, 717 (2015).

[3] A. Slobodskyy, T. Slobodskyy, T. Ulyanenkova, S. Doyle, M. Powalla, T. Baumbach, and U. Lemmer, Applied Physics Letters **97**, 251911 (2010).

[4] M. Marudachalam, R. W. Birkmire, H. Hichri, J. M. Schultz, A. Swartzlander, and M. M. Al-Jassim, Journal of Applied Physics **82**, 2896 (1997).

[5] S. Schleussner, U. Zimmermann, T. Wätjen, K. Leifer, and M. Edoff, Solar Energy Materials and Solar Cells **95**, 721 (2011).

[6] T. Dullweber, G. Hanna, W. Shams-Kolahi, A. Schwartzlander, M. A. Contreras, R. Noufi, and H. W. Schock, Thin Solid Films **361-362**, 478 (2000).

[7] M. M. Islam, A. Uedono, S. Ishibashi, K. Tenjinbayashi, T. Sakurai, A. Yamada, S. Ishizuka, K. Matsubara, S. Niki, and K. Akimoto, Applied Physics Letters **98**, 112105 (2011).

[8] M. M. Islam, A. Uedono, T. Sakurai, A. Yamada, S. Ishizuka, K. Matsubara, S. Niki, and K. Akimoto, Journal of Applied Physics **113**, 064907 (2013).

[9] A. Uedono, M. M. Islam, T. Sakurai, C. Hugenschmidt, W. Egger, R. Scheer, R. Krause-Rehberg, and K. Akimoto, Thin Solid Films **603**, 418 (2016).

[10] E. Korhonen, K. Kuitunen, F. Tuomisto, A. Urbaniak, M. Igalson, J. Larsen, L. Gütay, S. Siebentritt, and Y. Tomm, Physical Review B **86**, 064102 (2012).

[11] A. Polity, R. Krause-Rehberg, T. E. M. Staab, M. J. Puska, J. Klais, H. J. Möller, and B. K. Meyer, Journal of Applied Physics **83**, 71 (1998).

[12] L. Zhang, T. Wang, J. Li, Y. Hao, J. Liu, P. Zhang, B. Cheng, Z. Zhang, B. Wang, and B. Ye, Thin Solid Films **525**, 68 (2012).

[13] G. Hanna, A. Jasenek, U. Rau, and H. W. Schock, Thin Solid Films **387**, 71 (2001).

[14] S.-H. Wei, S. B. Zhang, and A. Zunger, Applied Physics Letters **72**, 3199 (1998).

[15] J. Noteboom, XRD and PL of CIGSe, TNO report, 2013.

[16] A. van Veen, H. Schut, J. de Vries, R. A. Hakvoort, and M. R. Ijpma, AIP Conference Proceedings 218, 171 (1990).

[17] T. Klinkert, B. Theys, G. Patriarche, M. Jubault, F. Donsanti, J. F. Guillemoles, and D. Lincot, The Journal of chemical physics **145**, 154702 (2016).

[18] T. Wada, N. Kohara, S. Nishiwaki, and T. Negami, Thin Solid Films **387**, 118 (2001).

[19] M. R. Balboul, H. W. Schock, S. A. Fayak, A. A. El-Aal, J. H. Werner, and A. A. Ramadan, Applied Physics A **92**, 557 (2008).

[20] K. Saarinen, P. Hautojärvi, and C. Corbel, in Identification of Defects in Semiconductors, edited by M. Stavola (Academic, San Diego, 1998), pp. 239.

[21] F. Plazaola, A. P. Seitsonen, and M. J. Puska, Journal of Physics: Condensed Matter **6**, 8809 (1994).

[22] G. Hanna, A. Jasenek, U. Rau, and H. W. Schock, Phys. Stat. Sol. (a) **179**, R7 (2000).

[23] V. J. Ghosh, B. Nielsen, A. C. Kruseman, P. E. Mijnarends, A. van Veen, and K. G. Lynn, Applied Surface Science **149**, 234 (1999).

[24] J. Heikinheimo, J. Ala-Heikkilä, and F. Tuomisto, Nuclear Instruments and Methods in Physics Research Section A: Accelerators, Spectrometers, Detectors and Associated Equipment **867**, 215 (2017).
[25] F. Linez, I. Makkonen, and F. Tuomisto, Physical Review B **94**, 014103 (2016).

Summary

High efficiency, low cost, and long stability are three key factors for the wide application of photovoltaics (PV) which are currently intensively studied in order to meet the increasing global renewable energy demand. Currently, the PV market is mainly based on silicon. However, solar cells based on silicon may not be capable to meet the long-term global energy demand due to their relatively high costs and high energy required for the synthesis of silicon wafers, opening the door to conventional thin films (such as $Cu(In_{1-x}Ga_x)Se_2$ (CIGS)) and innovative thin films (e.g. semiconductor quantum dots (QDs), based on PbS, PbSe, CdSe QDs). The advantages of QDs as solar cell materials are the low-temperature synthesis process, the tunable band gap via control of the composition and size, and the promise of physical mechanisms that may increase efficiency above the Shockley-Queisser limit, such as multiple exciton generation (MEG), in which more than one exciton is created from a single photon. However, the low efficiency, with a current laboratory record just above 10%, and the durability are still limitations on their widespread application in the PV market. It is very important to understand the surface structure and surface-ligand interactions in order to improve the efficiency and stability of QD solar cells. For CIGS solar cells, research-cell efficiencies have reached 22.6%, which is just below the efficiencies of Si-based solar cells. Besides, various deposition approaches have been developed that can supply high-efficiency, low-cost and large-area solar cell devices. However, it is still a challenge to guarantee long-term stability of CIGS modules. CIGS solar cells can be well protected by sealing into glass plates, but this in turn increases the manufacturing cost. Therefore, understanding of the degradation mechanism is necessary.

Positron techniques are powerful tools to study the surface composition of QDs and to determine the types of open space deficiencies in thin film materials. For QDs, previous studies provided indications that positrons can trap and annihilate at the surfaces of semiconductor QDs and can effectively probe the surface composition and electronic structure of colloidal semiconductor QDs. For CIGS, previous depth-sensitive positron experiments indicated the sensitivity of positrons to probe the types of vacancy-related defects in CIGS.

This thesis presents positron studies on two types of solar cell materials, namely semiconductor quantum dots (CdSe QDs and PbSe QDs) and $ZnO:Al/CdS/Cu(In_{1-x}Ga_x)Se_2$ (CIGS) layered systems, which are important for the further development of QD and CIGS thin film solar cells. The first objective of this thesis is to establish firm evidence that positrons are trapped at the surfaces of quantum dots, and provide a sound understanding of the nature of positron surface states (**Chapter 3**). Further, this property of the positron is used to study the surface composition and electronic structure of ligand-capped PbSe and CdSe semiconductor QDs embedded in thin films (**Chapter 4** and **5**). The second objective is to examine the stability and

degradation mechanism of ZnO:Al window layers for CIGS solar cells under damp heat conditions of 85% relative humidity (RH) and 85^{o}C in close comparison with the observed degradation of the solar cell parameters (**Chapter 6**), and to investigate in a depth-resolved manner the presence of vacancies and variations in Ga concentration in CIGS using positron techniques and X-ray diffraction, respectively (**Chapter 7**). Below we elaborate on the hightlights of these two main themes.

Positron studies of surface compositions and surface-ligand interactions in CdSe and PbSe QDs thin films

Previous positron two-dimensional Angular Correlation of Annihilation Radiation (2D-ACAR) studies on CdSe and PbSe QDs and Positron Annihilation Lifetime Spectroscopy (PALS) studies on PbSe QDs indicated that positrons can be trapped and annihilate at the surface of QDs and thus may effectively probe the surface compositions of QDs. In Chapter 3, we provide firm evidence of the existence of a positron surface state in quantum dots through a combined approach using PALS experiments at MLZ Garching and ab-initio calculations by Vincent Callewaert employing the recent formulation of the Weighted Density Approximation (WDA) developed at the University of Antwerpen. The PALS studies reveal a dominant fraction (77% - 84%) of positrons annihilate with a lifetime in the narrow range of 358-371 ps, indicating that the majority of positrons are trapped and annihilate at the surfaces of the CdSe QDs. The ab-initio calculations of the positron wave function and lifetime based on WDA provide strong theoretical support for the existence of a positron surface state, leading to theoretical lifetimes that are close to the experimental values, and provide detailed insights into the wave function of the positron at the surfaces of CdSe QDs. Our study thus resolves the longstanding debate regarding the nature of the positron state in semiconductor QDs. This opens a new pathway to extract quantitative information on surface composition and ligand-surface interactions of colloidal QDs via positron techniques based on Coincidence Doppler Broadening (CDB) and 2D-ACAR.

With this solid foundation based on experimental and theoretical evidence of positron surface state in CdSe quantum dots, positron annihilation is further used in this thesis to probe the electronic structure and surface compositional structure of PbSe QDs and CdSe QDs embedded in thin films.

In Chapter 4, the variation in electronic structure and composition at the surfaces of PbSe quantum dots (QDs) capped with various ligands are investigated by using the positron 2D-ACAR method. The positron can probe effectively the variation of the surface composition caused by various ligands. Also, for PbSe QDs, it is observed that the electron-positron momentum distributions are strongly affected by electronic coupling of valence electrons of neighbouring QDs when small ethyldiamine (EDA) molecules are applied as the ligands. Besides, the local oxidation process at the surfaces of colloidal nanocrystals, resulting from long term exposure to air, is monitored by the highly surface sensitive positron method.

In Chapter 5, the 2D-ACAR method is used to investigate the sensitivity of positron annihilation in probing the modification of the surface composition of CdSe QDs induced by the variation in ligand capping, including trioctylphosphine oxide (TOPO), oleic acid (OA), oleylamine (OLA), and stearic acid (SA) ligands, obtained through ligand exchange. The majority of the positrons are trapped at the surfaces of CdSe QDs, annihilating with Cd atoms and Se atoms at the surface and the atoms (oxygen (O) or nitrogen (N)) of ligands binding with the CdSe QDs. CdSe QDs with OA and SA ligands have similar intensity in the high momentum region, since they possess the same anchor group, –(C=O)O–, and a large $C_{17}H_{33}$ or $C_{17}H_{35}$ tail. CdSe QDs with TOPO, OA, and SA ligands show a higher intensity in the high momentum region than OLA ligands, because the O(1s) core electrons contribute strongly to the high momentum intensity. However, when comparing with PbSe QDs, the positron is less sensitive in probing the surface composition of CdSe QDs, as the observed variation in the intensity of the momentum distribution of CdSe QDs at the high momenta is much smaller than for the case of PbSe QDs. This is attributed to the more covalent nature of the bonds between O (or N) atoms and Cd atoms, leading to a similar probability of annihilation with electrons of O (or N) atoms and Se atoms, unlike the case of PbSe QDs, where the positron predominantly annihilates with electrons of O (or N) atoms that are attached via a more ionic bond to the excess Pb atoms forming a shell on PbSe QDs.

Positron studies of defect structures in ZnO:Al/CdS/Cu($In_{1-x}Ga_x$)Se_2 (CIGS) solar cells

Chapter 6 explores the mechanism of the degradation of the ZnO:Al transparaent conducting window layer for Cu(In,Ga)Se_2 (CIGS) solar cells by using Doppler Broadening Positron Annihilation Spectroscopy (DB-PAS) and Positron Annihilation Lifetime Spectroscopy (PALS). PALS and DB-PAS reveal the growth of vacancy clusters at the grain boundaries and mono-vacancies inside the grains induced by damp-heat exposure. The formation of open space at the grain boundaries may form an additional barrier against charge carrier transport through the transparent conductive oxide layer, contributing to the increase in series resistance. The direct comparison with the degradation of solar parameters such as efficiency and series resistance indicates that this can be one of the major reasons for the degradation of the cell efficiency. The depth-sensitive DB-PAS technique provided indications that open volume formation in the ZnO:Al layer in CIGS solar systems contributes to the deterioration of the cell efficiency under the accelerated damp heat condition. The increase in S- and decrease in W- parameters with accelerated degradation time suggests that the degradation of the ZnO:Al layer involves the formation of open volume, such as mono-vacancies or small vacancy clusters. Besides, the S parameter shows a great increase starting from the surface of the ZnO:Al layer and, over time, also in the deeper parts of the ZnO:Al layer, with a time dependence that matches with an in-diffusion process in which H_2O and CO_2 diffuse at the grain boundaries, react with ZnO:Al. The positron studies show that this process also leads to the creation of open-volume defects. Using an in-diffusion model, it was found that the time- and depth-dependence of the Doppler depth-profiles can be accurately described, with an extracted diffusion coefficient of 35 nm^2/hour that is similar to typical values extracted from SIMS profiles of in-diffused deuterium in previous

studies. The PALS results reveal that most positrons (64%-74%) trap and annihilate in Zn mono-vacancies V_{Zn} inside the grains, while 25%-34% of positrons trap and annihilate in vacancy clusters $(V_{Zn})_m(V_O)_n$ at the grain boundaries, with a higher fraction of positrons annihilating in larger vacancy clusters in the top layer compared to the bottom layer. With degradation time, the size of the vacancy clusters at the grain boundaries increases, and a higher trapping fraction of positrons at the grain boundaries is observed.

In Chapter 7, the presence of vacancies and the composition of $Cu(In_{1-x}Ga_x)Se_2$ (CIGS) films grown by a two-stage process were probed by Doppler Broadening Positron Annihilation Spectroscopy (DB-PAS) and X-ray Diffraction (XRD), respectively. DB-PAS reveals the presence of a two-layer structure in all CIGS films, which is attributed to different concentrations of vacancy defects, with a higher concentration in the top layer of the films. The gradient in vacancy concentration is most probably caused by an inhomogeneous composition that varies with depth in the CIGS absorber layer. The XRD diffractograms show that the CIGS film of each sample has a non-uniform distribution of Ga and In, and consists of at least three phases with different $In_{1-x}Ga_x$ composition.

Samenvatting

Hoge efficiëntie, lage kosten en langdurige stabiliteit zijn drie sleutelfactoren voor de brede toepassing van foto-voltaïsche cellen (PV), die momenteel intensief bestudeerd worden om tegemoet te komen aan de toenemende wereldwijde vraag naar duurzame energie. De huidige PV markt is hoofdzakelijk gebaseerd op silicium. Echter, zonnecellen gebaseerd op silicium zijn mogelijk niet in staat tegemoet te komen aan de wereldwijde energievraag op de lange termijn door hun relatief hoge kosten en de hoge energie, die nodig is voor de vervaardiging van silicium plakken, wat de weg vrij laat voor conventionele dunne lagen (zoals $Cu(In_{1-x}Ga_x)Se_2$ (CIGS)) en innovatieve dunne lagen (bijv. halfgeleider quantum dots (QDs), gebaseerd op PbS, PbSe of CdSe QDs). De voordelen van QDs als zonnecelmateriaal zijn de lage temperatuur van het vervaardigingsproces, de afstembare bandkloof door middel van samenstelling en grootte en het vooruitzicht van fysische mechanismen, die de efficiëntie kunnen verhogen tot boven de Shockley-Queisser limiet, zoals multiexciton generatie (MEG), waarbij meer dan één exciton wordt gemaakt met een enkel foton. Maar de efficiëntie, met een huidig record in het laboratorium van net boven de 10%, en de stabiliteit beperken nog hun brede toepassing in de PV markt. Het is zeer belangrijk om de oppervlaktestructuur en de wisselwerking tussen oppervlak en ligand te begrijpen om de efficiëntie en stabiliteit van QD zonnecellen te verbeteren. Voor CIGS zonnecellen heeft de efficiëntie van onderzoekscellen de 22.6% bereikt, wat net beneden de efficiënties ligt van op Si gebaseerde zonnecellen. Bovendien zijn verschillende depositietechnieken ontwikkeld, die zonnecellen met hoge efficiëntie, lage kosten en een groot oppervlak kunnen opleveren. Het is echter nog steeds een uitdaging om langdurige stabiliteit van CIGS modules te garanderen. CIGS zonnecellen kunnen goed beschermd worden door opsluiting in glasplaten, maar dit verhoogt op zijn beurt de fabricagekosten. Daarom is het noodzakelijk het degradatiemechanisme te begrijpen.

Positronentechnieken zijn krachtige hulpmiddelen om de oppervlaktesamenstelling van QDs te bestuderen en de aard van lege-ruimte defecten in dunne-laag materialen te bepalen. Voor QDs, gaven eerdere studies aanwijzingen, dat positronen ingevangen kunnen worden en annihileren aan de oppervlakken van halfgeleider QDs en een effectieve sonde kunnen zijn voor de oppervlaktesamenstelling en de elektronenstructuur van colloïdale halfgeleider QDs. Voor CIGS wezen eerdere dieptegevoelige positronenexperimenten op de gevoeligheid van positronen voor de aard van aan vacatures gerelateerde defecten in CIGS.

Dit proefschrift presenteert positronenstudies aan twee typen materialen voor zonnecellen, te weten halfgeleider quantum dots (CdSe QDs en PbSe QDs) en $ZnO:Al/CdS/Cu(In_{1-x}Ga_x)Se_2$ (CIGS) gelaagde systemen, die van belang zijn voor de verdere ontwikkeling van QD en CIGS dunne-laag zonnecellen. Het eerste streefdoel van dit proefschrift is met solide evidentie vast te

stellen, dat positronen ingevangen worden aan de oppervlakken van quantum dots, en een grondig begrip te verwerven van de aard van de oppervlaktetoestand van het positron (Hoofdstuk 3). Verder wordt deze eigenschap van het positron gebruikt om de oppervlaktesamenstelling en elektronenstructuur te bestuderen van door ligand bedekte PbSe and CdSe halfgeleider QDs ingebed in dunne lagen (Hoofdstuk 4 en 5). Het tweede streefdoel is om de stabiliteit en het degradatiemechanisme van ZnO:Al vensterlagen voor CIGS zonnecellen onder omstandigheden van vochtige warmte van 85% relatieve vochtigheid (RH) en 85^{o}C te bestuderen in nauwe samenhang met de waargenomen degradatie van de zonnecelparameters (Hoofdstuk 6) en met een methode met diepteresolutie de aanwezigheid van vacatures te onderzoeken en Ga concentraties in CIGS met respectievelijk positronentechnieken en Röntgendiffractie te bestuderen (Hoofdstuk 7).

Positronenstudies van oppervlaktesamenstelling en oppervlakte-ligand wisselwerking in CdSe en PbSe QDs dunne lagen

Eerdere twee-dimensionale Angular Correlation of Annihilation Radiation (2D-ACAR) positronenstudies aan CdSe en PbSe QDs en Positron Annihilatie Levensduur Spectroscopie (PALS) studies aan PbSe QDs gaven aanwijzingen, dat positronen ingevangen kunnen worden en annihileren aan het oppervlak van QDs en zo effectief de oppervlaktesamenstelling van QDs kunnen detecteren. In Hoofdstuk 3 geven wij solide evidentie voor het bestaan van een positronenoppervlaktetoestand in quantum dots door een gecombineerde benadering met PALS experimenten bij MLZ Garching en ab-initio berekeningen door Vincent Callewaert met gebruik van de recente formulering van de Weighted Density Approximation (WDA) ontwikkeld bij de Universiteit van Antwerpen. De PALS studies onthullen, dat een dominante fractie (77% - 84%) van de positronen annihileert met een levensduur in het nauwe bereik van 358-371 ps, wat aangeeft dat de meerderheid van de positronen wordt ingevangen en annihileert bij de oppervlakken van de CdSe QDs. De ab-initio berekeningen van de positronengolffunctie en levensduur gebaseerd op de WDA geven sterke theoretische ondersteuning aan het bestaan van een oppervlaktetoestand van het positron, wat leidt tot theoretische levensduren, die dicht bij de experimentele waarden liggen, en geven gedetailleerd inzicht in de golffunctie van het positron bij de oppervlakken van CdSe QDs. Onze studie biedt zo de oplossing voor het langdurige meningsverschil aangaande de aard van de positrontoestand in halfgeleider QDs. Dit creëert een nieuwe route om kwantitatieve informatie over oppervlaktesamenstelling en ligand-oppervlak wisselwerking van colloïdale QDs af te leiden via positrontechnieken gebaseerd op Coincidence Doppler Broadening (CDB) en 2D-ACAR.

Met deze solide fundering gebaseerd op experimentele en theoretische evidentie voor een oppervlaktetoestand voor positronen in CdSe quantum dots wordt positronannihilatie verder in dit proefschrift gebruikt als sonde voor de elektronenstructuur en oppervlaktesamenstellingsstructuur van PbSe QDs en CdSe QDs ingebed in dunne lagen.

In Hoofdstuk 4 worden de variatie in elektronenstructuur en samenstelling bij de oppervlakken van PbSe quantum dots (QDs), als zij bedekt zijn met verschillende liganden, onderzocht met

gebruik van de positronen 2D-ACAR methode. Het positron kan effectief de variatie van de oppervlaktesamenstelling veroorzaakt door verschillende liganden detecteren. Ook wordt voor PbSe QDs waargenomen, dat de elektron-positron impulsverdelingen sterk beïnvloed worden door elektronenkoppeling van valentie-elektronen van naburige QDs, wanneer kleine ethyldiamine (EDA) moleculen als ligand worden toegepast. Daarnaast wordt het lokale oxidatieproces aan de oppervlakken van colloïdale nanokristallen, dat voortkomt uit langdurige blootstelling aan lucht, gevolgd met de sterk oppervlaktegevoelige positronenmethode.

In Hoofdstuk 5 wordt de 2D-ACAR methode gebruikt om de gevoeligheid te onderzoeken van positronannihilatie voor het detecteren van de verandering van de oppervlaktesamenstelling van CdSe QDs geïnduceerd door de ligandbedekking te variëren, waarbij trioctylfosfine oxide (TOPO), oliezuur (OA), oleylamine (OLA) en stearinezuur (SA) als liganden gebruikt worden, verkregen door liganduitwisseling. De meerderheid van de positronen wordt ingevangen aan de oppervlakken van CdSe QDs, waar zij annihileren met Cd atomen en Se atomen aan het oppervlak en de atomen (zuurstof (O) of stikstof (N)) van liganden, die binden aan de CdSe QDs. CdSe QDs met OA en SA liganden hebben vergelijkbare intensiteit in het hoge-impuls regime, daar zij dezelfde ankergroep hebben, –(C=O)O–, en een lange $C_{17}H_{33}$ of $C_{17}H_{35}$ staart. CdSe QDs met TOPO, OA en SA liganden vertonen een hogere intensiteit in het hoge-impuls regime dan OLA liganden, omdat de O(1s) binnenschilelektronen sterk bijdragen aan hoge-impuls intensiteit. Echter, in vergelijking met PbSe QDs is het positron minder gevoelig voor het detecteren van de oppervlaktesamenstelling van CdSe QDs, omdat de waargenomen variatie in de intensiteit van de impulsverdeling van CdSe QDs bij hoge impuls veel kleiner is dan in het geval van PbSe QDs. Dit wordt toegeschreven aan de meer covalente aard van de bindingen tussen O (of N) atomen en Cd atomen, wat leidt tot een eendere waarschijnlijkheid voor annihilatie met elektronen van O (of N) atomen en Se atomen, anders dan in het geval van PbSe QDs, waar het positron overwegend annihileert met elektronen van O (of N) atomen, die via een meer ionische binding gebonden zijn aan de extra Pb atomen, die een schil vormen om PbSe QDs.

Positronenstudies aan defectstructuren in ZnO:Al/CdS/Cu($In_{1-x}Ga_x$)Se_2 (CIGS) zonnecellen

Hoofdstuk 6 verkent het mechanisme van de degradatie van de ZnO:Al vensterlaag voor Cu(In,Ga)Se_2 (CIGS) zonnecellen door gebruik te maken van Doppler Broadening Positron Annihilatie Spectroscopie (DB-PAS) en Positron Annihilatie Levensduur Spectroscopie (PALS). PALS en DB-PAS onthullen de groei van vacatureclusters aan de korrelgrenzen en mono-vacatures binnenin de korrels geïnduceerd door blootstelling aan vocht en hitte. De vorming van lege ruimte aan korrelgrenzen zou een additionele barrière kunnen vormen voor transport van ladingsdragers door de transparante geleidende oxidelaag, waardoor het bijdraagt aan toename in serieweerstand. Directe vergelijking met de degradatie van zonnecelparameters zoals efficiëntie en serieweerstand geeft aan, dat dit één van de belangrijkste redenen kan zijn voor de degradatie van de efficiëntie van de cel. De diepte-gevoelige DB-PAS techniek gaf

aanwijzingen, dat vorming van lege ruimte in de ZnO:Al laag in CIGS zonnecelsystemen bijdraagt aan de verslechtering van de efficiëntie van de cel onder de versnelde vochtige-warmte conditie. De toename in S en afname in W met versnelde degradatietijd suggereert, dat de degradatie van de ZnO:Al laag de vorming van lege ruimte, zoals mono-vacatures of kleine vacatureclusters, met zich mee brengt. Daarnaast vertoont de S-parameter een grote toename uitgaand van het oppervlak van de ZnO:Al laag en mettertijd ook in de diepere delen van de ZnO:Al laag met een tijdafhankelijkheid, die overeenkomt met een in-diffusie proces, waarin H_2O en CO_2 diffunderen langs de korrelgrenzen en reageren met ZnO:Al. De positronenstudies tonen, dat dit proces ook leidt tot de creatie van lege-ruimte defecten. Gebruik makend van een in-diffusie model werd gevonden, dat de tijd- en diepte-afhankelijkheid van de Doppler diepteprofielen accuraat beschreven kunnen worden, met een daaruit afgeleide diffusiecoëfficiënt van 35 nm^2/uur, die lijkt op typische waarden afgeleid uit SIMS profielen van in-gediffundeerd deuterium in eerdere studies. De PALS resultaten onthullen, dat de meeste positronen (64%-74%) worden ingevangen en annihileren in Zn mono-vacatures V_{Zn} binnen in de korrels, terwijl 25%-34% van de positronen ingevangen wordt en annihileert in vacatureclusters $(V_{Zn})_m(V_O)_n$ bij de korrelgrenzen, waarbij een grotere fractie van de positronen annihileert in grotere vacatureclusters in de bovenste laag vergeleken met de onderste laag. Met de degradatietijd neemt de grootte van de vacatureclusters bij de korrelgrenzen toe en wordt een grotere vangstfractie voor positronen aan de korrelgrenzen waargenomen.

In Hoofdstuk 7 werden de aanwezigheid van vacatures en de samenstelling van $Cu(In_{1-x}Ga_x)Se_2$ (CIGS) lagen, gegroeid met een twee-staps proces, gedetecteerd met Doppler Broadening Positron Annihilatie Spectroscopie (DB-PAS) en X-ray Diffractie (XRD), respectievelijk. DB-PAS laat de aanwezigheid van een twee-lagen structuur zien in alle CIGS films, wat toegeschreven wordt aan verschillende concentraties aan vacaturedefecten, met een hogere concentratie in de bovenste laag van de films. De gradiënt in vacatureconcentratie wordt hoogstwaarschijnlijk veroorzaakt door een inhomogene samenstelling, die met de diepte varieert in de CIGS absorber-laag. De XRD diffractogrammen tonen, dat de CIGS film van elk proefstuk een non-uniforme verdeling van Ga en In heeft en bestaat uit tenminste drie fasen met verschillende $In_{1-x}Ga_x$ samenstelling.

Acknowledgements

Preparing this thesis is not easy, and I couldn't have done it without many people involved. I'm glad I can take this opportunity to thank all of them.

I would like first to acknowledge my daily supervisor, Dr. S.W.H. Eijt, for giving me the opportunity to work as a PhD student in Fundamental Aspects of Materials and Energy (FAME) group. As a supervisor, Stephan is very responsible. He could always give me some right direction when I felt lost in the research and give me great support when I had some difficulties in experiments and data analysis during my PhD study. I learnt a lot through each work discussion on experiments, data analysis, presentation, and journal paper writing. His abundant knowledge in positron physics and cheerful attitude always aspire me. I also want to thank my promotor, prof. dr. E.H. Brück, for the work discussion in the progress meeting. He can always give me some valuable advices in experiments and data analysis.

The work in this thesis couldn't be done without the support and cooperation from people in other area of expertise. I'm greatly grateful to Dr. Theelen, who works in TNO/Solliance, for her support in the supply of CIGS samples, sample degradation treatment, and I-V measurement. Thank Dr. A. J. Houtepen and Dr. C.S. S. Sandeep for their supply of PbSe QDs samples and the support on the Optical Absorption Spectroscopy measurement in Chemical Engineering, in Delft University of Technology. I'm grateful to Dr. R. W. Meulenberg from University of Maine (USA) for supplying us two batches of CdSe QDs samples of high quality. Thank Dr. W. Egger and Marcel Dickmann for their support on Positron Annihilation Lifetime measurement in MLZ, Germany. Deep gratitude to Prof. B. Barbiellini for the guidance in conceiving the paper on Nature of the Positron State in CdSe Quantum Dots, which is finally published in Physical Review Letters. His positive attitude to the research results and extensive expertise in the positron always impress me. Thanks to Vincent Callewaert, a PhD student in University of Antwerp (Belgium), for his great contribution of the first-principles calculation to the paper on nature of the Positron State in CdSe Quantum Dots and valuable discussion. Special gratitude is given to Prof. Yuanzhi Li, my master supervisor, and Dr. Guang Ye. With their support, I can pursuit my PhD in the Netherlands.

I'm glad to be one member of FAME group. I greatly appreciate the technical support from the staff of FAME and NPM2. I would like to express my gratitude to Dr. H. Schut in NPM2 group, who gives me many supports in the Doppler Broadening of Positron Annihilation measurement. He can always kindly and cheerfully explain me how the VEPFIT setup works and how to use VEPFITI program. Deep gratitude to Ing. M.R. de Boer in NPM2 group for his great support for the measurement of 2-dimensional Angular Correlation of Annihilation Radiation (2D-ACAR)

during my first three years of PhD. He is always easygoing and kind to provide help. Many thanks go to Dr. M. Butterling, who is an expert in positron lifetime, for his guidance for the analysis of positron annihilation lifetime. Thanks to Ing. A.J.E. Lefering and Ing. M.P. Steenvoorden for helping me solve problems on glovebox. Thank Dr. J.R. Heringa for his support on computer and translation of my thesis summary. Thanks to Drs. K. Goubitz for the support for XRD measurement and his effort, sometimes with Dr. S. Ganapathy, to organize Christmas lunch every year. I'm greatly thankful to our secretaries, Nicole Banga and Ilse van der Kraaij-Quick, for their administrative support and their efforts to organize wonderful activities.

The great "thank you" also goes to other colleagues in FAME group. Thanks to my officemates Zhou Zhou, Haixing Fang, Maurits Boeije, and lately joined Yifan Fu for the warm and friendly working environment. I am happy that we share the office together. Thanks to Zhou Zhou and Haixing Fang for solving some programming problems and many other problems for me. I also want to thank other colleagues, Bowei Huang, Zhaolong Li, Bei Tian, Xinmin You, Jiawei Lai, Prasad and alumni of FAME, NPM2, and SEE groups such as Xiaoyu Zhang, Kun Shen, Shasha Zhang, Yaolin Xu, Xuefei Miao, Fengjiao Qian, Chuang Yu, Yibole for their accompany and interesting lunch talks.

I would like to thank Dr. Zhiwei Qian, who organized several road trips to see beautiful lavender in South France, to go to the lively Christmas Market in Germany, and to stroll along the crystal-blue coastline in Malta, which make my PhD life more delightful. I'm grateful to Xuliang Hou, Ying Yang, Tianshi Lu, Bei Wu, Peng Gao, Hua Dong, Xu Ma, Maria Varini, Kai Li, and Shulan Shu for their accompany on my trips.

I want to thank my family, especially my parents, who always love and support me. Deep gratitude to my parents-in-law who are enthusiastic and full of energy. They organise everything well for us when we are back to China. I am always inspired by their positive attitude to the family, to friends, and to their career. With the encouragement from our parents, my husband and I can always pursuit what we want to do.

Finally, I am grateful to my husband, Jiayi Chen, who is a generous and considerate person, for supporting and accompanying me to do anything I want to do.

List of Publications

1. **W. Shi**, M. Theelen, A. Illiberi, N. Barreau, S. J. van der Sar, M. Butterling, H. Schut, W. Egger, M. Dickmann, C. Hugenschmidt, M. Zeman, E. Brück, and S. W. H. Eijt, Evolution and Role of Vacancy Clusters at Grain Boundaries of ZnO:Al during accelerated Degradation of Cu(In,Ga)Se_2 Solar Cells revealed by Positron Annihilation, Physical Review Materials **2**, 105403 (2018)

2. **W. Shi**, V. Callewaert, B. Barbiellini, R. Saniz, M. Butterling, W. Egger, M. Dickmann, C. Hugenschmidt, B. Shakeri, R. W. Meulenberg, E. Brück, B. Partoens, A. Bansil, and S. Eijt, Nature of the positron state in CdSe quantum dots, Physical Review Letters **121**, 057401 (2018)

3. **W. Shi**, M. Theelen, V. Gevaerts , A. Illiberi, N. Barreau, M. Butterling, H. Schut, W. Egger, M. Dickmann, C. Hugenschmidt, M. Zeman, E. Brück, and S. W. H. Eijt, Positron annihilation studies on as-deposited and damp heat degraded CIGS solar cells with a ZnO:Al Transparent Conductive Oxide layer. IEEE Journal of Photovoltaics, vol. 8, no. 6, pp. 1847-1851, Oct. 2018

4. **W. Shi**, S. W. H. Eijt, C. S. S. Sandeep, L. D. A. Siebbeles, A. J. Houtepen, S. Kinge, E. Brück, B. Barbiellini, and A. Bansil, Ligand-surface interactions and surface oxidation of colloidal PbSe quantum dots revealed by thin-film positron annihilation methods, Applied Physics Letters **108**, 081602 (2016)

5. S. W. H. Eijt, **W. Shi**, A. Mannheim, M. Butterling, H. Schut, W. Egger, M. Dickmann, C. Hugenschmidt, B. Shakeri, R. Meulenberg, V. Callewaert, R Saniz, B. Partoens, B. Barbiellini, A. Bansil, J. Melskens, M. Zeman, A. H. M. Smets, M. Kulbak, G. Hodes, D. Cahen, E. H. Brück, New insights into the nanostructure of innovative thin film solar cells gained by positron annihilation spectroscopy. Journal of Physics Conference Series, 2017, 791(012021):1-6

Other publications

6. **W. Shi**, Y. Li, J. Hou, H. Lv, X. Zhao, P. Fang, F. Zheng, X. Wang, Densely populated mesopores in microcuboid CeO2 crystal leading to a significant enhancement of catalytic activity. J. Mater. Chem. A **1**(3): p. 728-734 (2013).

7. W. Xie, Y. Li, **W. Shi**, L. Zhao, X. Zhao, P. Fang, F. Zheng, S. Wang, Novel effect of significant enhancement of gas-phase photocatalytic efficiency for nano ZnO. Chemical Engineering Journal **213**: p. 218-224 (2012).

8. Y. Li, Q. Sun, M. Kong, **W. Shi**, J. Huang, J. Tang, X. Zhao, Coupling Oxygen Ion Conduction to Photocatalysis in Mesoporous Nanorod-like Ceria Significantly Improves Photocatalytic Efficiency. The Journal of Physical Chemistry C **115**(29): p. 14050-14057(2011).

9. W. Sun, Y. Li, **W. Shi**, X. Zhao, P. Fang, Formation of AgI/TiO_2 nanocomposite leads to excellent thermochromic reversibility and photostability. Journal of Materials Chemistry **21**(25): p. 9263 (2011).

10. D. Xia, J. Xu, **W. Shi**, P. Lei and X. Zhao, Synthesis and properties of SnS thin films by chemical bath deposition. In Key Engineering Materials (Vol. 509, pp. 333-338). Trans Tech Publications (2012).

Conference presentations

1. **W. Shi** et al, Surface composition and electronic structure of PbSe quantum dots for solar cells, The International Workshop on Positron Studies of Defects, Sep, 2014, Kyoto, Japan. (Poster)

2. **W. Shi** et al, Ligand-surface interactions and surface oxidation of colloidal PbSe quantum dots revealed by thin-film positron annihilation methods, 17th International Conference on Positron Annihilation (ICPA-17), Sep, 2015, Wuhan, China. (Oral presentation)

3. **W. Shi** et al, The degradation behaviour of ZnO:Al during accelerated degradation of Cu(In,Ga)Se2 solar cells revealed by positron annihilation, Chemistry as innovating science (Chains), Dec, 2017, the Netherlands. (Oral presentation)

Curriculum Vitae

Wenqin Shi

born on 21st February 1987

Wuhan, Hubei, China

Sep. 2005 – Jun. 2009

Bachelor's degree in Material Physics, Hubei University, Wuhan, China

Sept. 2009 – Jun. 2012

Master's degree in Optoelectronic and Information Function Materials, State Key Laboratory of Silicate Materials for Architectures, Wuhan University of Technology, Wuhan, China

Oct. 2012 – Jan. 2019

PhD candidate in the group Fundamental Aspects of Materials and Energy (FAME), Faculty of Applied Science, Delft University of Technology, Delft, the Netherlands